East Asian Journal on Applied Mathematics
doi: 10.4208/eajam.040411.030611a

Vol. **1**, No. 4, pp. 297-371
November 2011

REVIEW ARTICLE

Interface Dynamics and Far-From-Equilibrium Phase Transitions in Multilayer Epitaxial Growth and Erosion on Crystal Surfaces: Continuum Theory Insights

Leonardo Golubović[*,1], Artem Levandovsky[2] and Dorel Moldovan[3]

[1] *Physics Department, West Virginia University, Morgantown WV 26506-6315, USA.*
[2] *Department of Physics and Astronomy, University of California, Riverside, CA 92521, USA.*
[3] *Mechanical Engineering Department, Louisiana State University, Baton Rouge, LA 70803-6413, USA.*

Received 4 April 2011; Accepted (in revised version) 3 June 2011

Available online 23 September 2011

Abstract. We review recent theoretical progress in the physical understanding of far-from-equilibrium phenomena seen experimentally in epitaxial growth and erosion on crystal surfaces. The formation and dynamics of various interface structures (pyramids, ripples, etc.), and also kinetic phase transitions observed between these structures, can all be understood within a simple continuum model based on the mass conservation law and respecting the symmetries of the growing crystal surface. In particular, theoretical predictions and experimental results are compared for (001), (110) and (111) crystal surfaces.

PACS (2006): 81.15.Aa, 89.75.Kd, 05.90.+m

Key words: Interface dynamics, epitaxial growth, non-equilibrium phase transitions.

Contents

[*]Corresponding author. *Email address:* lgolubovic@yahoo.com (L. Golubović)

1. Introduction

There is extensive research interest in the dynamics of the surfaces of thin films undergoing molecular beam epitaxy (MBE) growth. The MBE technique is considered the best method for the growth of thin solid films, of great importance in applied and experimental studies [1]. It is a unique way to grow high quality crystalline materials; and in particular, to form structures with very high precision in the vertical direction perpendicular to the substrate, such as monolayer-thin interfaces or atomically flat surfaces. However, multilayer epitaxial growth may exhibit complex surface features that cannot easily be controlled experimentally. In epitaxial multilayer growth regimes, surface morphology dynamics involves a subtle interplay between the depositing molecular flux and the relaxation of the surface profile through the surface diffusion of adatoms. Of paramount significance are adatom interactions with steps that form on the multilayered surface, particularly the energy barriers occurring near the step edges that inhibit adatom transitions between layers of the growing interface. These so-called step edge barriers were found by Ehrlich and Hudda [2], and further elucidated by Schwoebel [3] and Villain [4]. Ehrlich-Schwoebel-Villain (ESV) energy barriers produce up-hill adatom surface currents, from the terrace of the lower layer towards the terrace of the upper layer. The ESV effect produces instabilities in the evolution of the surface morphology, which ultimately lead to the formation of fascinating structures such as mounds and pyramids across the growing interface [5, 6]. The ESV instability is a non-equilibrium effect, which is present only if the adatom density on a terrace is higher than in equilibrium. The deposition process by molecular beams raises the adatom density well above its equilibrium value, and surface currents are generated that depend on the local slope of the growing film. From a study of the diffusive dynamics of adatoms on vicinal surfaces with step edge barriers, Villain [4] found that the surface non-equilibrium current $\mathbf{J}^{\mathrm{NE}}$ has the same direction as the slope, and consequently tends to increase the local slope of the interface. However, once the interface attains sufficiently large slopes, other processes that counterbalance the destabilizing ESV effect also become significant, so the net current in *non-equilibrium* states vanishes for certain slopes (slope selection). Indeed, funneling and knockout processes [7, 8] can lead to zeros of $\mathbf{J}^{\mathrm{NE}}(M)$, even for small values of the interface slope M [9, 10]. Due to slope selection, the interface restructures into facets with pyramid-like objects. The slopes of these facets correspond to stable zeros of the non-equilibrium surface current.

Many experiments have shown that the surface evolution of films grown by MBE frequently involves the formation of pyramids or pyramid-like structures, even for homoepitaxial growth. Pyramid-like structures have often been observed — e.g. on the homoepitaxy of GaAs [6, 11], Cu [5, 44], Ge [12] and Fe [13, 14], all grown on singular (001) substrates, and on the Rh(111) surface [15]. The lateral size λ and height w of these pyramids grow in time as power laws with the *same* exponent. Thus the ratio w/λ corresponding to the pyramid slope eventually approaches a constant value, so there is

https://doi.org/10.4208/eajam.040411.030611a Published online by Cambridge University Press

a slope selection in typical epitaxial growth. Importantly, the corresponding coarsening exponent of the power law for the growth of λ and w was found experimentally to depend on the symmetry of the surface. For example, the experimental value of the coarsening exponent for growth on (001) surfaces is close to $1/4$ in agreement with simulations [16, 17], whereas the exponent reported for the growth on (111) surfaces is close to $1/3$ [15]. However, although there has been extensive experimental work, until recently there has not been sufficient understanding of how the large scale surface morphology coarsens in MBE and why the exponents have these values.

Seminal studies by two of us [18], and independently by Siegert [19], gave an initial qualitative understanding of the nature of the coarsening processes seen in multilayer epitaxial growth. In particular, a combination of numerical simulations and analysis provided the first *analytic* explanation of the coarsening law exponents seen in MBE growth [18]. The approach was inspired in part by theories of phase ordering processes such as the growth of domains in magnetic systems [20], assuming an underlying effective free energy that governs the film surface dynamics as in earlier work on epitaxial growth [21, 22]. Indeed, the dynamics of surface-like elastic manifolds such as membranes are governed by an elastic free energy, exemplified in studies of the buckling dynamics of semi-flexible polymers and membranes [23, 24]. However, since epitaxial growth has a number of specific features, no standard phase ordering theory seemed applicable, so our subsequent studies of epitaxial growth [25–29] reviewed in this article deliberately avoided the effective free energy assumption. A particularly significant effect, not tractable using an effective free energy approach, is the ubiquitous *vertical growth asymmetry* present in any realistic interface dynamics. The vertical asymmetry reflects the fact that the medium and conditions above the interface (in the vacuum hosting the molecular beam) are not the same as the medium and conditions below the interface (in the solid bulk). This yields experimentally well known differences between the shapes of pyramid tops and valleys (pyramidal pits). However, the actual role of the vertical asymmetry on the interface morphologies remained elusive until our more recent studies on (110) surfaces [27] and (001) surfaces [29] reviewed here (cf. § 4.2 and § 5).

Our approach involves numerical simulations and the analysis of continuum interface dynamics models constructed for various types of crystal surface symmetry. Our simple continuum models are based on mass conservation of the deposited thin film, and respect the strong restrictions imposed by symmetries of the growing crystal surface (cf. § 2). From these fundamentals alone, coarsening exponents are analytically obtained, and qualitative differences between the coarsening behaviors experimentally observed on hexagonal symmetry (111) and on square symmetry (001) surfaces are explained (cf. § 3). As initially found [18], there are striking qualitative differences in the surface morphologies (spatial organization of pyramids) on different symmetry surfaces, with pyramids arranged as nearly regular arrays (2D-crystal-like arrangements) on (001) surfaces but randomly (2D-glass-like arrangements) on (111) surfaces — cf.

https://doi.org/10.4208/eajam.040411.030611a Published online by Cambridge University Press

§ 3. One of the major findings of Ref. [18] was that the *edges* between pyramids facets, which form a network across the growing interface, are essential for a conceptual and qualitative understanding of the coarsening dynamics of molecular beam epitaxy (cf. § 2, § 3 and § 4.3).

In this review, we also discuss the rich interfacial phenomena observed in multilayer homoepitaxial growth and erosion on (110) crystal surfaces [30–35]. Experimentally, these rectangular symmetry surfaces exhibit a multitude of interesting non-equilibrium interfacial structures, such as rippled one-dimensionally periodic states not present in the homoepitaxial growth and erosion on high symmetry (001) and (111) crystal surfaces. The continuum theory approach, developed in Refs. [25–28] and reviewed here, provides a unified phenomenological model that predicts and elucidates a multitude of novel interfacial states on (110) surfaces and the far-from-equilibrium transitions between them (cf. § 4), including the observed transitions between two major types of rippled states on (110) surfaces in the so-called 90° ripple rotation transition [30, 31, 33–35]. The model has revealed several novel intermediate interface states, intervening via consecutive transitions between the two rippled states (cf. § 4.1). One is the Rhomboidal Pyramid State [25] that was subsequently observed by de Mongeot and coworkers, in the epitaxial erosion of Cu(110) and Rh(110) surfaces [33, 35]. In addition, the model captures a number of interesting intermediate states with structural properties somewhere between those of rippled and pyramidal states, including the prominent Rectangular Rippled states of long roof-like objects (huts) seen on Ag(110) surfaces [31, 34]. The model also predicts the existence of a striking interfacial structure that carries nonzero (persistent) surface currents. A periodic vortex pattern of the surface current field, which forms in this Buckled Rippled interface state, is an unusual far-from-equilibrium relative of self-organized convective flow patterns in hydrodynamic systems. The existence of such an unusual surface state shows that the widely accepted assumption of zero surface currents on the selected interface structures is *not* always true.

We conclude by reexamining the phenomenology of multilayer epitaxial growth and erosion on square symmetry (001) crystal surfaces, within our unified model [29]. The 45° pyramid rotation transitions between two major types of four-sided pyramids on (001) surfaces [36] and other related phenomena [37–40] are elucidated. Novel intermediate states involving many-sided pyramids, intervening in these transitions and causing experimentally observed enhanced interface roughening, are predicted and characterized. The effects of the vertical (pyramid-pit) growth asymmetry on the multitude of states on (001) crystal surfaces are also described and clarified.

2. Continuum Modeling

In our continuum modeling of the the dynamics of multilayer epitaxial growth and erosion [4, 41], the evolution of the interface is described by an equation that is gener-

https://doi.org/10.4208/eajam.040411.030611a Published online by Cambridge University Press

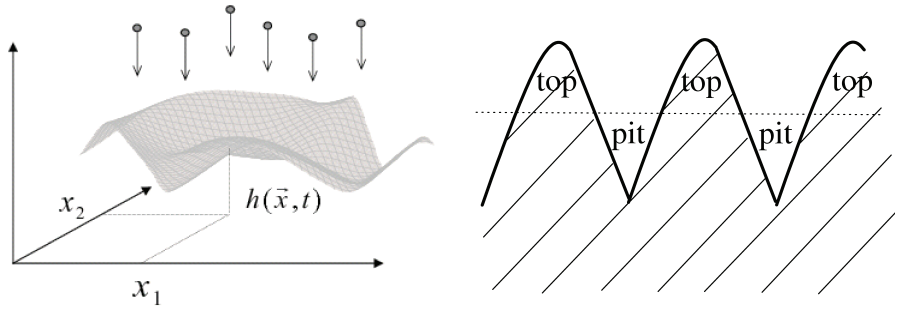

(a) (b) Vertical Asymmetry

Figure 1: (a) Geometry of the surface growth process in epitaxial growth and erosion. (b) Vertical growth asymmetry (VA) induces the difference between the shapes of pyramid tops and bottoms (pits).

ally of the form

$$\frac{\partial h(\mathbf{x},t)}{\partial t} = v(h) \ ,$$

where the local interface height velocity $v(h)$ is a function of the interface height $h(\mathbf{x},t)$ over a base plane and $\mathbf{x} = (x_1, x_2)$ is a two-dimensional base plane vector — cf. Fig. 1(a). In the *absence* of vertical asymmetry (VA), the interface velocity $v(h)$ is an *odd* function of the interface height [$v(-h) = -v(h)$], so under vertical reflection ($h \to -h$) there is dynamical symmetry of the interface evolution equation. However, with such a model there would be no shape difference between pyramids and pyramidal pits (upside-down pyramids) for example. In reality, this difference is always present [cf. Fig. 1(b)], as is VA. Indeed, for realistic interface dynamics models we have $v(-h) \neq -v(h)$, and the interface velocity can be decomposed as

$$v(h) = v_{\rm VS}(h) + v_{\rm VA}(h) \ .$$

Here $v_{\rm VS}(h) = -v_{\rm VS}(-h) = [v(h) - v(-h)]/2$ and $v_{\rm VA}(h) = v_{\rm VA}(-h) = [v(h) + v(-h)]/2$ are the respective odd and even parts of $v(h)$, and the *even* part $v_{\rm VA}(h)$ breaks the vertical reflection ($h \to -h$) symmetry of the interface dynamics to introduce the VA effects. This separation allows us to extract generic VA effects (directly compare results for nonzero VA to those obtained for zero VA), which is virtually impossible in both experiments and microscopic kinetic simulations.

Under typical conditions for epitaxial growth, the height $h(\mathbf{x},t)$ defining the position of the interface (relative to a base plane) obeys a conservation law. All relaxation processes on the surface conserve the deposited volume of growing film in the absence of desorbtion, vacancies or overhangs. Thus in a frame co-moving with the advancing crystal interface, the height evolution equation is of form

$$\frac{\partial h(\mathbf{x},t)}{\partial t} = -\boldsymbol{\nabla}\cdot\mathbf{J} + \eta(\mathbf{x},t) = -\frac{\partial J_1}{\partial x_1} - \frac{\partial J_2}{\partial x_2} + \eta(\mathbf{x},t) \ , \qquad (2.1)$$

https://doi.org/10.4208/eajam.040411.030611a Published online by Cambridge University Press

where $\mathbf{J} = (J_1, J_2)$ is the surface current vector and $\eta(\mathbf{x}, t)$ is the white noise describing the fluctuations of the deposition flux. The average deposition flux has been eliminated from Eq. (2.1) by adopting the co-moving frame of reference, and noise is irrelevant in related coarsening processes such as spinodal decomposition or Ostwald ripening [20]. In the same spirit, the focus of this review is on the dynamics described by Eq. (2.1) for $\eta(\mathbf{x}, t) = 0$. The surface current vector in Eq. (2.1) can generally be decomposed as

$$\mathbf{J} = \mathbf{J}^{\rm NE}(\boldsymbol{\nabla} h) + \mathbf{J}^{(\rm curv)} \ , \tag{2.2}$$

where $\mathbf{J}^{\rm NE}(\boldsymbol{\nabla} h)$ is the non-equilibrium surface current, a function of the local interface slope vector $\mathbf{M} = \boldsymbol{\nabla} h = (M_1, M_2)$ with $M_1 = \partial h/\partial x_1$ and $M_2 = \partial h/\partial x_2$ [4,25–29,41]. It is the most important contribution to the net surface current, and must not only incorporate the effects of the ESV instability but also lead to the slope selection mentioned in the Introduction. Thus for small slopes the non-equilibrium surface current $\mathbf{J}^{\rm NE}(\boldsymbol{\nabla} h)$ is nonzero and up-hill [4], rendering the initially flat interfaces unstable, but it may vanish at some values of the slope vector $\mathbf{M}$. As discussed in this review, *in most but not all situations of interest* the special values of $\mathbf{M}$ where $\mathbf{J}^{\rm NE}(\mathbf{M}) = \mathbf{0}$ correspond to the facet slopes of the surface structures (pyramids, ripples, etc.) that develop across the interface. On the other hand, the "curvature current" contribution $\mathbf{J}^{(\rm curv)}$ in Eq. (2.2) vanishes on flat interfaces ("facets") no matter what slope $\mathbf{M} = \boldsymbol{\nabla} h$ they may have; and it has the form

$$\mathbf{J}^{(\rm curv)} = \mathbf{J}_{\rm SD} + \mathbf{J}_{\rm VA} \ , \tag{2.3}$$

where $\mathbf{J}_{\rm SD} \sim \boldsymbol{\nabla}(\nabla^2 h)$ is a contribution isomorphic to the well known Mullins' surface diffusion current and $\mathbf{J}_{\rm VA}$ is the vertical asymmetry current. The form

$$\mathbf{J}_{\rm VA} \sim \boldsymbol{\nabla} |\boldsymbol{\nabla} h|^2$$

after Villain [4] is even under vertical reflection $h \to -h$, and therefore produces an even contribution to the interface velocity that introduces VA into the interface dynamics represented — cf. Eq. (2.1). The vertical asymmetry current $\mathbf{J}_{\rm VA}$ is reconsidered below.

In contrast to $\mathbf{J}_{\rm VA}$, both the non-equilibrium and Mullins' surface diffusion currents are *odd* under vertical reflection $h \to -h$, so do not contribute any VA. In particular, the non-equilibrium current $\mathbf{J}^{\rm NE}(\boldsymbol{\nabla} h)$, which encodes the significant ESV instability and other effects that stabilize the preferred slopes [18, 19, 25–29, 41], does *not* break the vertical symmetry. Thus with a perpendicular depositing beam incidence, one must have $\mathbf{J}^{\rm NE}(-\mathbf{M}) = -\mathbf{J}^{\rm NE}(\mathbf{M})$ due to the symmetry of major crystal surfaces such as (001), (111) and (110) under the horizontal (base plane) inversion $\mathbf{x} \to -\mathbf{x}$. It follows that the horizontal inversion symmetry *coincidentally* implies that $\mathbf{J}^{\rm NE}$ must *also* change sign under the vertical reflection $h \to -h$ (with $\mathbf{x}$ unchanged), as $\mathbf{M} = \boldsymbol{\nabla} h = \partial h/\partial \mathbf{x}$. Thus the non-equilibrium current $\mathbf{J}^{\rm NE}(\boldsymbol{\nabla} h)$ does *not* introduce any VA, so fundamental growth features such as the values of preferred facet slope vectors (encoded in the form of $\mathbf{J}^{\rm NE}(\boldsymbol{\nabla} h)$ through its stable zeros) are insensitive to VA! One therefore arrives

https://doi.org/10.4208/eajam.040411.030611a Published online by Cambridge University Press

at the striking conclusion that major growth factors, such as the Ehrlich-Schwoebel-Villain instability and slope stabilizing effects modeled by $\mathbf{J}^{\rm NE}(\boldsymbol{\nabla} h)$, do *not* themselves introduce VA in any fundamental way. Nonetheless, VA is *ubiquitous*, with no putative up-down reflection $h \to -h$ symmetry involved in any realistic interface dynamics. Due to VA, the shapes of pyramids and pits are not simply related to each other by up-down reflection, but the potential effects of VA remain uncertain and poorly understood. For example, can VA *alone* produce major qualitative effects on long length scale interface morphologies? As noted above, possible values of preferred facet slope vectors corresponding to the set of stable zeros of $\mathbf{J}^{\rm NE}(\boldsymbol{\nabla} h)$ are insensitive to VA. However, which of these many zeros are selected during interface growth is generally *not* encoded in the form of $\mathbf{J}^{\rm NE}(\boldsymbol{\nabla} h)$, such as the case in Eq. (2.6) below. Unless there are some special restrictions, *not* generic to the epitaxial growth process but arbitrarily imposed on the form of the surface current (e.g., the existence of an effective free energy generating the model dynamics), the selection of preferred facets from the set of *all* allowed facets (corresponding to all stable zeros of $\mathbf{J}^{\rm NE}(\boldsymbol{\nabla} h)$) is *kinetically* decided during the surface evolution. Consequently, kinetic VA effects may play a qualitatively important role in determining the form of the large scale structures of the growing interfaces in epitaxial growth and erosion. Our results reviewed in § 4.2 and § 5 well document this important role of VA.

The form $\mathbf{J}_{\rm VA} \sim \boldsymbol{\nabla}|\boldsymbol{\nabla} h|^2$ mentioned above, which contributes the so-called conservative Kardar-Parisi-Zhang (CKPZ) term $-\boldsymbol{\nabla}\cdot\mathbf{J}_{\rm VA} \sim -\nabla^2|\boldsymbol{\nabla} h|^2$ to the interface velocity in Eq. (2.1), is applicable to isotropic surfaces. However, the contribution depends upon the symmetries of the crystal surface under study, such that $\mathbf{J}_{\rm VA}$ and the corresponding conservative CKPZ term may be more complex. Thus on respecting surface symmetries, for (110) surfaces we find the VA contribution in Eq. (2.1) is a generalised CKPZ term

$$-\boldsymbol{\nabla}\cdot\mathbf{J}_{\rm VA} = -\frac{\lambda_{11}}{2}\left(\frac{\partial}{\partial x_1}\right)^2\left(\frac{\partial h}{\partial x_1}\right)^2 - \frac{\lambda_{12}}{2}\left(\frac{\partial}{\partial x_1}\right)^2\left(\frac{\partial h}{\partial x_2}\right)^2 - \frac{\lambda_{21}}{2}\left(\frac{\partial}{\partial x_2}\right)^2\left(\frac{\partial h}{\partial x_1}\right)^2 - \frac{\lambda_{22}}{2}\left(\frac{\partial}{\partial x_2}\right)^2\left(\frac{\partial h}{\partial x_2}\right)^2 - \frac{\lambda_3}{2}\frac{\partial}{\partial x_1}\frac{\partial}{\partial x_2}\left[\frac{\partial h}{\partial x_1}\frac{\partial h}{\partial x_2}\right], \tag{2.4}$$

This form is again even in h, in contrast to the surface diffusion-like (Mullins) current $\mathbf{J}_{\rm SD}$ for (110) surfaces, which renders in Eq. (2.1) the term

$$-\boldsymbol{\nabla}\cdot\mathbf{J}_{\rm SD} = -\kappa_{11}\left(\frac{\partial}{\partial x_1}\right)^4 h - 2\kappa_{12}\left(\frac{\partial}{\partial x_1}\right)^2\left(\frac{\partial}{\partial x_2}\right)^2 h - \kappa_{22}\left(\frac{\partial}{\partial x_2}\right)^4 h \tag{2.5}$$

that is odd in h. In Eq. (2.5), for the (110) crystal surface the constants $\kappa_{\alpha\beta}$ are generally unequal. The VA contribution to the interface velocity exhibited in Eq. (2.4) is consistent with the symmetries of the (110) surface that require Eq. (2.4) to be invariant under two reflections (i) $(x_1, x_2) \to (-x_1, x_2)$, and (ii) $(x_1, x_2) \to (x_1, -x_2)$, where here and in the following discussion the coordinate axes are directed along the two principal crystallographic directions of (110). For the (110) surfaces, the two

https://doi.org/10.4208/eajam.040411.030611a Published online by Cambridge University Press

principal directions are not coincident, so in Eq. (2.4) the constants $\lambda_{\alpha\beta}$ are unequal such that there are five independent λ-constants. However, for higher symmetry (001) surfaces there is also diagonal reflection symmetry $(x_1, x_2) \to (x_2, x_1)$ [18, 29], which implies $\lambda_{11} = \lambda_{22}$ and $\lambda_{12} = \lambda_{21}$, so for (100) surfaces there are three independent λ-constants in Eq. (2.4). For isotropic surfaces, the term in Eq. (2.4) must be invariant under all 2D rotations, which implies that $\lambda_{11} = \lambda_{12} = \lambda_{21} = \lambda_{22} = \lambda_{\rm VA}$ and $\lambda_3 = 0$. In this case Eq. (2.4) reduces to the simple (single constant) conservative KPZ form

$$-\boldsymbol{\nabla}\cdot \mathbf{J}_{\rm VA} = -\frac{\lambda_{\rm VA}}{2}\nabla^2|\boldsymbol{\nabla} h|^2 \,, \tag{2.4$'$}$$

which is thus strictly applicable *only* to idealized isotropic surfaces.

Let us now proceed to consider the non-equilibrium current $\mathbf{J}^{\rm NE}(\mathbf{M})$, which plays the dominant role in our continuum modeling of epitaxial growth and erosion. The form of $\mathbf{J}^{\rm NE}(\mathbf{M})$ in Eq. (2.2) is also strongly restricted by the orientational symmetries of the crystal surfaces. For any surface symmetry operation S that transforms the slope vector $\mathbf{M}$ into the vector $S\mathbf{M}$, the vector $\mathbf{J}^{\rm NE}$ must transform into the vector $S\mathbf{J}^{\rm NE}$. In other words, for any surface symmetry operation S the functional equation

$$\mathbf{J}^{\rm NE}(S\mathbf{M}) = S\mathbf{J}^{\rm NE}(\mathbf{M})$$

must be satisfied. For example, for (110) surfaces that have the symmetry of a rectangle, all symmetry operations can be generated by the two reflections S_1: $(x_1, x_2) \to (-x_1, x_2)$ and S_2: $(x_1, x_2) \to (x_1, -x_2)$ on taking the coordinate axes to be the two principal axes of the (110) crystal surface. Consequently, the above functional equation implies expansions of the form [25, 26],

$$\begin{aligned} J_1^{\rm NE}(M_1, M_2) &= M_1[r_1 - u_{11}M_1^2 - u_{12}M_2^2 + \cdots], \\ J_2^{\rm NE}(M_1, M_2) &= M_2[r_2 - u_{22}M_2^2 - u_{21}M_1^2 + \cdots] \end{aligned} \tag{2.6}$$

for the (110) surfaces, where the dots indicate higher order terms. Truncating out these higher order terms leads to our simplest comprehensive model [25, 26], consistent with the symmetries of the (110) surface respected by the terms exhibited explicitly in Eq. (2.6).

On the other hand, for (001) surfaces with square symmetry, one also has diagonal reflection symmetry $(x_1, x_2) \to (x_2, x_1)$. This higher symmetry yields the condition $J_1^{\rm NE}(M_1, M_2) = J_2^{\rm NE}(M_2, M_1)$, implying the restrictions $r_1 = r_2$, $u_{12} = u_{21}$ and $u_{11} = u_{22}$ on the parameters in Eq. (2.6), so for (001) surfaces Eq. (2.6) reduces to the form

$$\begin{aligned} J_1^{\rm NE}(M_1, M_2) &= M_1[r - uM_1^2 - buM_2^2 + \cdots] \,, \\ J_2^{\rm NE}(M_1, M_2) &= M_2[r - uM_2^2 - buM_1^2 + \cdots] \end{aligned} \tag{2.7}$$

https://doi.org/10.4208/eajam.040411.030611a Published online by Cambridge University Press

where b is an anisotropy parameter [18, 19]. For the special value $b = +1$, with the terms explicitly displayed in Eq. (2.7) the current acquires the full rotational invariance $\mathbf{J}^{\mathrm{NE}}(S\mathbf{M}) = S\mathbf{J}^{\mathrm{NE}}(\mathbf{M})$, where S is any 2D rotation. Thus for $b = +1$ the model in Eq. (2.7) becomes rotationally invariant (isotropic), and can therefore be used to study isotropic surfaces. For $b < 1$, the current (2.7) has four stable zeros at $[M_1, M_2] = [M_0 \cos(\theta_n), M_0 \sin(\theta_n)]$, with $M_0[2r/u(1+b)]^{1/2}$ and $\theta_n = 45^\circ + (n-1)\cdot 90^\circ$ for $n = 1, 2, 3$, and 4. For $b = +1$, the current vanishes on a continuous set of points constituting a circle in the M-space, with radius $M_0 = [r/u]^{1/2}$. For $b > +1$, the current (2.7) is again anisotropic, but with *new* locations of stable zeros of the current now at $[M_1, M_2] = [M_0 \cos(\theta_n), M_0 \sin(\theta_n)]$, where $M_0 = [r/u]^{1/2}$ and $\theta_n = (n-1)\cdot 90^\circ$ for $n = 1, 2, 3$, and 4. Thus the preferred facets for $b > +1$ are rotated by 45°, with respect to those preferred for $b < 1$. By tuning the anisotropy parameter b, one can go from the square anisotropy regime when $b < +1$ to the other square anisotropy regime when $b > +1$, on crossing through the isotropic point at $b = +1$. The four-sided pyramids and the facet edge networks that form for $b > +1$ are rotated by 45° with respect to those that form for $b < +1$ — cf. Fig. 2, depicting the so-called Phase I interface state from simulations [18]. For $b < +1$, the pyramid edges are parallel to the $x_1 = 0$ and $x_2 = 0$ axes, as seen in the Phase I simulations in Fig. 2; whereas for $b > +1$, the pyramid edges are parallel to the $x_1 - x_2 = 0$ and $x_1 + x_2 = 0$ axes, corresponding to the so-called Phase II where the four-sided pyramids are rotated by 45° with respect to the Phase I pyramids — cf. § 5. Such a 45° pyramid rotational transition between the two major types of four-sided pyramids on (001) surfaces has indeed been observed experimentally on (100) surfaces [36, 37]. Realistic modeling of this transition has required the incorporation of the higher order terms indicated by the dots in Eq. (2.7), leading to the more detailed model introduced in Ref. [29] and discussed in § 5 of this review. (The higher order terms are necessary to remove the artificial isotropic critical point $b = 1$ implied by Eq. (2.7) when the higher order terms are truncated out.)

Let us return to the discussion of the general features of epitaxial growth in the framework of our continuum modeling. A major aspect is the selection of the slope vectors of the faceted morphologies developing across the growing surface. Thus an outstanding question is, what are the slopes of the preferred (selected) facets? It is frequently stated in the literature (without proof) that these slopes correspond to the zeros of the non-equilibrium current $\mathbf{J}^{\mathrm{NE}}(\mathbf{M})$. To examine this point, let us reconsider the model current (2.6) for the (110) surfaces. For the *special* parameter choice $u_{12} = u_{21}$, *not* required by any first principles such as (110) surface symmetry, the $\mathbf{J}^{\mathrm{NE}}(\mathbf{M})$ in Eq. (2.4) becomes a gradient of a potential

$$\mathbf{J}^{\mathrm{NE}}(\mathbf{M}) = -\frac{\partial U(\mathbf{M})}{\partial \mathbf{M}} \,, \tag{2.8a}$$

where the potential is

$$U(M) = -\frac{r_1}{2}M_1^2 - \frac{r_2}{2}M_2^2 + \frac{u_{11}}{4}M_1^4 + \frac{u_{12}}{2}M_1^2 M_2^2 + \frac{u_{22}}{4}M_2^4 \,. \tag{2.8b}$$

https://doi.org/10.4208/eajam.040411.030611a Published online by Cambridge University Press

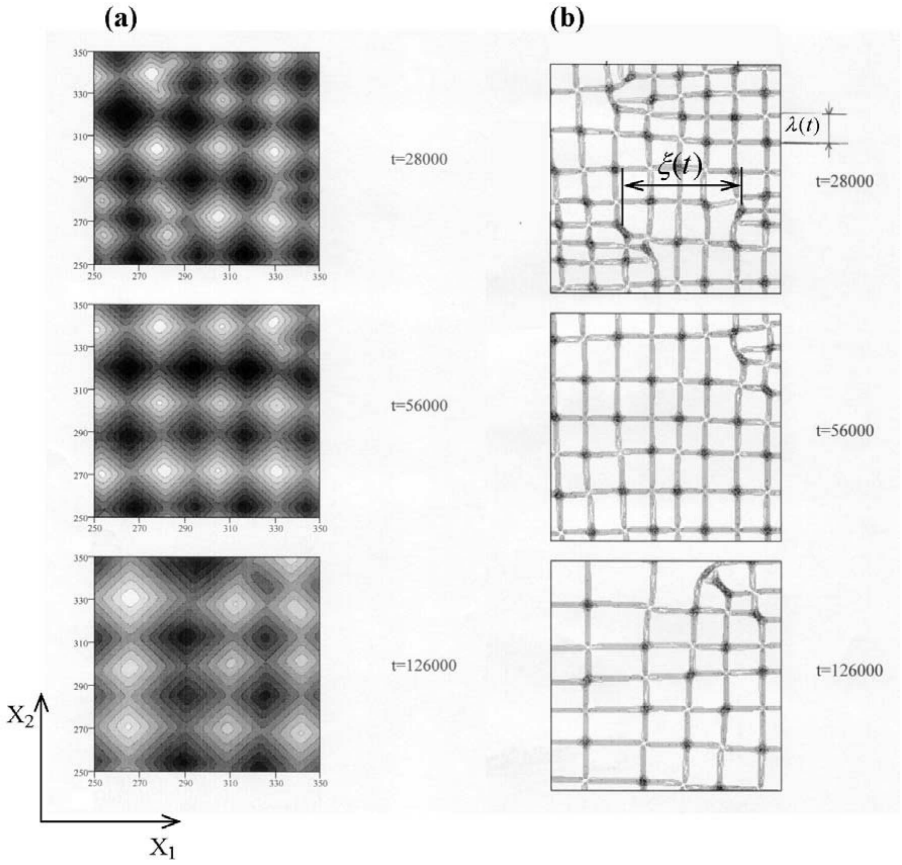

Figure 2: (a) Contour plots giving the time evolution of the square anisotropy (001) surfaces, where a nearly regular lattice of four-sided pyramids forms. (b) Corresponding snapshots of the edge lattice, with dislocations (topological defects of the edge lattice). The dislocations move, and their motion mediates coarsening as discussed in the text. (This figure is reproduced from Ref. [18].)

On the other hand, the interface dynamics equation (2.1) can be shown to be equivalent to

$$\frac{\partial h(x,t)}{\partial t} = -\frac{\delta F_{\rm eff}}{\delta h(x,t)}, \tag{2.9a}$$

provided one makes a more arbitrary assumption — viz. that the vertical asymmetry terms in Eq. (2.4) are ignored. In Eq. (2.9a), the $F_{\rm eff}$ is an *effective* free energy functional of the form $F_{\rm eff}(h) = F_{\rm NE} + F_{\rm SD}$, with

$$F_{\rm NE} = \int d^2x\, U(\mathbf{M}(\mathbf{x})) \tag{2.9b}$$

contributing the non-equilibrium current $\mathbf{J}^{\rm NE}(\mathbf{M})$ via Eq. (2.6) [with $u_{12} = u_{21}$] and

https://doi.org/10.4208/eajam.040411.030611a Published online by Cambridge University Press

Eq. (2.2) to Eq. (2.1), and

$$F_{\rm SD} = \int d^2x \left[\frac{\kappa_{11}}{2} \left(\frac{\partial^2 h}{\partial x_1^2} \right)^2 + \kappa_{12} \left(\frac{\partial^2 h}{\partial x_1 \partial x_2} \right)^2 + \frac{\kappa_{22}}{2} \left(\frac{\partial^2 h}{\partial x_2^2} \right)^2 \right] \tag{2.9c}$$

contributing the surface diffusion $\mathbf{J}_{SD}$ term via Eqs. (2.5) and (2.3) to Eqs. (2.2) and (2.1). We stress that for $u_{12} \neq u_{21}$ there is no $F_{\rm eff}$ that would generate the dynamics via Eq. (2.9a). The selected facet slope vectors are commonly assumed to correspond to the zeros of $\mathbf{J}^{\rm NE}(\mathbf{M})$, but there are known exceptions to this "zero current rule" [25, 26]. Indeed, this rule *necessarily* holds only for the surface dynamics governed by an effective free energy. Thus from Eq. (2.9a) it can be shown that

$$\frac{dF_{\rm eff}}{dt} = -\int d^2x \left(\frac{\partial h}{\partial t} \right)^2 \leqslant 0 \,, \tag{2.10}$$

so $F_{\rm eff}$ generally decreases with time. This energy minimization is achieved by the interface breaking up into nearly flat (vicinal) *growing* facets: on a flat facet the surface diffusion "free energy" $F_{\rm SD} \geqslant 0$ given by Eq. (2.9c) reduces to zero, whereas the non-equilibrium current "free energy" $F_{\rm NE}$ given by Eq. (2.9b) is minimized by selecting the slopes that minimize the local potential $U(\mathbf{M})$. Thus from Eq. (2.8a), $\mathbf{J}^{\rm NE} = 0$ at the slope vectors of the selected facets, so the slope vector $\mathbf{M} = \boldsymbol{\nabla} h$ plays the role of the order parameter in the effective free energy $F_{\rm eff}$ that favors the development of growing facets with preferred slope. The effective free energy *in excess* of its absolute minimum is localized at the edges between the selected facets [18, 28]. An edge of length l contributes the excess effective free energy proportional to its length — i.e.

$$\Delta F_{\rm eff} = \sigma l \,, \tag{2.11}$$

where σ is the edge line tension easily calculated for static edges ($\partial h/\partial t = 0$) between various types of facets [18, 28]. During the surface coarsening process, the facets grow and the total length of all the edges present on the surface decreases in time, yielding a decrease of $F_{\rm eff}$ in accord with the inequality in Eq. (2.10). Thus the interface coarsening dynamics in the epitaxial growth can also be viewed as a process of *edge extinction*, as originally emphasized in [18] — cf. Figs. 2, 3 and 4 here. This allowed us to provide simple analytic explanations for the coarsening laws observed in numerous experiments and simulations on crystal surfaces with various symmetry — cf. § 3.

Indeed, the often presumed vanishing of the non-equilibrium current on preferred facets, a major feature frequently attributed to the multilayer epitaxial growth, is actually only mandatory for models with an underlying effective free energy. In its absence, the vanishing of the non-equilibrium current on preferred facets (although still possible) is *no longer* mandatory. Further, by lifting the restriction $u_{12} = u_{21}$, which is not required by the (110) surface symmetry, our studies of the model (2.6) revealed the existence of the so-called Buckled Rippled interface state that carries nonzero (persistent) surface currents [25, 26] — cf. § 4.1. This state exhibits a periodic arrangement

https://doi.org/10.4208/eajam.040411.030611a Published online by Cambridge University Press

of surface current vortices, reminiscent of self-organized convective flow patterns in hydrodynamic systems. The existence of the Buckled Rippled interface state on the rectangular symmetry (110) surfaces (where $u_{12} \neq u_{21}$, so no effective free energy) shows that the frequently stated "axiom" of zero surface current on the selected interface structures is *not* generally true. On the other hand, the diagonal symmetry of the square symmetry (001) surfaces implies the condition $u_{12} = u_{21}$ and the non-equilibrium current of the form in Eq. (2.7), as noted above. In the absence of the higher order terms indicated by the dots in Eq. (2.7), this current is generated by the potential given in Eq. (2.8b), which for (001) surfaces reduces to

$$U(M_1, M_2) = -\frac{r}{2}\left[(M_1)^2 + (M_2)^2\right] + \frac{u}{4}\left[(M_1)^4 + (M_2)^4 + 2b(M_1)^2(M_2)^2\right] \qquad (2.12a)$$

that may be rewritten in terms of polar coordinates $(M_1 = M\cos\theta, M_2 = M\sin\theta)$ as

$$U(M, \theta) = -\frac{r}{2}M^2 + \frac{u(3+b)}{16}M^4 + \frac{u(1-b)}{16}M^4\cos 4\theta \ , \qquad (2.12b)$$

where r, u and b are the parameters in Eq. (2.7). We note that the anisotropy parameter b must satisfy the condition $b > -1$ to ensure that the local potential given by (2.12b) is bounded from below. For $b = +1$, this potential depends only on the slope magnitude and becomes isotropic (θ-independent), yielding the pyramidal growth seen in Fig. 3 with the coarsening exponent $n_c = 1/3$ [18] — cf. § 3.1. From Eq. (2.12b), for any $b \neq 1$ the potential has eight extremes (four minima and four saddle points), when from Eq. (2.8a) the non-equilibrium current vanishes. For $b < 1$, the local potential given by (2.12b) has four stable minima at $[M_1, M_2] = [M_0\cos(\theta_n), M_0\sin(\theta_n)]$, with $M_0[2r/u(1+b)]^{1/2}$ and $\theta_n = 45^0 + (n-1)\cdot 90^\circ$ for $n = 1, 2, 3$, and 4, yielding the pyramidal growth seen in Fig. 2 where the coarsening exponent is $n_c = 1/4$ [18,19] — cf. § 3.2. For $b = +1$, the energy minimum set degenerates into the circle with radius $M_0 = [r/u]^{1/2}$, reflecting that the model becomes isotropic for this special value of b. For $b > +1$, the model potential given by (2.12b) is again anisotropic however, with new locations of the potential minima at $[M_1, M_2] = [M_0\cos(\theta_n), M_0\sin(\theta_n)]$, where $M_0 = [r/u]^{1/2}$ and $\theta_n = (n-1)\cdot 90^\circ$ for $n = 1, 2, 3$, and 4. All of these observations directly correspond to those made below Eq. (2.7), in terms of the non-equilibrium current zeros. However, the description in terms of the potential $U(\mathbf{M})$ makes it easy to examine the stability properties of the various current zeros, and to directly determine which of them are stable — i.e. represent the minima of the effective free energy eventually reached by the system due to the dynamical energy minimization [cf. Eq. (2.7)]. The preferred value of the slope thus corresponds to the minimum of the local potential $U(\mathbf{M})$. Consequently, the slope vector $\mathbf{M} = \boldsymbol{\nabla} h$ is an order parameter of the effective free energy F_{eff}, which favors the development of growing facets with preferred slope. Within the effective free energy framework, the development of growing pyramids with facets of preferred slope can thus be viewed as a phase ordering process, similar to those seen in magnetic systems [20]. Pyramid facets are analogous to magnetic domains that grow as some power of the time, with edges between two facets

https://doi.org/10.4208/eajam.040411.030611a Published online by Cambridge University Press

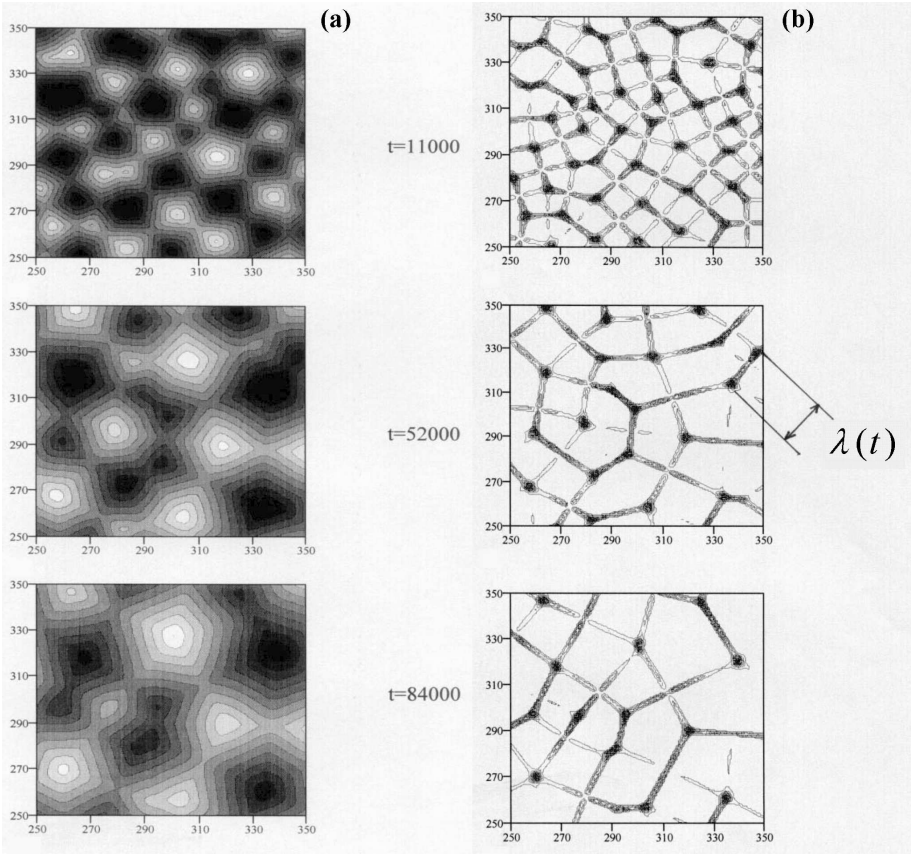

Figure 3: (a) Contour plots giving the time evolution of the isotropic surface, where nearly flat facets bounded by edges are evident. (b) Corresponding snapshots of the edge network. There are no preferred directions for the orientation of the edges. The structural length-scale of the edge network $\lambda(t)$, comparable to the facet size or lateral pyramid size, grows in time. (This figure is reproduced from Ref. [18].)

analogous to the domain walls between two magnetically ordered domains, so edge extinction resembles the extinction of the magnetic domain walls [20]. Importantly, it *is* the extinction of facet edges favored by the effective free energy minimization implied by Eq. (2.10) that governs the interface coarsening dynamics — cf. § 3 and § 4.3 of this review.

If the local potential U were only to depend upon the magnitude of the slope $|\mathbf{M}|$, i.e. $U(\mathbf{M}) = U(|\mathbf{M}|)$, by this rotational symmetry the non-equilibrium current would vanish on a circle in the order parameter space (M_1,M_2). Such an isotropic model is certainly not realistic for the growth on real crystalline surfaces. For realistic surfaces with hexagonal or quadratic symmetry, the local potential depends on both the magnitude $|\mathbf{M}|$ and the polar angle θ of $\mathbf{M}$, as exemplified above by the model potential in Eq. (2.12). Thus a realistic $U(\mathbf{M})$ may only have a *discrete* set of minima; and for the hexagonal symmetry (111) crystal surfaces the local potential has the symmetry

https://doi.org/10.4208/eajam.040411.030611a Published online by Cambridge University Press

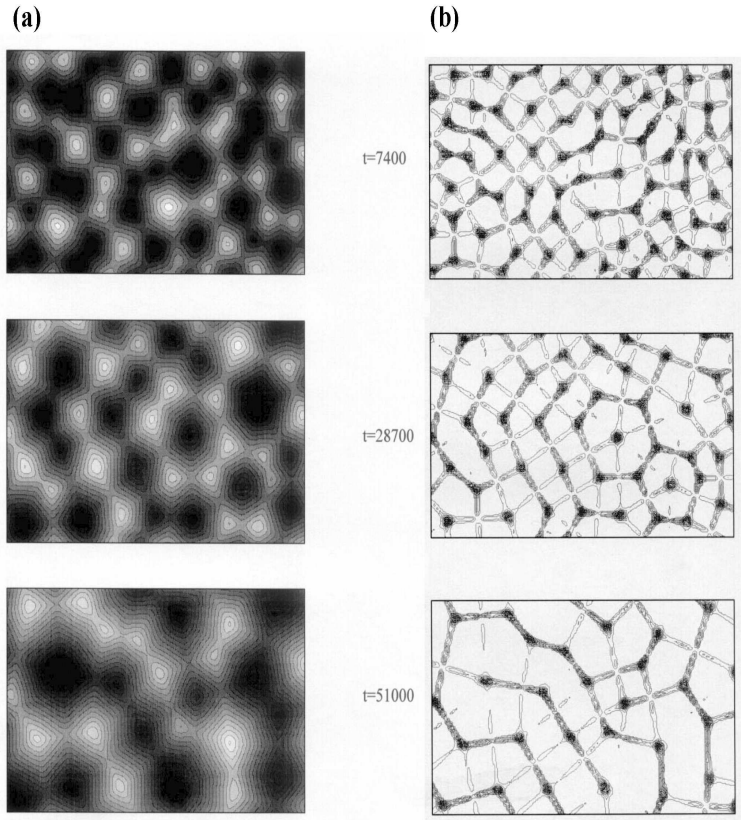

Figure 4: (a) Contour plots that depict the time evolution of the hexagonal symmetry (111) surfaces. Note the presence of facets bounded by edges. (b) The edge network on a small portion of the growing surface for the hexagonal symmetry surfaces, where the edge orientations are mastered by the six-fold anisotropy of the (111) surface. (This figure is reproduced from Ref. [18].)

property

$$U(\mathbf{M}) = U(|\mathbf{M}|, \theta) = U\left(|\mathbf{M}|, \theta + \frac{2\pi}{6}\right) , \tag{2.13}$$

hence $U(\mathbf{M})$ must have (at least) six minima corresponding to six preferred facet orientations that may appear in the growth process — cf. Fig. 4. Likewise, for surfaces that have square symmetry such as the (100) surface, the local potential has the symmetry property

$$U(\mathbf{M}) = U(|\mathbf{M}|, \theta) = U\left(|\mathbf{M}|, \theta + \frac{2\pi}{4}\right) , \tag{2.14}$$

when $U(\mathbf{M})$ must have (at least) four minima, corresponding to four preferred orientations of the facets that may appear in the growth process on this type of surface.

In § 3, we review the results obtained in Ref. [18] from the effective free energy modeling for the case of high symmetry (001) and (111) crystal surfaces — and also for idealized isotropic surfaces that appear at special critical points, such as $b = +1$ in

https://doi.org/10.4208/eajam.040411.030611a Published online by Cambridge University Press

the model potential in Eq. (2.12). However, the assumption of an effective free energy limits the generality of the modeling, by imposing the condition (2.8a) on the form of the non-equilibrium current vector, equivalent to the constraint

$$\frac{\partial J_i^{\rm NE}}{\partial M_j} = \frac{\partial J_j^{\rm NE}}{\partial M_i} \tag{2.15}$$

on the components of the non-equilibrium current ($i, j = 1, 2$). For $i = j$, Eq. (2.15) is obviously identically satisfied — but not generally for $i \neq j$ on realistic crystal surfaces, as there is then no physical or symmetry reason for that. However, the inequality

$$\frac{\partial J_1^{\rm NE}}{\partial M_2} \neq \frac{\partial J_2^{\rm NE}}{\partial M_1} \tag{2.16}$$

should generally hold. With the model current given by Eq. (2.6) for (110) surfaces, a particular consequence is that $u_{12} \neq u_{21}$, leading to the existence of the unusual Buckled Rippled state that carries nonzero surface current [25,26] — cf. § 4.1. In this state, *none* of the zeros of $\mathbf{J}^{\rm NE}(\mathbf{M})$ is stable, so none of the zeros can be selected [18]. The situation where all zeros of $\mathbf{J}^{\rm NE}(\mathbf{M})$ are unstable cannot be realized within a model where the non-equilibrium current is generated by an effective potential, as in Eq. (2.8a). Other interesting effects related to the nonexistence of an effective free energy can emerge due to the vertical growth asymmetry. We recall that vertical asymmetry contributions from Eq. (2.4) in the interface evolution equation cannot be incorporated into the dynamics of the form given by Eq. (2.9a), governed by effective free energy. Interesting physical phenomena induced by these VA terms, and also the non-equilibrium current terms violating Eq. (2.15), indeed arose in simulations [27,29]. We review our results on these effects in § 4 for (110) surfaces, and in § 5 for (001) surfaces.

3. Interface Coarsening as the Extinction of Facet Edges

In this section, we discuss major concepts and physical ideas that emerged from simulations of interface dynamics in the epitaxial growth on (111) and (001) surfaces and also on isotropic surfaces [18], based on the dynamics governed by an effective free energy. As mentioned in the Introduction, numerous experiments on (111) and (001) surfaces produce the coarsening exponents obtained in Ref. [18] within the effective free energy framework. (We defer until § 4 and § 5 a discussion of effects that cannot be incorporated within the effective free energy framework, as under some conditions these effects are irrelevant for the long time scale dynamics of interface coarsening.)

3.1. Coarsening of isotropic surfaces and (111) crystal surfaces

The simulations of Ref. [18] indicated that the epitaxial growth on both isotropic and hexagonal symmetry (111) surfaces exhibits a scaling behavior characterized by

https://doi.org/10.4208/eajam.040411.030611a Published online by Cambridge University Press

the presence of a single characteristic length-scale — viz. the pyramid size $\lambda(t)$, growing in time according to a power law $\lambda \sim t^{n_c}$. The simulations suggest that the growth of this characteristic length scale is governed by the same coarsening exponent $n_c \cong 1/3$ for both isotropic and hexagonal symmetry (111) surfaces [18]. A major outcome of these simulations was that they motivated a simple kinetic theory to qualitatively explain this scaling behavior. This theory assumes (corroborated by the simulations) that the effective free energy of the growing interfaces is localized within edge networks that form across the interface, both with and without (hexagonal) spatial anisotropy present — cf. Figs. 3 and 4. The central theoretical idea here is to relate the dynamics of the coarsening process to the rate of extinction of the effective free energy rich regions, which are the edges between the facets of the growing pyramids. This is illustrated in Figs. 3 and 4 from the simulations, depicting the interface in terms of the density of the effective free energy discussed in § 2. The free energy in excess of the free energy minimum indeed appears to be localized in the facet edges and described by Eq. (2.11). The effective free energy per unit cell (pyramidal motif) of this edge network, with the cell base size $\approx \lambda(t) \sim$ typical pyramid size, is localized in the few facet edges of a single pyramid. From Eq. (2.11), the effective free energy of an edge with typical length λ is proportional to the length of the edge — i.e.

$$F_{\rm edge} = \sigma\lambda \,, \tag{3.1}$$

where σ is the edge line tension. As there is about one edge per area $\sim \lambda^2$ (cf. Figs. 3 and 4), the effective free energy per unit base area is

$$F_{\rm u.a.} = \frac{F_{\rm eff}}{A_{\rm B}} \approx \frac{F_{\rm edge}}{\lambda^2} = \frac{\sigma}{\lambda} \,, \tag{3.2}$$

where $A_{\rm B}$ denotes the base area of the film. Next, we invoke Eq. (2.10), which implies the decay rate of the effective free energy density (per unit area) is proportional to the spatial average of the squared interface velocity — i.e.

$$\frac{d}{dt}\frac{F_{\rm eff}}{A_{\rm B}} = -\frac{\int (\partial h/\partial t)^2 \, d^2x}{A_{\rm B}} \tag{3.3}$$

or

$$\frac{d}{dt}F_{\rm u.a.} = -\left\langle \left(\frac{\partial h}{\partial t}\right)^2 \right\rangle \,. \tag{3.4}$$

Estimating the typical velocity of the interface as $\langle(\partial h/\partial t)^2\rangle \approx (dw/dt)^2$ where w is the pyramid height, from Eq. (3.2) and Eq. (3.4) we obtain

$$\frac{d}{dt}\left(\frac{\sigma}{\lambda}\right) = -\left(\frac{dw}{dt}\right)^2 \,.$$

Then since $w/\lambda = M_0$ is the preferred slope, we have

$$\frac{d}{dt}\left(\frac{M_0\sigma}{w}\right) = -\left(\frac{dw}{dt}\right)^2 \,, \tag{3.5}$$

https://doi.org/10.4208/eajam.040411.030611a Published online by Cambridge University Press

which for $M_0\sigma$ constant yields on integration

$$w = M_0\lambda = \text{const.}\,(M_0\sigma)^{1/3}\,t^{1/3}\ . \tag{3.6}$$

Thus for isotropic (111) surfaces, we obtain the coarsening scaling law

$$w \sim \lambda \sim t^{1/3}\ , \tag{3.7}$$

with coarsening exponent $\beta = n_c = 1/3$ in accord with the simulation results for the growth of interface roughness $< h^2 >^{1/2} \sim w \sim t^{\beta}$ and the pyramid size $\lambda \sim t^{n_c}$ [18].

It is illuminating to discuss similarities and differences between MBE growth and phase ordering processes, such as the domain growth in magnetic systems [20]. In MBE growth with slope selection, the interface slope vector $\mathbf{M} = \boldsymbol{\nabla} h$ develops a nonzero value and thus plays the role of an order parameter. The facets with preferred slopes that develop in the MBE growth are analogous to magnetically ordered growing domains in the phase ordering process of discrete symmetry magnetic systems, such as the Ising and *anisotropic* XY models. The analogue to a domain wall between two magnetic domains is an edge that occurs at the intersection of two nearly flat facets with different slope vectors, say $\mathbf{M}_1$ and $\mathbf{M}_2$. An edge appears as a straight line segment, as shown in Figs. 2–4, directed along the vector $\mathbf{M}_1 + \mathbf{M}_2$ [18]. Both simulations and the above analytic results call for a cautious comparison of MBE growth with the phase ordering phenomena in standard magnetic systems. For example, the scaling law in Eq. (3.7) with coarsening exponent 1/3 is the same as that for the conserved (type B) Ising dynamics — cf. the well known Lifshitz-Slyozov law [20]. However, this hardly explains why we *also* have the 1/3 exponent for an *isotropic* local potential $U(\mathbf{M})$ that is invariant with respect to rotations of the slope vector $\mathbf{M}$. Although the isotropic MBE model is more like the isotropic X-Y model than an Ising model, the conserved (type B) dynamics of an isotropic X-Y model has a coarsening exponent of 1/4 [20] — and so fails to provide an understanding of the 1/3 coarsening law that we find for the isotropic MBE growth.

The physical origin of this difference between the isotropic MBE model and the XY model is that the vector order parameter $\mathbf{M}$ for the MBE case is a gradient of another field — viz. the interface height $h(x)$. In the absence of this constraint, for the isotropic case the effective free energy in Eq. (2.12) would simply reduce to that of an X-Y model. The isotropic X-Y model has *smeared* domain boundaries with a completely de-localized free energy density [20], with the average free energy density given by $F_{\text{u.a.}} \sim 1/\lambda^2$ rather than the law in Eq. (3.2). However, the situation substantially changes in the interface dynamics models due to the constraint $\mathbf{M} = \boldsymbol{\nabla} h$. The domain boundaries then generally form as narrow domain walls, with the edges carrying essentially all the effective free energy of the system. This *free energy localization*, similar to that in Ising systems, eventually yields the law $F_{\text{u.a.}} \sim 1/\lambda$ as in Eq. (3.1), which is crucial for obtaining the 1/3 coarsening law in Eq. (3.7). Unlike the situation in magnetic

https://doi.org/10.4208/eajam.040411.030611a Published online by Cambridge University Press

systems, free energy localization in the epitaxial interface dynamics model (i.e. the existence of facets bounded by sharp, narrow edges) is *by no means* conditioned by the presence of anisotropies. Indeed, the narrow edges where the free energy is localized and the associated 1/3 coarsening power law arise even for isotropic MBE growth, as documented by the simulations [18]. A long edge is simply a stable stationary solution of the evolution equation (2.9a), for which $\delta F_{\rm eff}/\delta h = 0$. This equation has solutions in the form of *even* narrow edges, for the analytic isotropic MBE growth models in Ref. [18]. This feature is in marked contrast to ordinary X-Y systems, where sharp domain walls may form *only* in the presence of anisotropies. However, an isotropic MBE model has narrow domain walls (edges) and energy localization *even in the absence of spatial anisotropies*, such as the hexagonal anisotropy of (111) crystal surfaces. The observed 1/3 - coarsening power for the isotropic MBE model is a direct consequence of this energy localization, implying $F_{\rm u.a.} \sim 1/\lambda$ rather than $F_{\rm u.a.} \sim 1/\lambda^2$ in the isotropic X-Y model, where there is the 1/4 coarsening law for conserved (type B) dynamics.

How does the presence of anisotropies affect this 1/3 coarsening power law? The crucial feature is that $F_{\rm edge} \sim \lambda$, so $F_{\rm u.a.} \sim 1/\lambda$ cannot be altered by the presence of anisotropies because the edges are narrow (so free energy is localized), even for zero anisotropy. Thus one could expect that the 1/3 coarsening power law may be preserved in the presence of anisotropies, as is apparently the case for the *hexagonal* anisotropy from the simulations [18]. For this case, the main effect of the anisotropy is to orient the already (for zero anisotropy) narrow edges. Nonetheless, the resulting edge networks are still essentially random as in the isotropic case — cf. Figs. 3 and 4. No strong constraints on the edge dynamics are imposed in such random networks, and the coarsening on the hexagonal anisotropy (111) surfaces varies with the same power law Eq. (3.7) as in the isotropic case. On the other hand, as discussed in the next section, *square anisotropy* present on the (001) surfaces may induce the formation of a more regular edge structure (the "edge crystal" seen in Figs. 2 and 5), which imposes special constraints on the dynamics of the edge networks. In such circumstances, the basic 1/3 coarsening power law may break down, as detailed below.

3.2. Coarsening of (001) crystal surfaces

In marked contrast to (111) surfaces, the simulations of (001) surfaces show that the pyramids and their facet edges form nearly perfect square lattices disordered by irregularly placed topological defects — cf. Figs. 2 and 5. Simulations have shown that these defects are dislocations of the edge lattices, and that the presence of the dislocations is crucial for the coarsening of the square symmetry (001) surfaces [18]. Without the dislocations, the edge network would form a regular square lattice, an "edge crystal" with the lattice constant $\lambda(t)$. The simulations show the presence of dislocations that systematically *move* (drift) through this edge lattice — cf. Figs. 2 and 5.

As discussed below, the dislocation drift is caused by the line tension of the edges

https://doi.org/10.4208/eajam.040411.030611a Published online by Cambridge University Press

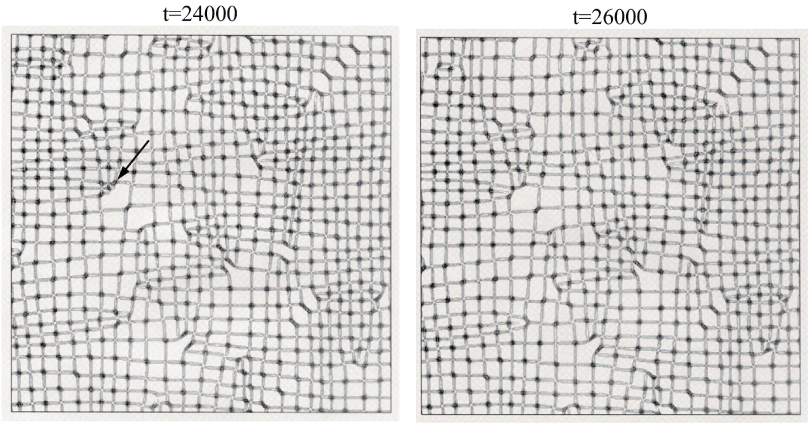

Figure 5: A portion of the network of ridges of the square anisotropy (001) surfaces at two different times. Note the presence of two dislocation ensembles, where one moves horizontally whereas the other moves vertically. The arrow points to an unstable bound state between the two dislocations moving in different directions.

terminating at the dislocation core. Importantly, the drift motion of the dislocations mediates the coarsening process — i.e. the edge lattice constant $\lambda(t)$ increases with time, as can indeed be seen from the dislocation in the upper part of Fig. 2. This dislocation apparently moves to the right, via a gradual extinction (collapse) of two horizontal lines of edges terminating at the dislocation core (cf. Fig. 2). In effect, the *total* length of the edges in the system decreases and pyramid facets then grow. Note the presence of *larger* facets just to the left of the dislocation core, and *smaller* facets to the right of the dislocation. As the two horizontal edges terminating at the dislocation core collapse, three smaller facets transform into one larger facet, and at the same time the dislocation moves to the right. Thus the interface coarsening process is mediated by the dislocation motion [18]. Another striking result from these simulations is that the growth on the square symmetry (001) surfaces exhibits a multi-scaling behavior, as there are two characteristic length-scales that grow in time with two different coarsening exponents. One is $\lambda(t) \sim$ pyramid lateral size $\sim$ pyramid height, growing with the coarsening exponent $n_c \cong \beta \cong 0.25$ [18]. The other length scale $\xi(t)$ is the distance between the dislocations in the same row of the edge lattice (cf. Figs. 2 and 6), and this scale grows faster with a different exponent $n_\xi \cong 0.50$ [18]. Kinetic scaling theory explains these coarsening exponents for the square symmetry (001) surfaces [18]. The theory shows that dislocation climbing and annihilation processes occurring across the edge network are essential to our understanding of the coarsening dynamics on (001) crystal surfaces. Other possible dislocation processes, such as dislocation-pair production or the occasional formations of unstable bound states between two dislocations moving in different directions (one vertically, the other horizontally — cf. Fig. 5), do not significantly affect the coarsening. Indeed, a significant dislocation production only occurs during the initial (pre-coarsening) stage of the growth. Subsequent production of new dislocations is energetically hindered, as that would introduce new

https://doi.org/10.4208/eajam.040411.030611a Published online by Cambridge University Press

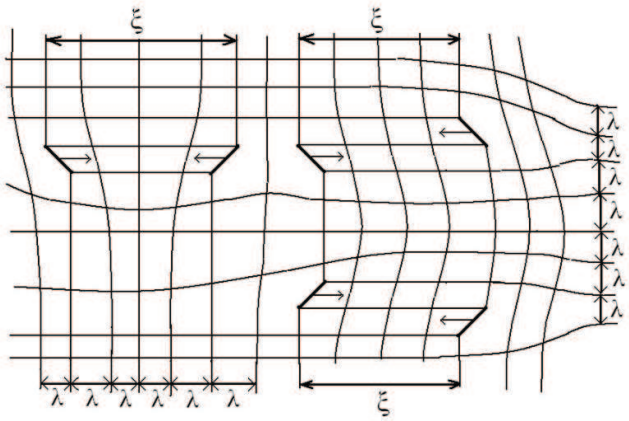

Figure 6: A schematic representation of the moving dislocations of the edge lattice. Note that a dislocation may annihilate with an anti-dislocation moving either in the same row (cf. the left side of the figure) or in a neighboring row of the edge lattice, either above or below the row where the dislocation is moving (cf. the right side of the figure). This gives rise to $q = 3$ channels for dislocation annihilations, employed in the kinetic theory of the interface coarsening dynamics of (001) surfaces.

pyramid edges and cause an increase in the effective free energy. The coarsening on square symmetry (001) surfaces is then identified as the extinction of pyramid edges and facets, mediated by drifting dislocations, where the rate of extinction crucially depends on the number of dislocations present across the interface. During the interface coarsening process, the total number of dislocations decreases with time due to their annihilations with other dislocations.

The usual assumption that there is only one coarsening length scale in epitaxial growth was not really questioned prior to our work [18], where we produced a kinetic theory for the coarsening process on (001) surfaces that carefully takes into account the existence of two large length scales, $\lambda(t)$ and $\xi(t)$. This theory explains the coarsening exponents for the pyramid size, $\lambda \sim t^{n_c}$ with $n_c \approx \beta \approx 1/4$, reported in previous simulations and in experiments on (001) surfaces. It is directly motivated by the observation from the simulations that the coarsening on square symmetry surfaces is mediated by the *moving* dislocations of the edge lattice. The edge lattice coarsens during the motion of the dislocations along the x_1 or x_2 directions. Because the two dislocations ensembles moving along these two different directions are weakly interacting with each other (and are thus nearly statistically independent), it is sufficient to focus attention on only one of them — the dislocations moving along the x_1-direction, say. Let $N_{\rm d}$ denote the total number of these dislocations, which is nearly one half of the total number of all dislocations. Their surface density per unit base area is thus

$$n_{\rm d} = \frac{N_{\rm d}}{A_{\rm B}}, \tag{3.8}$$

where $A_{\rm B}$ denotes the base area of the film as before. The length-scale ξ is the average

https://doi.org/10.4208/eajam.040411.030611a Published online by Cambridge University Press

distance between the dislocations in the *same* lattice row of the height λ, as shown schematically in Fig. 6. There is just one dislocation on a rectangle with height λ and width ξ (cf. Fig. 6), so $n_{\rm d}\lambda\,\xi = 1$ such that

$$n_{\rm d} = \frac{1}{\lambda\,\xi}\ . \tag{3.9}$$

Let L denote the *total* length of the edges directed along the x_1-direction. On an L_1-by-L_2 substrate ($A_{\rm B} = L_1 \cdot L_2$), one has $L = L_1 \times$ number of rows $= L_1(L_2/\lambda)$, so that

$$L = \frac{A_{\rm B}}{\lambda}\ . \tag{3.10}$$

During the motion of each dislocation with velocity $\mathrm{v_d}$, the length L decreases during the time interval dt by the amount equal to $2\,\mathrm{v_d}\,dt$. (The factor of 2 is due to the two lines of edges along the x-direction terminating at each dislocation core — cf. Fig. 6.) As there are $N_{\rm d}$ dislocations and anti-dislocations moving in the x_1 direction, the total change of L is $dL = -N_{\rm d}\,2\,\mathrm{v_d}\,dt$, so that

$$\frac{dL}{dt} = -2\,N_{\rm d}\,\mathrm{v_d}\ . \tag{3.11}$$

From Eqs. (3.8), (3.10) and (3.11) one readily obtains

$$-\frac{1}{\lambda^2}\frac{d\lambda}{dt} = -2\,n_{\rm d}\,\mathrm{v_d}\ , \tag{3.12}$$

where Eq. (3.9) gives the dislocation density $n_{\rm d}$, whence

$$\frac{1}{\lambda}\frac{d\lambda}{dt} = \frac{2\,\mathrm{v_d}}{\xi}\ . \tag{3.13}$$

The total number of the dislocations $N_{\rm d}$ decreases in time, due to annihilations with anti-dislocations (cf. Fig. 6), so we can write $(1/N_{\rm d})dN_{\rm d}/dt = -1/\tau$ or

$$\frac{1}{n_{\rm d}}\frac{dn_{\rm d}}{dt} = -\frac{1}{\tau}\ , \tag{3.14}$$

where τ demotes the mean lifetime of a dislocation before it annihilates with an anti-dislocation. For example, a dislocation/anti-dislocation pair moving in the same row with relative velocity $2\,\mathrm{v_d}$ (cf. Fig. 6) annihilates after a typical time $\tau = \xi/(2\,\mathrm{v_d})$, so on taking into account only one such annihilation channel one would obtain

$$\frac{1}{\tau} = \frac{2\,\mathrm{v_d}}{\xi}\ . \tag{3.15}$$

However, although the anti-dislocation moves in the same row as the dislocation, it may also annihilate with anti-dislocations moving in the rows immediately *above* and *below* it (cf. Fig. 6), so there are actually $q = 3$ channels of dislocation annihilation. The

https://doi.org/10.4208/eajam.040411.030611a Published online by Cambridge University Press

total rate of annihilations is therefore 3 times bigger than given by Eq. (3.15), so (with $q = 3$)

$$\frac{1}{\tau} = q\frac{2\,\mathrm{v_d}}{\xi}\ . \tag{3.16}$$

From Eqs. (3.14) and (3.16),

$$\frac{1}{n_\mathrm{d}}\frac{dn_\mathrm{d}}{dt} = -q\frac{2\,\mathrm{v_d}}{\xi}\ , \tag{3.17}$$

so from Eqs. (3.9) and (3.17) we have

$$-\frac{1}{\xi}\frac{d\xi}{dt} - \frac{1}{\lambda}\frac{d\lambda}{dt} = -q\frac{2\,\mathrm{v_d}}{\xi}\ , \tag{3.18}$$

and hence from Eq. (3.13)

$$\frac{1}{\xi}\frac{d\xi}{dt} = (q-1)\frac{2\,\mathrm{v_d}}{\xi} = (q-1)\frac{1}{\lambda}\frac{d\lambda}{dt}\ . \tag{3.19}$$

Thus from (3.19) we have

$$\frac{(1/\xi)\,d\xi/dt}{(1/\lambda)\,d\lambda/dt} = \frac{d(\ln\xi)}{d(\ln\lambda)} = q-1\ ,$$

and integrating this equation yields

$$\xi \sim \lambda^{q-1} \tag{3.20}$$

— i.e. $\xi \sim \lambda^2$ with $q = 3$. To proceed, we invoke

$$\mathrm{v_d} \sim \frac{1}{\lambda^2}, \tag{3.21}$$

which states that the dislocation velocity on (001) surfaces is inversely proportional to the square of the lattice constant λ of the edge lattice, as discussed at the end of this section and (in a different way) in § 4.3. Thus Eqs. (3.13) and (3.21) yield

$$\frac{1}{\lambda}\frac{d\lambda}{dt} = \frac{2\mathrm{v_d}}{\xi} \sim \frac{1}{\xi\lambda^2}\ , \tag{3.22}$$

and hence from (3.20)

$$\frac{1}{\lambda}\frac{d\lambda}{dt} \sim \frac{1}{\lambda^{q+1}}\ . \tag{3.23}$$

Integrating Eq. (3.23) yields

$$\lambda(t) \sim t^{n_c}\ , \tag{3.24}$$

and from (3.20) and (3.24) we have another scaling relation

$$\xi(t) \sim t^{n_\xi}\ , \tag{3.25}$$

https://doi.org/10.4208/eajam.040411.030611a Published online by Cambridge University Press

so respectively

$$n_c = \frac{1}{q+1}\,, \tag{3.26}$$

$$n_\xi = \frac{q-1}{q+1}\,. \tag{3.27}$$

On recalling that there are three channels of dislocation annihilations ($q = 3$), we get the following values for the coarsening exponents:

$$n_c = \frac{1}{4} \qquad \text{and} \qquad n_\xi = \frac{1}{2}\,. \tag{3.28}$$

These analytically derived values agree with the results obtained from the numerical simulations of MBE growth on square anisotropy surfaces [18]. We note that the average distance $d = 1/\sqrt{n_{\rm d}}$ between dislocations in *any* direction differs from the length-scale ξ, which measures the average distance between neighboring dislocations in the same row of the edge lattice (i.e. along the x-axis). Indeed, $d = \sqrt{\xi\,\lambda}$ from (3.9), and hence $d \sim t^\delta$ with $\delta = (n_\xi + n_\lambda)/2 = 3/8$.

We noted in Eq. (3.21) that the dislocation velocity $\mathrm{v_d}$ is inversely proportional to the square of the lattice constant λ at the edge lattice. To derive this, consider the core of the dislocation in Fig. 2, of size $\sim \lambda$. One has $\mathrm{v_d} = \lambda/t_1(\lambda)$, where $t_1(\lambda)$ is the time needed for a dislocation to move a core size distance $\sim \lambda$. During this move, the two edges just above and below the dislocation core merge and are extinguished. After this extinction, the dislocation in Fig. 2 moves distance $\sim \lambda$. The time $t_1(\lambda)$ taken for this process to occur is related to λ via $\lambda \sim (t_1)^{1/3}$, as one can infer by considering the edge extinction event with the reasoning that led us to Eq. (3.6). Thus $t_1 \sim \lambda^3$, and $\mathrm{v_d} = \lambda/t_1 \sim 1/\lambda^2$, as stated in Eq. (3.21). See also § 4.3 for an alternative derivation of the dislocation velocity law (3.21).

4. Epitaxial Growth and Erosion on (110) Crystal Surfaces: Far-From-Equilibrium Phase Transitions Between Various Interfacial States

The far-from-equilibrium interfacial structures formed in the epitaxial growth and erosion (by molecular beams) on *rectangular* symmetry (110) crystal surfaces have only recently attracted attention [30–36]. Rather than pyramids, nearly periodic rippled one-dimensional structures are commonly seen on these surfaces — e.g. for Fe(110) [32], Ag(110) [30,31], Cu(110) and Rh(110) [33,35]. There are two types of these rippled states, with wave-vectors oriented along the two perpendicular principal axes of the (110) surfaces — i.e. the x_1 and x_2 axes mentioned in § 2. By changing the growth or erosion conditions such as substrate temperature, erosion flux intensity and energy, it is experimentally possible to drive a transition between the ripples

https://doi.org/10.4208/eajam.040411.030611a Published online by Cambridge University Press

oriented along the x_1-axis and those oriented along the x_2-axis. In addition to the rippled states, intriguing *intermediate* interface states have been revealed in these so-called 90° ripple rotation transitions between the two types of rippled states on Ag (110) surfaces [30,31], and more recently on Cu(110) and Rh(110) surfaces [33,35]. These intermediate states are believed to have a pyramidal character. Exotic pyramidal structures have also been seen on Al(110), in the form of self-assembled "huts" — i.e. roof-like pyramids [34].

In our studies [25–28], we discussed the far-from-equilibrium phenomena occurring in multilayer epitaxial growth and ion beam erosion on (110) crystal surfaces. Within a unified phenomenological model described here in § 2, we managed to expose a generic multitude of novel interfacial states on (110) surfaces, and also the far-from-equilibrium phase transitions between these states. On taking into account the various contributions to the surface current for (110) surfaces considered in § 2, we take the interface equation of motion Eq. (2.1) in the form

$$\begin{aligned}\frac{\partial h}{\partial t} =& -\frac{\partial}{\partial x_1}\left\{\frac{\partial h}{\partial x_1}\left[r_1 - u_{11}\left(\frac{\partial h}{\partial x_1}\right)^2 - u_{12}\left(\frac{\partial h}{\partial x_2}\right)^2\right]\right\} \\ & -\frac{\partial}{\partial x_2}\left\{\frac{\partial h}{\partial x_2}\left[r_2 - u_{22}\left(\frac{\partial h}{\partial x_2}\right)^2 - u_{21}\left(\frac{\partial h}{\partial x_1}\right)^2\right]\right\} \\ & -\kappa_{11}\left(\frac{\partial}{\partial x_1}\right)^4 h - 2\kappa_{12}\left(\frac{\partial}{\partial x_1}\right)^2\left(\frac{\partial}{\partial x_2}\right)^2 h - \kappa_{22}\left(\frac{\partial}{\partial x_2}\right)^4 h \\ & -\frac{\lambda_{11}}{2}\left(\frac{\partial}{\partial x_1}\right)^2\left(\frac{\partial h}{\partial x_1}\right)^2 - \frac{\lambda_{12}}{2}\left(\frac{\partial}{\partial x_1}\right)^2\left(\frac{\partial h}{\partial x_2}\right)^2 - \frac{\lambda_{21}}{2}\left(\frac{\partial}{\partial x_2}\right)^2\left(\frac{\partial h}{\partial x_1}\right)^2 \\ & -\frac{\lambda_{22}}{2}\left(\frac{\partial}{\partial x_2}\right)^2\left(\frac{\partial h}{\partial x_2}\right)^2 - \frac{\lambda_3}{2}\frac{\partial}{\partial x_1}\frac{\partial}{\partial x_2}\left[\frac{\partial h}{\partial x_1}\frac{\partial h}{\partial x_2}\right] . \end{aligned} \tag{4.1}$$

This interface evolution equation was solved numerically by a standard Euler algorithm, on adopting finite difference approximations for the spatial derivatives that preserve volume conservation. We employed the standard initial condition (at $t = 0$)

$$h(x_1, x_2, t) = 0 + \text{small random number different at each grid site } (x_1, x_2) ,$$

corresponding to a nearly horizontal interface close to the $h = 0$ interface, in a configuration that is unstable due to the ESV effect discussed in the Introduction. The eventual interface morphologies depend on the values of the model parameters in Eq. (4.1).

Through our analytic arguments and numerical simulations [25–28], Eq. (4.1) has been employed to derive the generic non-equilibrium phase diagram for (110) surfaces — cf. Figs. 7–9. The model successfully reproduces the experimentally observed transitions [30, 31, 33, 35], and the intermediate states between the two types of Rippled states discussed above — cf. § 4.1 and § 4.2. It predicts a number of intermediate interface states, intervening via consecutive transitions in the 90-degrees ripple rotation

https://doi.org/10.4208/eajam.040411.030611a Published online by Cambridge University Press

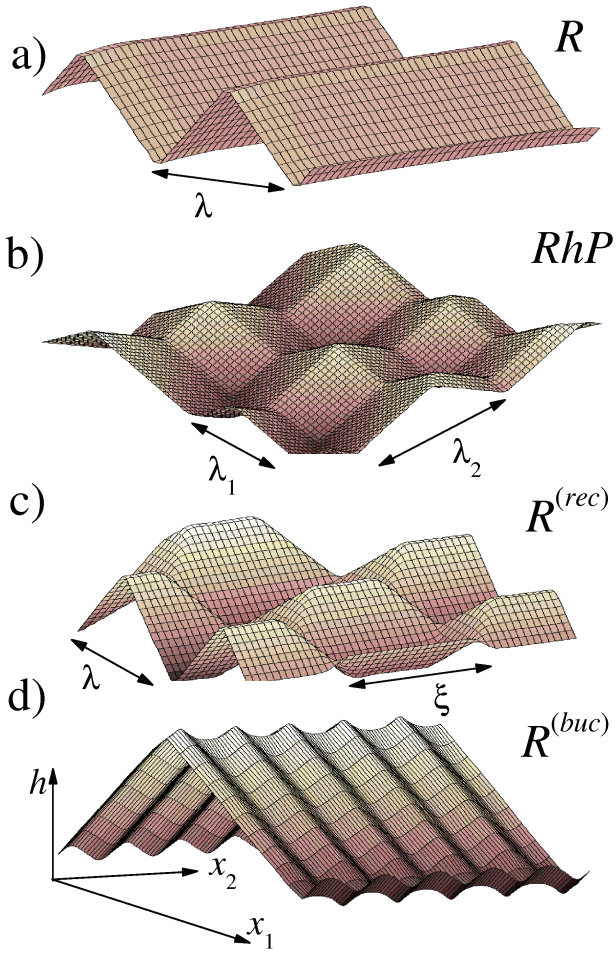

Figure 7: 3-D views of the interfacial morphologies in the epitaxial growth and erosion of (110) surfaces from simulations: (a) Ordinary Rippled R state with period λ; (b) Rhomboidal Pyramid RhP state with periods λ_1 and λ_2; (c) Rectangular Rippled $R^{(\mathrm{rec})}$ state, with motif a roof-like pyramid (hut) with a long roof-top edge of length ξ; and (d) Buckled Rippled $R^{(\mathrm{buc})}$ state.

transition between the two Rippled states — cf. Fig. 7. One of these is the Rhomboidal Pyramid State shown in Fig. 7(b) that we theoretically predicted [25], which was subsequently seen by de Mongeot and coworkers in the epitaxial erosion of Cu(110) and Rh(110) surfaces [33, 35].

In addition, our model yields a number of experimentally interesting intermediate states, with structural properties somewhere between those of rippled and pyramidal states. Among them are the Rectangular Rippled states of long roof-like objects (huts), shown in Fig. 7(c). Theoretically discussed in [25–27], these states have been seen in the epitaxial growth on Ag(110) [30, 31] and Al(110) [34]. Further, the basic Rect-

https://doi.org/10.4208/eajam.040411.030611a Published online by Cambridge University Press

angular Rippled structure we found, with the checkerboard arrangements of huts and pits (inverted huts) shown in Fig. 9 below, has been seen in ion erosion experiments on Ag(110) in Ref. [31] — cf. Fig. 4(d) there, and § 4.2 here for further discussions of these experiments. We predicted two types of Rectangular Rippled states, with wave-vectors oriented along the two perpendicular principal axes of the (110) surfaces; and to elucidate the transition between these states, we generalized the classical Gibbs phase coexistence rule to situations involving far-from-equilibrium phase transitions in the *absence* of an effective free energy governing dynamics, since in realistic growth dynamics it typically does not govern the interface dynamics — cf. § 2. Our theory [25,26] has also revealed the exotic Buckled Rippled interface state shown in Fig. 7(d). Unlike the usual interfacial states (e.g. see [18, 19, 41] and references there), the interfaces in the Buckled Rippled state exhibit non-vanishing, persistent surface currents forming a periodic convection-like vortex pattern — cf. § 4.1. This interface state is a far-from-equilibrium relative of Rayleigh-Benard and other self-organized convective flow patterns occurring in hydrodynamic systems [42]. We used our model to discuss the dynamics of the coarsening process in various interfacial states on (110) surfaces, where in particular the coarsening (growth of the spatial period) of the rippled states was shown to be mediated by ensembles of climbing dislocations that destroy the perfect periodicity of these states — cf. § 4.1 and § 4.3. Within our model, the interfacial phenomena underlying the enhanced coarsening of the Rhomboidal Pyramid state observed experimentally [33, 35] can be also elucidated — cf. § 4.1.

4.1. The multitude of interface states on (110) surfaces

As it stands, the model (4.1) depends on numerous parameters. However, the most important turn out to be the six parameters emerging from the non-equilibrium current (2.6). Moreover, under a simple anisotropic rescaling of the coordinates (x_1, x_2), the continuum model Eq. (4.1) can be made to depend on only three dimensionless parameters — cf. Ref. [26] and Eqs. f(2.15) and (2.16) there. These three parameters are

$$a = \frac{r_1/\sqrt{u_{22}} - r_2/\sqrt{u_{22}}}{r_1/\sqrt{u_{11}} + r_2/\sqrt{u_{22}}} , \qquad b = \frac{u_{12} + u_{21}}{2\sqrt{u_{11}u_{22}}} , \qquad c = \frac{u_{12} - u_{21}}{2\sqrt{u_{11}u_{22}}} . \tag{4.2}$$

Comparison of the theory [25–28] with experimental phenomenology [30, 31, 33, 35] shows that the parameter a is the most sensitive to the changes causing the 90° ripple rotation transition between the two rippled states — e.g. changes of deposition (or erosion) beam flux, beam energy and substrate temperature. The other parameters b and c in Eq. (4.2) are less sensitive to these changes — i.e. they vary little across the transition. Indeed, they depend on the u_{ij} but not on the r_i constants in the non-equilibrium surface current given by Eq. (2.6); and appear to mainly depend upon the material used in the experiments exhibiting the transition between the rippled states R_1 and R_2. The wave-vectors of these one-dimensionally periodic states are oriented along the x_1 and x_2 axes, respectively.

https://doi.org/10.4208/eajam.040411.030611a Published online by Cambridge University Press

The kinetic phase diagram of (110) surfaces obtained from our model (4.1) is depicted in Figs. 8 and 9, for the case of zero VA (nonzero vertical asymetry effects are discussed in § 4.2). The phase diagram is marked by two characteristic values of the control parameter a — viz.

$$a_+(b,c) = \frac{1-b+c}{1+b-c} \qquad \text{and} \qquad a_-(b,c) = -\frac{1-b-c}{1+b+c}\,. \tag{4.3}$$

Most of the phase diagram in Fig. 9 below is occupied by the simple rippled states R_1 and R_2 — cf. Fig. 7(a). The R_1 state, which is periodic along the x_1 direction, occurs for $a > \max[a_+(b,c), a_-(b,c)]$ in the phase diagram. This state consists of alternating R_1 facets with slope vectors $(+M_1, M_2 = 0)$ and $(-M_1, M_2 = 0)$. The R_2 state, which is periodic along the x_2 direction, occurs for $a < \min[a_+(b,c), a_-(b,c)]$. This state consists of alternating R_2 facets with the slope vectors $(M_1 = 0, +M_2)$ and $(M_1 = 0, -M_2)$. For a fixed value of c, in Figs. 8 and 9 the lines $a_+(b,c)$ and $a_-(b,c)$ in the (b,a) plane intersect at the point X where $b_X = \sqrt{1+c^2}$ and $a_X = (\sqrt{1+c^2}-1)/c$. This point X separates the following two characteristic phase behaviors encountered in the model.

Type A behavior: For $b < b_X = \sqrt{1+c^2}$ [or $u_{11}u_{22} > u_{12}u_{21}$, from Eq. (4.2)] one has $a_-(b,c) < a_+(b,c)$; and in the parameter range

$$a_-(b,c) < a < a_+(b,c)\,, \tag{4.4}$$

the R_1 and R_2 rippled phases are both unstable and have two types of qualitatively different intervening interface structures as follows.
(i) In the range Eq. (4.4), for $b < 1$ the Rhomboidal Pyramid (RhP) state develops [25, 26]. This state is a nearly periodic structure, consisting of four-sided pyramids with rhomboidally shaped contour lines as shown in Figs. 7(b) and 9, with profile of form

$$h(x_1,x_2) = |M_1|\,|x_1| + |M_2|\,|x_2|\ , \tag{4.5}$$

within a single period $|x_1| < \lambda_1/2$, $|x_2| < \lambda_2/2$. The rhomboidal angle 2θ between two of the selected quartet of facet slope vectors (viz. $\pm M_1, \pm M_2$) in Figs. 8 and 9) is given by $\tan\theta = M_2/M_1$. From our model, we find

$$\tan\theta = \frac{M_2}{M_1} \sim \sqrt{\frac{a_+ - a}{a - a_-}} \tag{4.6}$$

so $\theta \to 0$ and $M_2 \to 0$ as $a \to a_+$. As shown in Fig. 8, in this limit the RhP state continuously approaches the rippled state R_1 with facets selected from the doublet of the form $(\pm M_1, M_2 = 0)$, and the R_1-to-RhP transition in Figs. 8 and 9 is a Hopf bifurcation. On the other hand, in the limit where $\theta \to 90^\circ$ and $M_1 \to 0$ as $a \to a_-$ the RhP state approaches the R_2 rippled state with facets selected from the doublet of form $(M_1 = 0, \pm M_2)$ as shown in Fig. 8, and the R_2-to-RhP transition in Figs. 8 and 9 is also a Hopf bifurcation.

https://doi.org/10.4208/eajam.040411.030611a Published online by Cambridge University Press

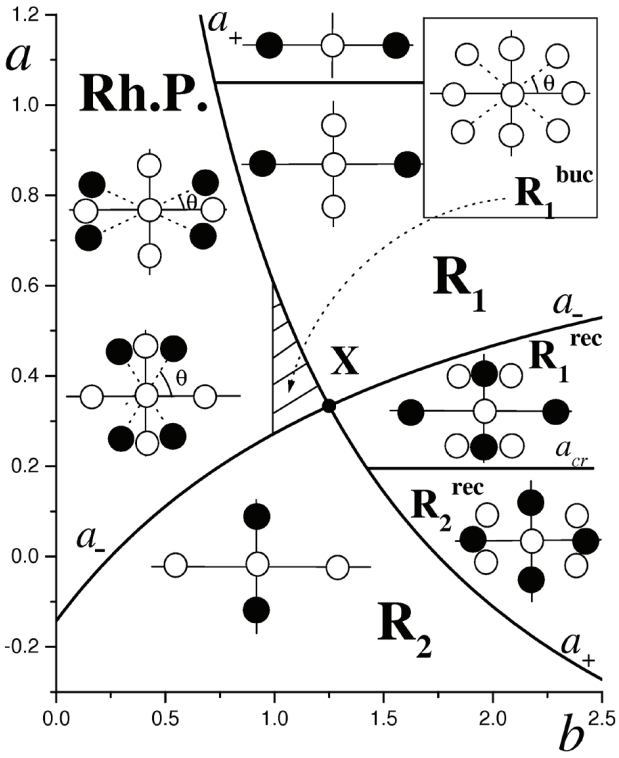

Figure 8: Kinetic phase diagram for multilayer epitaxial growth and erosion on (110) surfaces, obtained from analytic arguments [26]. For each interfacial state, the figure indicates the M-space with stable (full circles) and unstable (empty circles) zeros of the $\mathbf{J}^{\rm NE}(\mathbf{M})$. R_1 and R_2 are the two rippled states, RhP is the Rhomboidal Pyramid state, $R_1^{(\rm rec)}$ and $R_2^{(\rm rec)}$ are the two Rectangular Rippled states, whereas the Buckled Rippled state $R_1^{(\rm buc)}$ occupies the hatched domain (*all* of its current zeros are unstable, as depicted in the inset). For the RhP quartet, the angle θ ranges from zero at the transition to R_1 to 90° at the transition to R_2. (This figure is reproduced from Ref. [26].)

(ii) For $1 < b < b_X$ and a in the range Eq. (4.4), the so-called Buckled Rippled State (R^{buc}) develops — cf. Fig. 7(d). An unusual feature of this state is that its facets carry nonzero surface currents [25, 26], as discussed later in this section. For this state domain to exist, it is necessary that $b_X = \sqrt{1+c^2} > 1$ — i.e. that $c \neq 0$, equivalent to the condition $u_{12} \neq u_{21}$ from Eq. (4.2). We recall that this condition is equivalent to no effective free energy governing the interfacial dynamics — cf. § 2. Thus the peculiar Buckled Rippled State actually owes its existence to the non-existence of effective free energy! Furthermore, the condition $u_{12} \neq u_{21}$ should generally be satisfied on (110) surfaces. Indeed, from the discussion in § 2 the diagonal symmetry of the (001) surfaces (that have square symmetry), which would render u_{12} equal to u_{21}, is *not* a symmetry of the (110) surfaces (that have rectangular symmetry). Consequently, the existence of the Buckled Rippled State domain is a generic feature of the kinetic phase diagram of (110) crystal surfaces.

https://doi.org/10.4208/eajam.040411.030611a Published online by Cambridge University Press

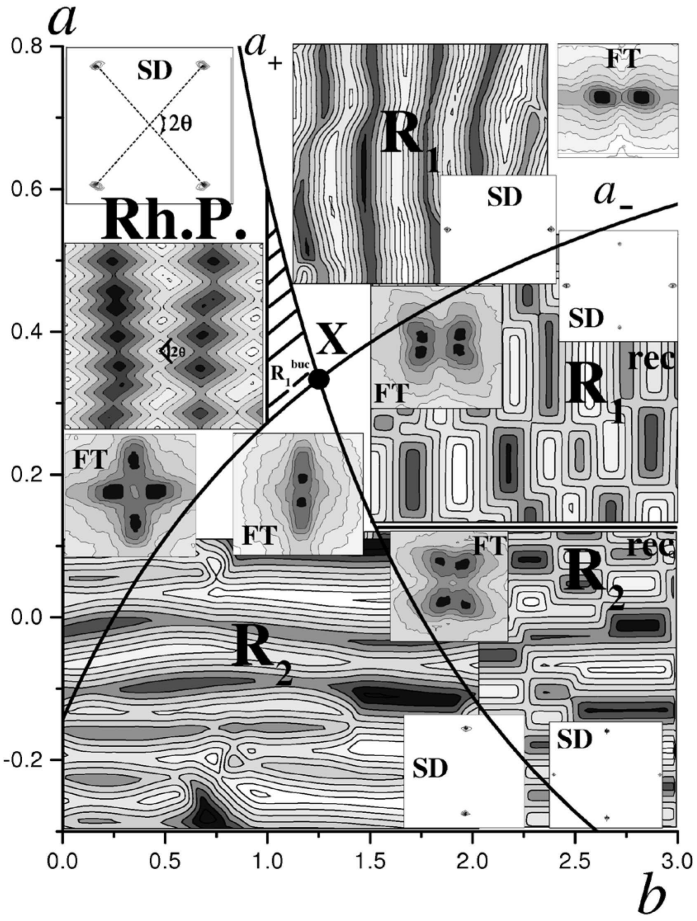

Figure 9: Kinetic phase diagram depicting various interfacial states, in terms of their basic properties (as obtained from the simulations): surface contour plots, magnitudes of interfacial height Fourier transforms (FT) corresponding to nearly in-phase diffraction patterns, and slope distributions (SD) in the M-space corresponding to out-of-phase diffraction patterns. R_1 and R_2 are the two rippled states, RhP is the Rhomboidal Pyramid state, $R_1^{(\mathrm{rec})}$ and $R_2^{(\mathrm{rec})}$ are the two Rectangular Rippled states, and $R_1^{(\mathrm{buc})}$ (hatched domain) is the Buckled Rippled state (its data are shown in Figs. 14 and 17). The RhP rhomboidal angle 2θ ranges from zero at the transition to R_1 to 180° at the transition to R_2. At long times, the four-lobe FTs of the $R^{(\mathrm{rec})}$ states approach the two-lobe form of the FTs of ordinary Rippled states [see Fig. 13(a)]. The peaks of SD of various states here directly correspond to the stable zeros of $\mathbf{J}^{\mathrm{NE}}(\mathbf{M})$ in Fig. 8, with the exception of the $R_1^{(\mathrm{buc})}$ state [cf. Figs. 14 and 17]. The phase diagram here is given for a positive value of the parameter c, without lack of generality — changing the signs of both a and c is equivalent to exchanging the base plane coordinates x_1 and x_2. Thus in particular, the $R_1^{(\mathrm{buc})}$ state [buckled form of the R_1 rippled state] occurs for $c > 0$, whereas the $R_2^{(\mathrm{buc})}$ state [buckled form of the R_2 rippled state, not shown here] occurs for $c < 0$. (This figure is reproduced from Ref. [26].)

Type B behavior: For $b > b_X = \sqrt{1+c^2}$ [or $u_{11}u_{22} < u_{12}u_{21}$ from Eq. (4.2)], one has

https://doi.org/10.4208/eajam.040411.030611a Published online by Cambridge University Press

$a_-(b,c) > a_+(b,c)$; and in the parameter range

$$a_+(b,c) < a < a_-(b,c) \tag{4.7}$$

the R_1 and R_2 facets are both stable. This multi-stability gives rise to the development of the so-called Rectangular Rippled States $R_1^{(\mathrm{rec})}$ and $R_2^{(\mathrm{rec})}$ [25, 26]. Indeed, from the simulations we find that interesting interface structures formed from both R_1 and R_2 facets develop in this range. These structures have rectangular contour lines (cf. Fig. 9), corresponding to roof-like pyramids (huts) with long roof-top edges, shown in Fig. 7(c). As shown in Fig. 9, for zero VA there are two kinds of such structures, called the Rectangular Rippled States $R_1^{(\mathrm{rec})}$ and $R_2^{(\mathrm{rec})}$. In the $R_1^{(\mathrm{rec})}$ state, the R_1 facets grow faster than the R_2 facets, whereas in the $R_2^{(\mathrm{rec})}$ state the R_2 facets grow faster than the R_1 facets. The difference in growth rates between the facets is related to R_1 facets and R_2 facets not being equivalent (symmetry related) to each other. Recall that the diagonal reflection $(x_1, x_2) \to (x_2, x_1)$, which would make R_2 equivalent to R_1, is not a symmetry of (110) surfaces — cf. § 2. This suggests that *in general* there is no steady state interface profile $(\partial h/\partial t = 0)$ from the dynamics equation (4.1) with the form of a *static* edge between the non-equivalent R_1 and R_2 facets — thus one of them prevails, as seen in the $R^{(\mathrm{rec})}$ states. Indeed, such a static edge can exist only along the special line $a_{cr}(b,c)$ in the phase diagram in Fig. 8, where

$$a_{cr} = \frac{\sqrt{1+(c/3)^2}-1}{c/3} \tag{4.8}$$

for zero VA [26] (nonzero vertical asymmetry is discussed in § 4.2). A static coexistence between the R_1 and R_2 facets can be realized only at the phase transition line between the Rectangular Rippled States $R_1^{(\mathrm{rec})}$ and $R_2^{(\mathrm{rec})}$ defined by Eq. (4.8) — cf. Figs. 8 and 9. This phase transition line has also been derived in the spirit of Gibbs' original phase coexistence argument by requiring a static coexistence between the two facet types [26], but here the analytic result (4.8) is obtained for non-standard situations where there is *no* effective free energy. This result for the phase transition line is corroborated by simulations [25, 26], which confirm the correctness of this generalization beyond our original Gibbs argument in the present context where no effective free energy is involved.

The type A behavior occurring in materials with $u_{11}u_{22} > u_{12}u_{21}$, which involves the formation of the Rhomboidal Pyramid state intervening between the two rippled states, was theoretically predicted [25] and subsequently observed in epitaxial erosion experiments on Rh(110) and Cu(110) surfaces [33]. On the other hand, the type B behavior occurring in materials with $u_{11}u_{22} < u_{12}u_{21}$, with the ripple rotation transition proceeding through a multi-stable parameter range where Rectangular Rippled states are formed [25–27], was observed in experiments on the Ag(110) surface involving both epitaxial growth [30] and ion beam erosion [31]. It is significant that erosion by molecular beams can be envisioned as a deposition of vacancies, as the same model can

https://doi.org/10.4208/eajam.040411.030611a Published online by Cambridge University Press

be used to discuss both epitaxial growth and erosion phenomena. We now discuss properties of the many interfacial states identified, stressing their experimental significance.

Particularly interesting are theoretical predictions for the behavior of two major kinds of surface diffraction data — viz. (i) out-of-phase diffraction data, corresponding to the interface slope ($\mathbf{M} = \boldsymbol{\nabla} h$) SD distribution; and (ii), nearly in-phase diffraction data, corresponding to the magnitude of the square of the interface height $h(\mathbf{x}, t)$ Fourier transform (FT). Especially significant is the Rhomboidal Pyramid (RhP) state, a two-dimensionally periodic interface structure of four-sided pyramid-like objects shown in Fig. 7(b), obtained using Eq. (3.6). The contour lines (step terraces) of these pyramids are rhombi, which sometimes deform into rhomboids if roof-top edges develop on the pyramids — cf. Fig. 10. The predicted RhP state [25] has since been seen by de Mongeot and co-workers, in erosion by molecular beams on both Cu(110) and Rh(110) surfaces [33]. The RhP state has the interface SD (i.e. an out-of-phase diffraction pattern), with a quartet of four equivalent peaks $(\pm M_1, \pm M_2)$ — cf. Figs. 8, 9 and 11. The RhP motif in Eq. (4.5) implies that the 2D FT of the RhP has dominant peaks along the q_1 and q_2 axes, with (i) the set of peaks at wave-vectors $(\pm 2\pi(2n+1)/\lambda_1, 0)$; and (ii), the set of peaks at $(\pm 2\pi(2n+1)/\lambda_2, 0)$. Structurally, from Eq. (4.5) the RhP state is a linear superposition of the two rippled states. Thus its FT (the nearly in-phase diffraction pattern) is simply the superposition of the FTs of the two rippled states R_1 and R_2 — cf. Fig. 9. From simulations, at most the four brightest ($n = 0$) peaks occurring at the wave-vectors $(\pm 2\pi/\lambda_1, 0)$ and $(\pm 2\pi/\lambda_2, 0)$ are visible — cf. Fig. 10]. Such a four-lobe nearly in-phase diffraction pattern is manifest in the simulations, as shown in the FT magnitude plots of RhP in Figs. 9 and 10(a). All other FT peaks are smeared out by the positional disorder of the pyramid lattice, which is especially pronounced in the RhP region close to the $R_1^{(\mathrm{buc})}$ state in the phase diagram shown in Fig. 9. The RhP in-phase diffraction pattern there exhibits only two peaks, except very close to the RhP-to-R_2 transition — cf. Figs. 10(b) and 11(b), and our further discussion below. Such an almost two-lobe RhP near the in-phase diffraction pattern has indeed been seen, in a recent study where the RhP state occurred in erosion on Cu(110) and Rh(110) crystal surfaces [35].

The RhP state has a nearly rectangular network of pyramid facet edges — cf. Fig. 10. The interface structure and coarsening dynamics of the RhP state is similar to that of the four-sided square pyramid Phase I (with the square network of edges) on (001) surfaces [18, 29] — cf. Figs. 2 and 5, and § 3.2 and § 5. Indeed, Phase I has the interface profile given by Eq. (4.5) with $M_1 = M_2$. Thus the RhP state, shown in Fig. 10 on the (110) surfaces in Fig. 9, is essentially a (rhomboidally) anisotropic version of the square pyramid Phase I on (001) surfaces in Fig. 2. Topologically, these two states are identical. The simulations show that the coarsening of the RhP state is mediated by the motion and annihilations of the dislocations (topological defects) of the network of pyramid facet edges seen in Fig. 10, in a way which is topologically identical to the coarsening of the square pyramid Phase I on (001) surfaces in Figs. 2

https://doi.org/10.4208/eajam.040411.030611a Published online by Cambridge University Press

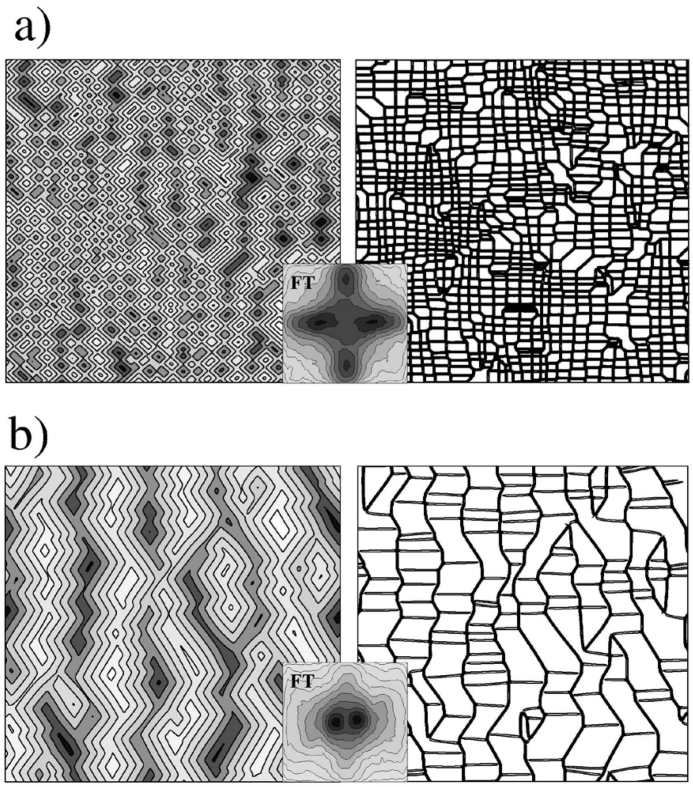

Figure 10: Rhomboidal Pyramid (RhP) state. To the left are the interface contour plots; and to the right, the facet edge plots (contour plots of the magnitude of local interface curvature) with prominent present dislocations destroying perfect periodicity of the interface profile. Fig. (a) shows the ordinary RhP state, occurring away from the RhP-to-$R_1^{(\mathrm{buc})}$ transition. Fig. (b) shows the intensely rough RhP state occurring close to this transition (the interface here corresponds to the maximally rough surface found at $a = 0.6$ in Fig. 11). Note the qualitative difference between the FTs in the upper and lower panels.

and 5 — cf. § 3.2. In accord with this, from the simulations we find that the interface width $w =< h^2 >^{1/2}$ grows as $w \sim t^{\beta}$ with $\beta \approx 1/4$, which is the same as for the four-sided pyramid state on (001) surface discussed in § 3.2. However, we stress that such coarsening was found in the RhP domain *away* from the transitions to other interface states in the phase diagram of Figs. 8 and 9, hence the RhP forms as in Fig. 10(a). However, a substantially faster coarsening was found in the RhP region close to the $R^{(\mathrm{buc})}$ state — i.e. in the proximity of the hatched domain in Figs. 8 and 9. This *enhanced roughening* of RhP is documented in Fig. 11(a), which gives the interface width w for several different times versus the parameter a, for a fixed $b < 1$ close to the transition to $R^{(\mathrm{buc})}$ at $b = 1$ in Fig. 9. In Fig. 11(a), the RhP state is between a_+ and a_-, whereas for $a < a_-$ and $a > a_+$ the rippled states are R_2 and R_1, respectively. The fastest coarsening was found within the RhP state range $a_- < a < a_+$, when the RhP pyramids eventually grow with a high coarsening exponent $\beta \approx 0.4$ — cf. Fig. 11(a).

https://doi.org/10.4208/eajam.040411.030611a Published online by Cambridge University Press

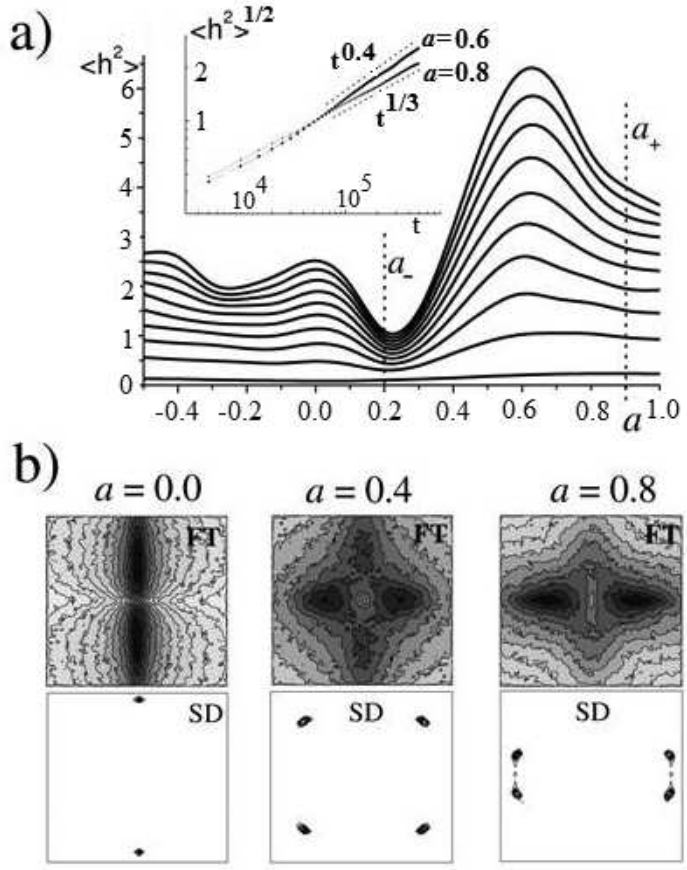

Figure 11: Fig. (a) shows the square of the interfacial width $< h^2 >$ versus the parameter a for several different times — across the transition from the rippled state R_2 (for $a < a_-$) to the rippled state R_1 (for $a > a_+$), going through the intermediate Rhomboidal Pyramid state (occurring for $a_- < a < a_+$). The figure is obtained from numerous simulations done along the line $b = 0.8$, passing close to the transition line $b = 1$ from the RhP to the $R_1^{(\mathrm{buc})}$ state — cf. Figs. 8 and 9. The inset documents the enhanced roughening of the RhP state at $a = 0.6$, with the roughening exponent reaching the value ≈ 0.4 close to the center of the RhP range. In Fig. (b), to the right are FT magnitudes and SDs found along this ripple rotation transition for $a = 0$ (in the R_2 state), and for $a = 0.4$ and 0.8 (both within the intensely rough RhP range). Note the FTs, the in-phase diffraction patterns of the intensely rough RhP, have just one pair of peaks as in the R_1 state pattern. The other significantly weaker pair of peaks can only be seen close to the transition to R_2 ($a = 0.4$ here). Note the SDs (i.e. the out-of-phase diffraction patterns) distinguish the RhP from the R_1 state — cf. Fig. 9.

Such an enhanced roughening of the RhP intermediate state, faster than that of the nearby rippled states (see below), has also been observed in experiments on Cu(110) and Rh(110) surfaces [33,35]. We stress that the enhanced roughening of RhP occurs only in proximity to the $R^{(\mathrm{buc})}$ state in Figs. 8 and 9. There the RhP state becomes highly anisotropic, as seen in Fig. 10(b); and we see that the two RhP state periods λ_1 and λ_2, along the principal axis of (110) surface in Fig. 7(b), significantly differ from each other. This anisotropy is also manifest in the character of the pyramid facet

https://doi.org/10.4208/eajam.040411.030611a Published online by Cambridge University Press

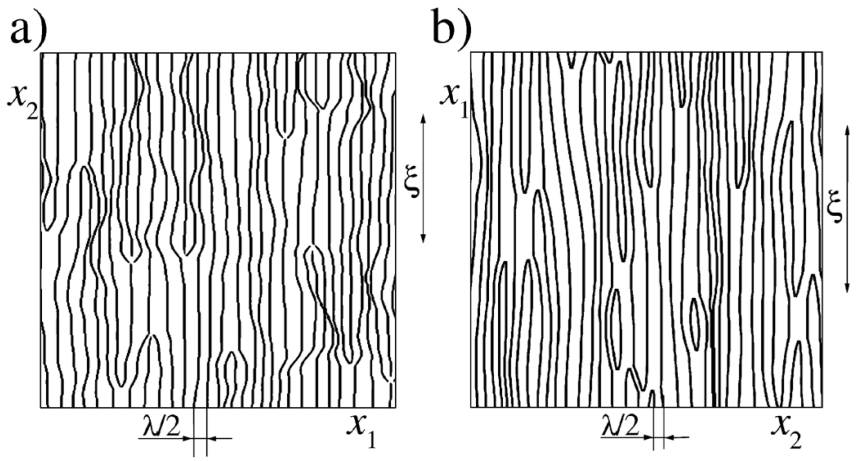

Figure 12: (a) Facet edge plot of the rippled state R_1 in the phase diagram domain, where both fork and knife dislocations are present. (b) Facet edge plot of the Rippled state R_2 in the domain where only knife dislocations occur. Note that the R_2 state in Fig. (b) is rotated by 90°, to facilitate comparison with Fig. (a). The length scale ξ is the average distance between dislocations along a ripple.

edges in Fig. 10(b), where vertical edges are sharp and connected to each other, either directly or by frequently present roof-top edges. In contrast, the horizontal edges in this figure are blunt and disconnected. Due to this positional disorder of the horizontal edges, the *intensely rough* RhP structure in Fig. 10(b) is significantly more disordered than the ordinary RhP structures in Fig. 10(a), and its enhanced roughening is similar to the fast roughening in the nearby $R^{(\mathrm{buc})}$ state discussed later in this section.

Both the intensely rough RhP and the $R^{(\mathrm{buc})}$ state exhibit two-lobe nearly in-phase diffraction patterns (i.e. FT's) as shown in Figs. 10 and 11, and also in Fig. 17 later. The two-lobe rather than four-lobe FT pattern is due to the typically large aspect ratio λ_1/λ_2 and the strong positional disorder of the vertical facet edges seen in Fig. 10(b) — cf. Ref. [26] for the discussion of this point. Thus the intensely rough RhP state has nearly the same in-phase diffraction pattern as a simple rippled state. This feature, found experimentally on Cu(110) and Rh(110) surfaces [33, 35], is documented here in Fig. 11 from the simulations. Note that this FT (i.e. the nearly in-phase diffraction pattern) is nearly the same as that of the R_1 rippled state, except close to the R_2 rippled state transition — cf. Fig. 11(b, middle panel). Consequently, the out-of-phase diffraction pattern [i.e. the slope distribution in the simulations — cf. Fig. 11(b)] with the quartet of four equivalent peaks is essential to identify the RhP state, as confirmed by recent experiments on Cu(110) and Rh(110) surfaces [35]. Our R_1 state here corresponds to the "hot rippled state" (the high temperature one), whereas the experiments show that the RhP has the same FT as the "cold ripple state" [35] — cf. also further discussion at the end of this section.

Let us now consider the properties of the rippled states shown in Fig. 7(a). The sim-

https://doi.org/10.4208/eajam.040411.030611a Published online by Cambridge University Press

ulations show coarsening of these states mediated by moving dislocations that destroy the perfect periodicity of their structures as shown in Figs. 12(a) and (b), defining the interface in terms of the edges formed between alternating R facets. The dislocations of the rippled states R_1 and R_2 are geometrically similar to the dislocations of equilibrium 2D smectic A liquid crystals [43]. However, in the present generically non-equilibrium (driven) system, the dislocations are prominent dynamical objects that move (climb) along the directions of the facet edges — cf. Figs. 12(a) and (b). The dislocation motion is driven by the edge tensions, which are unbalanced at the dislocation cores. There are two morphologically different types of dislocations in Figs. 12(a) and (b) — viz. (i) "forks", with three edges on one side of the core and just one edge on the opposite side; and (ii) "knives", with two edges on one side and no edges on the opposite side of the core. Thus in both cases there are two extra edges pulling the dislocations, and the edge tension misbalance causes the dislocations to move along the ripples — i.e. vertically in Figs. 12(a) and (b). The dislocation motion is discussed analytically in Ref. [28] — cf. § 4.3 here. Importantly, we find this dislocation motion (climb) mediates the growth of the ripple phase period λ — i.e. as the dislocation climbs along the extra edges, it leaves behind enlarged facets [cf. the facet width just above and below dislocations in Figs. 12(a) and (b)]. Thus the growth of the rippled phase period λ is the fusion of the rippled state R facets mediated by climbing dislocations. In addition to the interface width w and average ripple period λ, the rippled states are characterized by the *coherence length* of the ripples ξ, corresponding to the separation between dislocations along a ripple (cf. Fig. 12).

The ripple coherence length ξ increases with time due to the annihilations of pairs of dislocations traveling towards each other, as shown in Figs. 12(a) and (b). Consequently, the number of dislocations decreases and the ripple coherence length ξ increases in time. Both λ and ξ are extracted from the simulations by computing the anisotropic height-height correlation function

$$K(x_1, x_2, t) =< h(x_1, x_2, t)h(0, 0, t) >= (w(t))^2 \psi (x_1/\lambda(t), x_2/\xi(t)) \tag{4.9}$$

for the R_1 phase, where the function ψ decays in an oscillatory fashion along x_1 (longitudinal correlations), and monotonously along x_2 (transverse correlations) — cf. Fig. 6(c) of Ref. [26] for details. By using the longitudinal and transverse correlations, from the simulations we find $\lambda \sim w$ and ξ grow as power laws in time t — viz.

$$\lambda \sim w \sim t^{n_\lambda}, \qquad \xi \sim t^{n_\xi} . \tag{4.10}$$

By extracting the values of the coarsening exponents $\beta = n_\lambda$ and n_ξ, it emerges that there are *two* kinetically different sub-domains of the whole rippled phase domain in the phase diagram in Fig. 9, which are characterized by the different morphologies and kinetics of the moving dislocations — cf. Figs. 12(a) and (b). Most of this phase diagram in Fig. 9 is occupied by the rippled phase with the dislocations seen in Fig. 12(a), where both forks and knives climb along the x_2 direction. In addition, the simulations

https://doi.org/10.4208/eajam.040411.030611a Published online by Cambridge University Press

reveal that dislocations also move along the x_1 direction. However, in contrast to the steady directional dislocation climb along the x_2 direction in Fig. 12(a), the dislocation glide motion along x_1 has a random walk character and involves reconnection (topological changes) of the edges network, turning forks into knives and vice versa — cf. Fig. 6(d) of Ref. [26]. In the sub-domain of the phase diagram where this reconnection mechanism is active, from the simulations we find that $w \sim \lambda$ and ξ grow as in Eq. (4.10) with $\beta = n_\lambda = 2/7$ and $n_\xi = 4/7$, which is further corroborated by analytic arguments [28] — cf. § 4.3 here. The simulations also reveal the existence of another sub-domain of the kinetic phase diagram in Fig. 9, where the coarsening of the rippled phase is enhanced and proceeds with different exponents $n_\lambda = 1/3$ and $n_\xi = 1/2$. This enhanced coarsening of the rippled state occurs for $c \neq 0$, and is found in the rippled state sub-domain below the intensely rough RhP domain as shown in Fig. 9 — e.g. for $a < a_-$, below the intensely rough RhP in Fig. 11. In this rippled state sub-domain, reconnections of the facet edges (i.e. the formation of forks out of knives) are suppressed, as shown in Fig. 12(b) from simulations where only knife-dislocations are present. This dynamical constraint yields the exponents $\beta = n_\lambda = 1/3$ and $n_\xi = 1/2$, found in the simulations and further corroborated by analytic arguments [28] — cf. § 4.3 and the discussion of Eq. (4.33) there. We note experimental evidence for rippled and RhP state coarsening, with effective exponents $\beta \approx 0.35 > n_\lambda \approx 0.1$ [35]. In contrast to the long time (slope selection dominated) regime with $\beta = n_\lambda$, in the experiments the selected facets do not fully reach the selected slope magnitudes as their slope still grows within the experimental time window [35]. Such early time regimes are theoretically known to exhibit the coarsening exponent $n < \beta$, with typically small n in the range $0.1 - 0.2$ [22].

The type A behavior, with the RhP and $R^{(\mathrm{buc})}$ states intervening in the transition between the rippled states, is only one of two possible routes between the rippled states in the phase diagram in Fig. 9. The other route is the type B behavior, where the transition between the rippled states R_1 to R_2 goes through the Rectangular Rippled states $R_1^{(\mathrm{rec})}$ and $R_2^{(\mathrm{rec})}$, comprised of roof-like pyramids (huts) formed out of both R_1 and R_2 facets — cf. Figs. 7(c), 9 and 13. The basic $R^{(\mathrm{rec})}$ state structure, with the checkerboard arrangement of huts and pits (inverted huts), has been seen in erosion experiments on Ag(110) by Costantini *et al.* — cf. Fig. 4(d) in Ref. [31], for comparison with our Figs. 9 and 13. The hut sizes λ and ξ were measured along the two (non-equivalent) principal directions of a (110) surface — cf. Figs. 7(c) and 13. From the simulations, we find these two length scales grow in time with *different* power laws — viz. $\lambda \sim t^{n_\lambda}$ with $n_\lambda = 1/4$ and $\xi \sim t^{n_\xi}$ with $n_\xi = 1/2$, as corroborated by analytic discussions in Ref. [28] and § 4.3 here. As $w(t) \sim \lambda(t) \ll \xi(t)$ at long times, the $R^{(\mathrm{rec})}$ pyramid states may be considered to be a special kind of rippled state with period $\lambda(t)$, as suggested by the $R^{(\mathrm{rec})}$ Fourier transforms — i.e. the nearly in-phase diffraction patterns obtained from the simulations shown in Fig. 13(a), with four peaks at $(\pm q_1, \pm q_2)$ where $q_1 \sim 1/\lambda$ and $q_2 \sim 1/\xi$ for the $R_1^{(\mathrm{rec})}$ state. However, as $\xi(t)/\lambda(t)$ diverges at long times, the FT of

https://doi.org/10.4208/eajam.040411.030611a Published online by Cambridge University Press

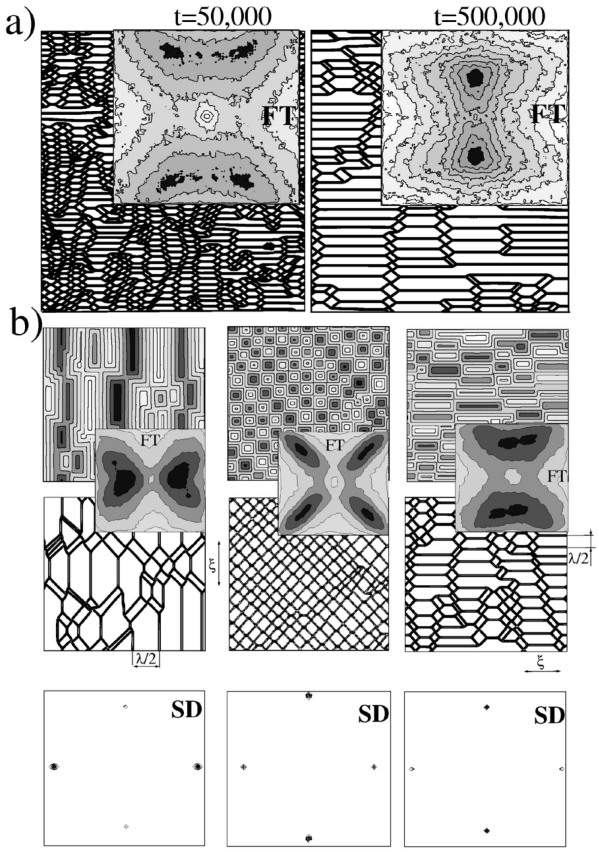

Figure 13: Rectangular Rippled States. (a) Snapshots of facet edge plots of the $R_2^{(\mathrm{rec})}$ state and interface FTs at two different times. Note the presence of rapidly growing horizontal roof-top edges interfacing the dominant R_2 facets [cf. also Fig. 7(c)]. These roof-like pyramids (huts) are terminated on both sides by small rhomboidally shaped R_1 facets, which cluster to form long chains. (b) Sequence of interfacial states occurring in the $R_1^{(\mathrm{rec})}$ to $R_2^{(\mathrm{rec})}$ transition (interface contour lines and corresponding facet edge plots). For $a > a_{cr}$, the $R_1^{(\mathrm{rec})}$ state with roof-top edges grows vertically (left panel). For $a < a_{cr}$, the $R_2^{(\mathrm{rec})}$ state with roof-top edges grows horizontally (right panel). At the critical point $a = a_{cr}$, four-sided rectangular pyramids develop, with no roof-top edges present (middle panel).

$R_1^{(\mathrm{rec})}$ approaches the form of the FT of the nearby rippled R_1 state, with just two peaks at $(\pm q_1, 0)$. The length scale $\xi(t)$ is essentially the length of the long roof-top edges on these roof-like pyramids — cf. Figs. 13 and 7(c). These roof-top edges develop and grow either along the x_2 direction in the $R_1^{(\mathrm{rec})}$ state, or along the x_1 direction in the $R_2^{(\mathrm{rec})}$ state — cf. Fig. 13(b). The snapshots from the simulations of the $R_2^{(\mathrm{rec})}$ state in Fig. 13(a) well document the presence of rapidly growing horizontal roof-top edges, interfacing the dominant R_2 facets. Note that the roof-like pyramids (huts) are terminated on both sides by small rhomboidally (diamond) shaped R_1 facets. A prominent feature of the $R^{(\mathrm{rec})}$ state is that these diamond-like facets cluster to form long chains — cf. Fig. 13. Due to their presence, the interface structure of the $R^{(\mathrm{rec})}$ states

https://doi.org/10.4208/eajam.040411.030611a Published online by Cambridge University Press

is more coherent than that of ordinary rippled states. Indeed, at early times the $R^{(\mathrm{rec})}$ states appear periodic-like, not only along the λ direction but also along the ξ direction (unlike the ordinary rippled phase). However, with increasing time the number of diamond facets clustered into each of the chains decreases, and the diamond facet chains are less evenly spaced — cf. Fig. 13(a). Consequently, the coherence of the $R^{(\mathrm{rec})}$ state along the transverse direction (parallel to ripples) decreases in time, and becomes comparable to that of the ordinary rippled state (with dislocations present). Further, at long times the four FT peaks of the $R^{(\mathrm{rec})}$ state shown in the left panel of Fig. 13(a) left panel broaden and eventually merge into just two peaks as shown in the right panel, and such an FT becomes indistinguishable from that of the ordinary Rippled state (cf. Fig. 9).

Let us now discuss the transition between the $R_1^{(\mathrm{rec})}$ and $R_2^{(\mathrm{rec})}$ states in Figs. 8 and 9, for the case of zero VA (vertical asymmetry); nonzero VA is discussed in § 4.2. Not only roof-top edges on the rectangular pyramids develop at the transition point between the $R_1^{(\mathrm{rec})}$ and $R_2^{(\mathrm{rec})}$, for precisely at the transition point there are simple four-sided pyramids without roof-top edges, with a rhomboidal network of edges — cf. Fig. 13. This critical state is an anisotropic version of the four-sided square pyramid Phase II on (100) surfaces [18, 29] — cf. § 5. Its nearly in-phase diffraction pattern has four peaks $(\pm q_1, \pm q_2)$, with $q_1 \sim q_2 \sim 1/t^{1/4}$. The $R_1^{(\mathrm{rec})}$-to-$R_2^{(\mathrm{rec})}$ transition line is a far-from-equilibrium first-order-like transition, at which the non-equivalent R_1 and R_2 facets of (110) surfaces coexist [cf. Eq. (4.8)], which is necessary to ensure the structural stability of the four-sided pyramids developing at the transition point as seen in Fig. 13(b, middle panel). Indeed, R_1 and R_2 facets comprising such pyramids can maintain (at long times) equal sizes and shapes only if the conditions are fulfilled to render the stationary solution $(\partial h/\partial t = 0)$ of Eq. (4.1) as the static interface (edge) between two *semi-infinite* R_1 and R_2 facets. As noted in § 4.1, this requirement yields our analytic prediction for the position of the $R_1^{(\mathrm{rec})}$-to-$R_2^{(\mathrm{rec})}$ transition line given in Eq. (4.8), which is corroborated by simulations — cf. Fig. 13(b). The main features of the ripple rotation transition seen on Ag(110) surface (epitaxial growth) [30] correspond to those of our $R_1^{(\mathrm{rec})}$-to-$R_2^{(\mathrm{rec})}$ transition. Importantly, in the multi-stable region suggested by the experiments of Ref. [30], it is *not* simple rippled phases (R_1 and R_2) but rather the more complex structures of the Rectangular Rippled states that appear. However, the intermediate state seen in Ref. [30] on Ag(110) has a nearly in-phase diffraction pattern (FT) that differs from the critical state seen in Fig. 13(b, middle), whereas the experimental out-of-phase pattern (SD) is the same as for the state in Fig. 13(b, middle). This puzzling behavior was elucidated in Ref. [27], where the experimental nearly in-phase diffraction pattern (as observed in [30] close to the ripple rotation transition) was shown to emerge due to the vertical growth asymmetry between the huts and pits (inverted huts) comprising the $R^{(\mathrm{rec})}$ state interfaces. We address these vertical growth asymmetry effects in § 4.2.

https://doi.org/10.4208/eajam.040411.030611a Published online by Cambridge University Press

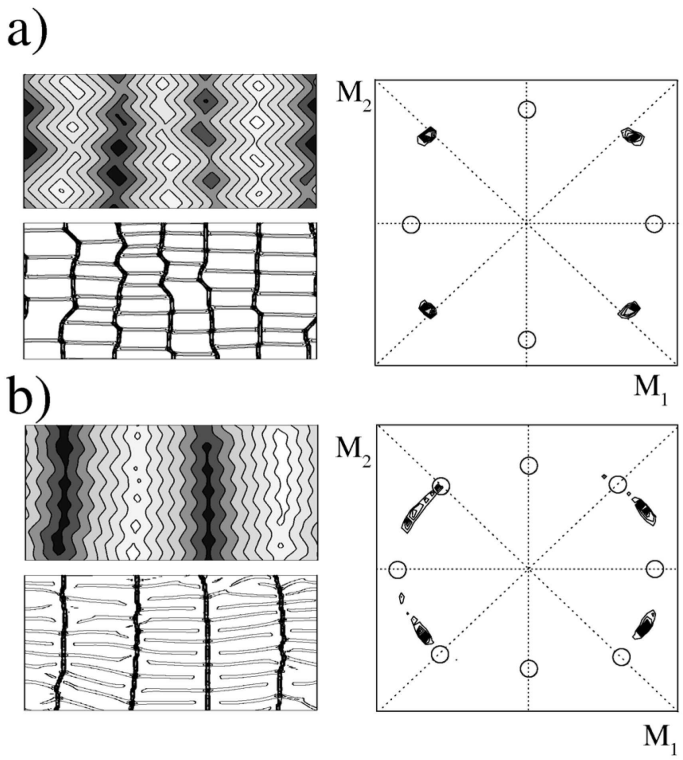

Figure 14: Rhomboidal Pyramid state [in (a)] and the Buckled Rippled state [in (b)] have similar interface morphologies — cf. their SDs in M-space, their interfacial contour plots, and corresponding facet edges plots. For both states, the quartet zeros of the surface non-equilibrium current are on the dashed lines "guiding eye". In Fig. (b), the Buckled Rippled state SD has peaks that are *off* the current zeros (indicated by open circles). Thus in contrast to the Rhomboidal Pyramid state in the left panel in Fig. (a), the facets of the Buckled Rippled state carry persistent surface currents — cf. also Fig. 15.

Last but not the least, let us consider the Buckled Rippled $R^{(\mathrm{buc})}$ state seen in Fig. 7(d), which occupies the hatched domain in the phase diagram in Figs. 8 and 9. In this region, as discussed in Refs. [25, 26], *all* zeros of $\mathbf{J}^{(NE)}(\mathbf{M})$ are *unstable*, in contrast to the rest of the phase diagram where at least some zeros are stable — cf. Fig. 8. The existence of this state defies the common belief that the stable facets with vanishing $\mathbf{J}^{(NE)}(\mathbf{M})$ dominate the epitaxial growth and erosion with slope selection, as no facet is stable here! In the region occupied by the $R^{(\mathrm{buc})}$ state in Figs. 8 and 9, we find a long transient involving ordering of pyramidal chains — cf. the simulation in Fig. 8(b) from Ref. [26]. The interface eventually selects the shape of a rippled phase with buckled (wavy) ripples as seen in Fig. 7(d). The buckling breaks the ripples into smaller facets joined by edges — cf. Fig. 14. Consequently, the $R^{(\mathrm{buc})}$ state is structurally close to the RhP state, with a motif similar to that of RhP from Eq. (4.5), but with M_1 and M_2 there *not* corresponding to a zero of $\mathbf{J}^{(NE)}(\mathbf{M})$ — cf. Fig. 14(b).

Thus strikingly, in contrast to the RhP and all other interfacial states discussed

https://doi.org/10.4208/eajam.040411.030611a Published online by Cambridge University Press

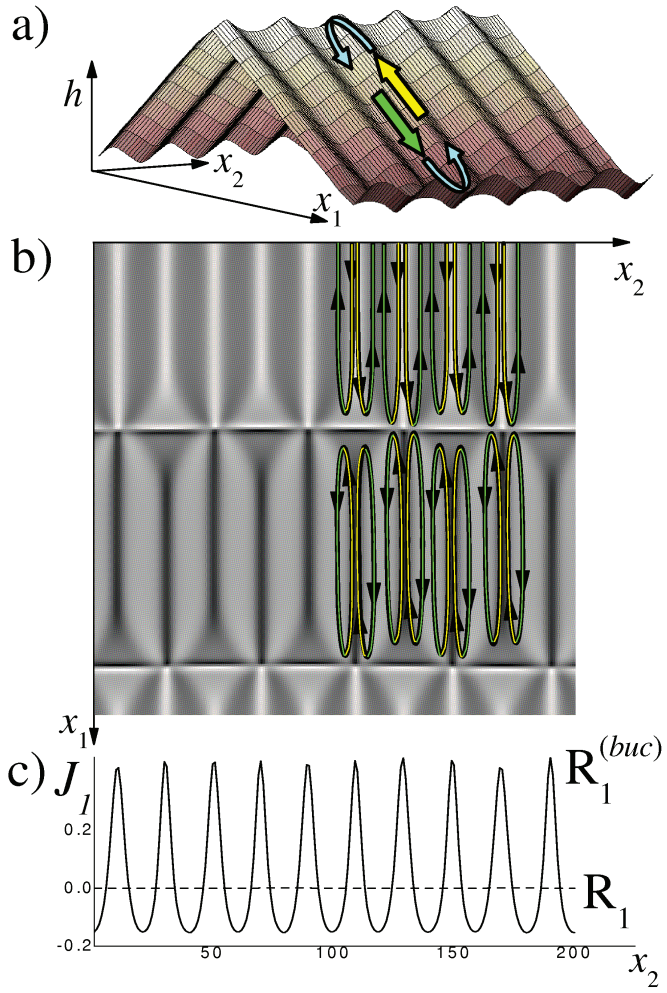

Figure 15: Persistent surface currents in the Buckled Rippled state, $R_1^{(\mathrm{buc})}$ in Fig. (a). In Fig. (c) the current J_1 is plotted versus x_2 for a fixed x_1, away from tops and bottoms of the buckled ripples of the $R_1^{(\mathrm{buc})}$ state. The persistent current is down-hill along the $R^{(\mathrm{buc})}$ facets and it is up-hill along the edges between the facets. This yields a vortex-like behavior of the surface current, which goes up the edges and circles back down along the facets. The overall surface current pattern has the character of a vortex lattice as depicted in Fig. (b), where the currents are indicated atop of the corresponding contour plot of J_1 (x_1, x_2). For comparison, in Fig. (c) we also plot (by the dashed line) the surface current J_1 for the ordinary rippled phase which approaches zero at long times when the facets become large. (This figure is reproduced from Ref. [26].)

here, the $R^{(\mathrm{buc})}$ state does not develop facets with slopes where $\mathbf{J}^{(NE)}(\mathbf{M})$ vanishes — cf. Figs. 14(b) and 15. Rather, as shown in Fig. 15, the facets of the $R^{(\mathrm{buc})}$ state carry non-vanishing *persistent* downhill surface currents. The downhill currents in the $R^{(\mathrm{buc})}$ facets are compensated for by uphill currents flowing along the edges between the facets — i.e. the net current flux is *zero* in Fig. 15(c). Due to these current back-flows, the overall surface current pattern has a *vortex-like* character, with vortices forming a

https://doi.org/10.4208/eajam.040411.030611a Published online by Cambridge University Press

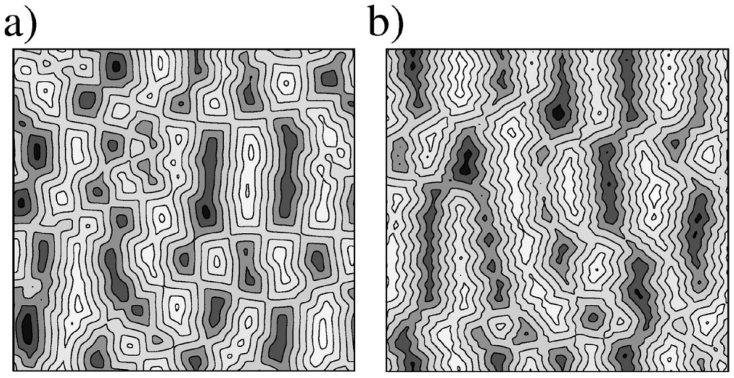

Figure 16: (a) Interface contour plot at the X point (cf. Figs. 8 and 9), exhibiting large huts and pits arranged as in the $R_1^{(\mathrm{rec})}$ state, just to the right of the X point in Figs. 8 and 9. The interface contour plot obtained in the $R_1^{(\mathrm{buc})}$ state, exhibiting large *buckled* huts and pits arranged as at the X point, which terminates the $R_1^{(\mathrm{buc})}$ range on its right-hand side — cf. Figs. 8 and 9. The $R_1^{(\mathrm{buc})}$ state is essentially the buckled form of the $R_1^{(\mathrm{rec})}$ state.

rectangular lattice — cf. Fig. 15(b). Note that the $R^{(\mathrm{buc})}$ state exhibits both clockwise and anti-clockwise oriented vortices alternating across the surface. This *convection-like* surface current pattern driven by incoming atomic fluxes is a far-from-equilibrium relative of the self-organized fluid patterns in convective hydrodynamic instabilities driven by heat-fluxes — e.g. Rayleigh-Benard patterns [42]. Unlike such steady hydrodynamic patterns, the length scales (periods) of the $R^{(\mathrm{buc})}$ state vortex lattice actually grow in time as the interface coarsens. In the $R^{(\mathrm{buc})}$ state, the distribution of interface slope vectors approaches a stable form, with maxima at $\mathbf{M}$ values *off* the zeros of $\mathbf{J}^{(NE)}(\mathbf{M})$ — cf. Fig. 14(b). Thus the uncommon $R^{(\mathrm{buc})}$ state *does* exhibit *slope distribution selection*, although there are no stable zeros of $\mathbf{J}^{(NE)}(\mathbf{M})$.

From the simulations, we find the $R^{(\mathrm{buc})}$ state exhibits a fast coarsening where the interface width is $w \sim t^{\beta}$ with $\beta \approx 0.4$, close to the center of the $R^{(\mathrm{buc})}$ range in Fig. 9. We recall that a similar enhanced roughening is also found in the intensely rough domain of the RhP phase, occurring close to the $R^{(\mathrm{buc})}$ domain in our kinetic phase diagram in Fig. 9 (cf. also Fig. 11 and related discussion). Another interesting structural aspect of the Buckled Rippled state, revealed in the simulations represented in Fig. 16, is the buckled form of the Rectangular Rippled state. Indeed, from Fig. 16(b) one can see that the large scale morphology of the $R^{(\mathrm{buc})}$ state is that of the $R^{(\mathrm{rec})}$ state with large huts and pits (inverted huts) forming a checkerboard structure. However, in contrast to the $R^{(\mathrm{rec})}$ state, the facets of the huts and pits of the $R^{(\mathrm{buc})}$ state are buckled — i.e. exhibit an additional modulation, with a wavelength much smaller than the size of the huts [cf. Fig. 16(b)]. This buckling deformation in the $R^{(\mathrm{buc})}$ state disappears as the X point in the phase diagram in Fig. 9 is approached — cf. Fig. 16(a). At the X-point, the interface morphology is that of the $R^{(\mathrm{rec})}$ state.

https://doi.org/10.4208/eajam.040411.030611a Published online by Cambridge University Press

In addition to the RhP state, the $R^{(\mathrm{buc})}$ state may qualify as the intermediate state seen in the erosion on Cu(110) and on Rh(110) surfaces [33, 35]. This is illustrated in Fig. 17, depicting detailed results of the simulations of the ripple rotation transition along a line going through the $R_1^{(\mathrm{buc})}$ state. Note that this figure is quite similar to Fig. 11, where this transition goes through the intensely rough RhP state. Thus by comparison with the nearly in-phase (FT) and out-of-phase (SD) diffraction data on Cu(110) and Rh(110) surfaces [33, 35], we argue that these experimentally observed ripple rotation transitions proceed with the intervention of either the intensely rough RhP state as in Fig. 11 or the $R_1^{(\mathrm{buc})}$ state as in Fig. 17. In addition to the diffraction data, this is supported by the intensely rough RhP and $R_1^{(\mathrm{buc})}$ states both exhibiting the experimentally observed enhanced coarsening with interface width $\sim t^{0.4}$. In both cases, the experimentally observed hot-rippled phase corresponds to our R_2 phase. By decreasing the temperature T, the R_2 facets destabilize and the interface transforms into the RhP or the $R_1^{(\mathrm{buc})}$ state. At this point, it is illuminating to recall Fig. 8, and in particular that the R_2-to-RhP transition is a Hopf bifurcation where R_2 facets destabilize and transform into the RhP facets that take over the interface morphology. Microscopically, this facet destabilization with decreasing T can be caused by Schwoebel barriers on the kinks on the terrace steps of the R_2 facets. These kinks are easily rounded by adatoms, but only at high enough T (so R_2 is stable there). With decreasing T, the R_2 facets destabilize due to the Schwoebel barriers, as the R_2 rippled state transforms into the RhP state. Moreover, a further temperature decrease can destabilize the RhP facets, and cause the transition into the fascinating $R_1^{(\mathrm{buc})}$ state when *all* flat facets are unstable — cf. again Fig. 8.

From the above discussion of the atomistic effects underlying the continuum model, the interface morphology transformations seen on Cu(110) and Rh(110) surfaces [33, 35] reflect one (or both) of the following two chains of far-from-equilibrium phase transitions.
Chain 1: with decreasing temperature,

$$R_2 \to RhP \to R_1^{(\mathrm{buc})}; \tag{4.11}$$

Chain 2: with decreasing temperature,

$$R_2 \to R_1^{(\mathrm{buc})} \ . \tag{4.12}$$

In both chains, R_2 is the "hot rippled" state and the $R_1^{(\mathrm{buc})}$ is the "cold rippled" state. Chain 1 has the intensely rough RhP as the intermediate state, manifest through the experimentally observed quartet slope distribution — cf. Fig. 11. On the other hand, Chain 2 in Eq. (4.12) does not involve an intermediate state at all, but also reproduces the experimental fact that the quartet slope distribution occurs in an intermediate temperature range. This is documented by the simulations in Fig. 17, which gives the

https://doi.org/10.4208/eajam.040411.030611a Published online by Cambridge University Press

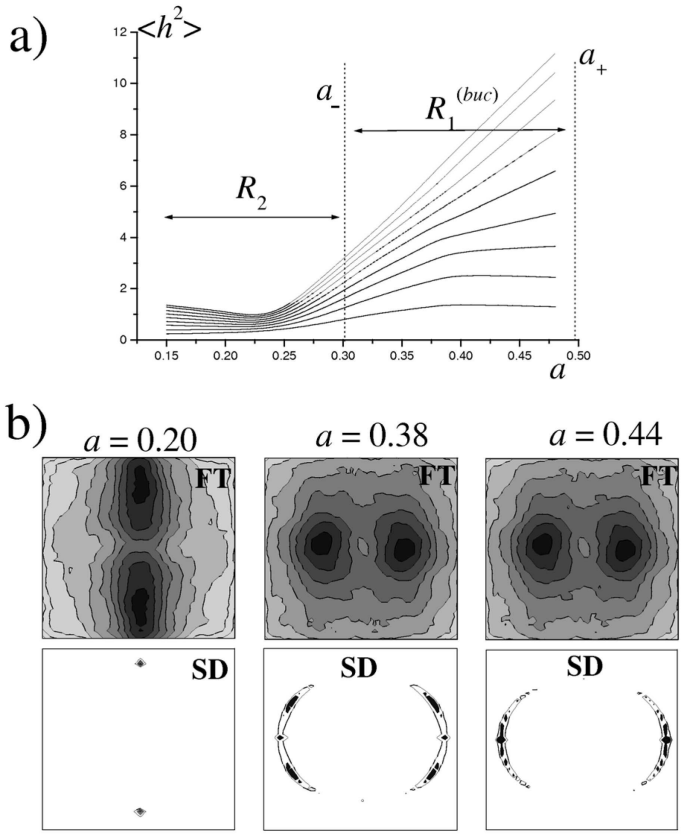

Figure 17: (a) The square of the interfacial width $< h^2 >$ versus parameter a for several different times, across the transition from the rippled state R_2 (for $a < a_-$) to the Buckled Rippled state $R_1^{(\mathrm{buc})}$ (for $a > a_-$). This transition does not involve an intermediate state. (This figure is obtained from numerous simulations done along the line $b = 1.1$ that goes from R_2 directly to the $R_1^{(\mathrm{buc})}$ state.) In Fig. (b), FT magnitudes and SDs found along the ripple rotation transition are shown, for $a = 0.2$ (in the R_2 state) and for $a = 0.38$ and 0.44 (both within the $R_1^{(\mathrm{buc})}$ range). Note the FTs (i.e. nearly in-phase diffraction patterns) of the $R_1^{(\mathrm{buc})}$ have just two peaks, like the R_1 pattern. Nevertheless, the SDs (i.e. out-of-phase diffraction patterns) distinguish the $R_1^{(\mathrm{buc})}$ from the R_1 state. Overall, the FTs and SDs of the $R_1^{(\mathrm{buc})}$ state are similar to those of the intensely rough RhP state in Fig. 11. However, note that the forms of the SDs of $R_1^{(\mathrm{buc})}$ are closer or even indistinguishable from those of the R_1 state — cf. the SD obtained for $a = 0.44$, within the $R_1^{(\mathrm{buc})}$ range.

in-phase (FT) and out-of-phase (SD) diffraction patterns for Chain 2 with only R_2 and $R_1^{(\mathrm{buc})}$ states involved. Note that the SD of the $R_1^{(\mathrm{buc})}$ state changes from the quartet form occurring near the R_2-to-$R_1^{(\mathrm{buc})}$ transition to the R_1-like doublet form occurring *even before* the $R_1^{(\mathrm{buc})}$-to-R_1 transition is reached. Thus the fascinating Buckled Rippled state $R_1^{(\mathrm{buc})}$ reproduces the observed behaviors, in both the intermediate (RhP-like) and in the ultimate low temperature (R_1-like) regimes seen experimentally [33, 35].

https://doi.org/10.4208/eajam.040411.030611a Published online by Cambridge University Press

4.2. Deciphering the role of vertical growth asymmetry

The physics of a thin film interface is naturally affected by the strong qualitative differences between the media and processes occurring above and below it. This up-down vertical asymmetry (VA) is an integral part in any realistic model of the interface dynamics. Epitaxial growth and erosion phenomena, such as discussed in this review, are no exceptions. For example, VA effects are clearly visible on the interfaces of homoepitaxially grown films, through the difference between the shapes of pyramids and pits (upside-down pyramids) that develop during the homoepitaxial growth on (001) and (111) crystal surfaces [44] — recall Fig. 1(b). Experimentally, it is impossible to "switch VA off" in order to see how much VA really matters. Major effects such as ESV and slope stabilization enter the continuum theory through surface non-equilibrium, which by itself does *not* introduce VA in a fundamental way — cf. § 2. Moreover, under some circumstances continuum modeling of epitaxial growth and erosion reproduces major features of the experimentally observed interface dynamics (e.g. coarsening exponents), even when VA effects are ignored [18, 19]. This leads us to a basic question: *Is VA primary or a secondary factor in epitaxial growth and erosion?* It is difficult if not impossible to address this question using microscopic (quasi-atomistic) modeling of the epitaxial growth phenomena, such as kinetic Monte Carlo simulations or other similar approaches [10]. Indeed, under a microscopic approach using a step flow model, in addition to the ESV and slope selection terms of the surface current there is also a VA current term that is *generally* nonzero [45] — i.e. one cannot eliminate (switch off) VA effects. Much like the experiments, realistic microscopic simulations of epitaxial growth *ubiquitously* include VA, and thus cannot be used to directly elucidate actual VA effects *per se* separately from other effects.

To address the role of VA, we pursued a conceptually different approach based on the phenomenological continuum model of interface dynamics in Eq. (4.1). In this approach [27], let us recall the interface is described by its height evolution equation that is generally of the form

$$\frac{\partial h(\mathbf{x},t)}{\partial t} = v_{\rm VS}(h) + v_{\rm VA}(h) \ , \tag{4.13}$$

where the local interface height velocity $v(h)$ is expressed as the sum of $v_{\rm VS}(h) = -v_{\rm VS}(-h)$ and $v_{\rm VA}(h) = v_{\rm VA}(-h)$ — i.e. its odd and even parts, respectively. The *even* part, $v_{\rm VA}(h)$ breaks the vertical reflection ($h \to -h$) symmetry of the interface dynamics, and thus introduces the VA effects. The separation into these different symmetry contributions in Eq. (4.13) allows us to directly extract generic VA effects, by comparing results obtained with nonzero VA to those obtained with zero VA. Indeed, within the continuum model (4.1) for (110) surfaces, it is straightforward to switch off the VA by setting the λ constants to zero and then compare the results to those obtained with nonzero λ constants. As mentioned, such a comparison is virtually impossible in experiments and microscopic kinetic simulations. In particular, we have explored the

https://doi.org/10.4208/eajam.040411.030611a Published online by Cambridge University Press

role of VA in epitaxial growth by considering in depth the effects on the growth and erosion on (110) crystal surfaces [27].

The most interesting VA effects were found in the type B behavior, where there is both stable and unstable facet behavior and the Rectangular Rippled states $R_1^{(\mathrm{rec})}$ and $R_2^{(\mathrm{rec})}$ are formed — cf. § 4.1. We recall that these interface states are checker-board structures of alternating rectangular pyramids and pits — cf. Figs. 7(c) and 13(b). Unlike the simple R_1 rippled state for example, a rectangular pyramid of the $R_1^{(\mathrm{rec})}$ state not only incorporates the long R_1 facets but also the significantly smaller metastable R_2 facets [25, 26]. Our Rippled Rectangular pyramid structures in Fig. 13(b) can be seen in the STM images obtained in erosion experiments on Ag(110) — cf. Fig. 4(d) of Ref. [31]. For the type B behavior seen in the ripple rotation transition on Ag(110) surface, it is shown in Ref. [27] that the surface diffraction patterns and underlying surface morphologies are strongly affected by vertical growth asymmetry. These findings, in agreement with the experimental data [30,31], provide the first clear evidence that VA plays a significant role in epitaxial growth and erosion on crystal surfaces. It has long been recognised, for example on (001) surfaces, that VA produces differences between the shapes of four-sided pyramids and pits (inverted pyramids) [44]. However, VA effects on interface structure and dynamics are still debated, and a better (but likely incomplete) understanding has only begun to emerge quite recently for the case of high symmetry (001) surfaces [29]. Our study [27] was the first *in depth* discussion of VA effects for the case of low symmetry (110) crystal surfaces, where it emerged that VA plays an essential role in the range where the Rippled Rectangular states form. Due to VA the ripple rotation transition is smeared out and extends over an extended parameter range. The transition point, at which the qualitative change of nearly in-phase diffraction pattern (surface Fourier transform magnitude) occurs, turns out to differ from the transition point at which the qualitative change of out-of phase diffraction pattern (facet slope distribution) occurs. At the former transition point, the four-lobe nearly in-phase diffraction pattern occurs with the four peaks along the principal axes of the (110) surface, in accord with experiments on Ag(110) [30]. Such a pattern and the underlying surface morphology are different from those occurring with zero VA shown in Fig. 13(b, middle panel). *This theoretical finding, and its consistency with experiment, demonstrates for the first time that VA can induce the formation of unique surfaces morphologies that would otherwise be absent (with zero VA)*. Moreover, on the two sides of the extended ripple rotation transition we find two interesting interface states, which are qualitatively altered forms of the Rectangular Rippled states. These two novel interface states are both induced by the VA, and correspond well to the interface morphologies seen in STM images [31]. One exhibits an enhanced roughening, which was seen in the experiments on Ag(110) surface [31]. This intensely rough interface state is an exotic alteration of the rectangular rippled $R_1^{(\mathrm{rec})}$ state, with rectangular pyramids replaced by arrays of small (nearly) square shaped pyramids packed between long rectangular pits. The other interface state revealed in Ref. [27] is an altered form

https://doi.org/10.4208/eajam.040411.030611a Published online by Cambridge University Press

of the rectangular rippled $R_2^{(\mathrm{rec})}$ state. It has depressed pit sizes, where the roof-top edges of elongated worm-like mounds are decorated by exotic arrays of small rounded mounds, but does not exhibit enhanced roughening. Due to the difference between the roughening character of these two exotic states, the interface data are highly asymmetric across the ripple rotation transition, as seen in the experiments on Ag(110) [30,31].

The results in Ref. [27] reviewed below were obtained by simulations and analytic arguments using the general continuum model Eq. (4.1), for the growth and erosion of (110) crystal surfaces. The VA enters the model through terms that have coefficients labeled in Eq. (4.1) as λ_{ij} — cf. also Eq. (2.4). By an anisotropic rescaling of the coordinates (x_1, x_2), the contributions to the model (4.1) that originate from the non-equilibrium surface current $\mathbf{J}^{\mathrm{NE}}$ in Eq. (2.6) can be made to depend on only the three dimensionless parameters (a, b, c) met in § 4, as discussed in Ref. [26] — cf. Eqs. (2.15) and (2.16) there. In the resultant rescaled model, $\mathbf{J}^{\mathrm{NE}}$ is given by Eq. (2.6) with $r_1 = 1 + a$, $r_2 = 1 - a$, $u_{11} = u_{22} = 1$, $u_{12} = b + c$, $u_{21} = b - c$ as employed hereafter. Preferred interface slopes correspond to zeros of $\mathbf{J}^{\mathrm{NE}}(\mathbf{M})$, and in the rescaled model the R_1 doublet of facets that gives rise to the R_1 rippled state occurs at the slopes

$$M_1 = \pm\sqrt{1+a}, \qquad M_2 = 0\ . \tag{4.14}$$

Likewise, the R_2 doublet of facets giving rise to the R_2 rippled state occurs at the slopes

$$M_1 = 0, \qquad M_2 = \pm\sqrt{1-a}\ . \tag{4.15}$$

The slopes in Eqs. (4.14) and (4.15) are shown in Fig. 18(a). Importantly, the R_1 and R_2 facets in Eqs. (4.14) and (4.15) are *both* stable for the parameter a in the range displayed in Eq. (4.7) — viz.

$$a_+(b,c) < a < a_-(b,c)\ ,$$

with $a_+ = (1 - b + c)/(1 + b - c)$ and $a_- = (1 - b - c)/(1 + b + c)$. For $a_+ < a_-$ (i.e. for $b > \sqrt{1 + c^2}$), the multi-stable type B behavior with the Rectangular Rippled states $R_1^{(\mathrm{rec})}$ and $R_2^{(\mathrm{rec})}$ develops even for zero VA (cf. Refs. [25,26] and § 4.1 here). However, in [27] the primary interest was in VA effects on the interface morphologies occurring in this range. The results of the simulations revealed that VA effects are essential to elucidate the experiments that reported the ripple rotation transition on the Ag(110) crystal surface [30,31]. Within our model, as in homoepitaxial growth experiments on the Ag(110) [30], the transition occurs within a multi-stable system parameter range where the R_1 and R_2 facets are stable. The slopes of these facets as given by Eqs. (4.14) and (4.15) are depicted in Fig. 18(a), versus the control parameter a. The facet slope and multi-stability behavior seen in our Fig. 18(a) are in remarkable qualitative agreement with that seen on Ag(110) with changing substrate temperature (cf. Fig. 3(a) of Ref. [30]), provided a is identified as a temperature-like control parameter in the experiments. As discussed in § 2, the VA current is a curvature current that vanishes

https://doi.org/10.4208/eajam.040411.030611a Published online by Cambridge University Press

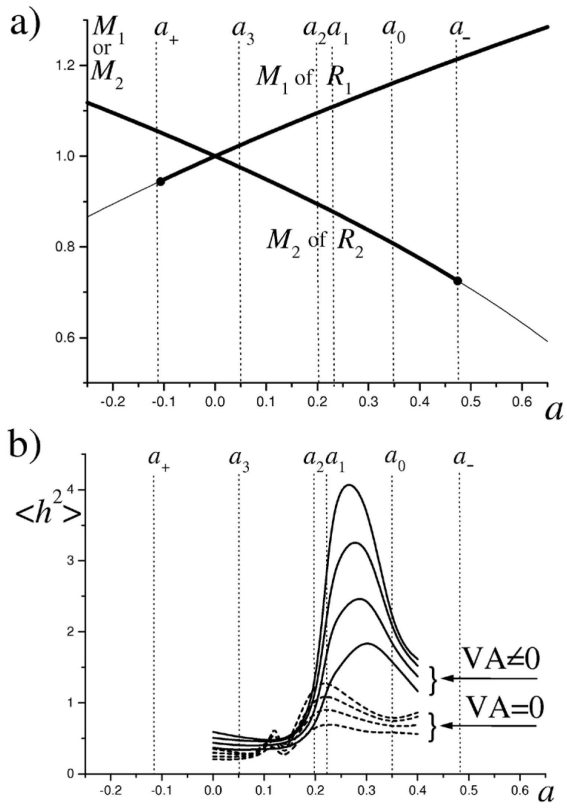

Figure 18: Multi-stable range involved in the transition from the $R_2^{(\mathrm{rec})}$ to the $R_1^{(\mathrm{rec})}$ state. (a) Variations of the slopes of the R_1 and R_2 facets, respectively $M_1 = \sqrt{1+a}$ and $M_2 = \sqrt{1-a}$, versus the temperature-like dimensionless parameter a. Facet slopes are shown by thick (thin) lines for stable (unstable) facets. Both R_1 and R_2 facets are stable for a in the range $a_+ < a < a_-$. (b) Variation of the square of the interface width $< h^2 >$ obtained from the simulations, given by solid lines for several different deposition times versus the parameter a (for nonzero VA). Labeled are the four characteristic values of a — viz. $a_3 < a_2 < a_1 < a_0$ as discussed in the text. (This figure is reproduced from Ref. [27].)

on flat facets, so does not affect the magnitudes of the selected slopes of the flat facets R_1 and R_2. They are determined purely by the form of the non-equilibrium current in Eqs. (4.14) and (4.15) depicted in Fig. 18(a). Nonetheless, the VA does qualitatively affect the long length-scale interface morphology in an ample range around the transition — compare Fig. 20 obtained with a nonzero VA and Fig. 13(b) obtained with zero VA. As detailed hereafter, the experimental data [30, 31] are in accord with the predictions from our theory *provided the VA is incorporated into the modeling*. Of practical significance are the experimental surface diffraction patterns [30] — i.e. the nearly in-phase and out-of-phase diffraction patterns, corresponding to the surface Fourier transform (FT) magnitude and slope distribution (SD) obtained from the simulations respectively. Here we show that various experimental data on Ag(110) growth [30]

https://doi.org/10.4208/eajam.040411.030611a Published online by Cambridge University Press

and erosion [31] can be understood physically only if nonzero VA is incorporated in the theory. Unlike the simple rippled states, each of the two $R^{(\mathrm{rec})}$ states involves both R_1 and R_2 facets — cf. Figs. 7(c) and 13(b). These two facet types are not equivalent (i.e. not symmetry related) to each other, so in general they can coexist only across the moving edges between them [25, 26]. Due to the edge motion in the $R_1^{(\mathrm{rec})}$ state, the R_1 facets grow faster than the R_2 facets, whereas in the $R_2^{(\mathrm{rec})}$ state the R_2 facets grow faster than the R_1 facets. This edge motion produces the surface morphologies seen in the Rectangular Rippled states — cf. Fig. 13. Only at a specific (critical) point can there be a static edge between the R_1 and R_2 facets — cf. Fig. 13(b, middle panel). For zero VA, this point occurs at $a = a_{cr}$, with a_{cr} as in Eq. (4.8). For $a = a_{cr}$, the interface dynamics equation (4.1) has a steady solution ($\partial h/\partial t = 0$), corresponding to a *static edge* between semi-infinite R_1 and R_2 facets. Such an edge is an analogue of the classical equilibrium Gibbs interfaces that only exist at phase transitions points. For zero VA, the critical value of the control parameter a in Eq. (4.8) corresponds to the transition point between the $R_1^{(\mathrm{rec})}$ and $R_2^{(\mathrm{rec})}$ states [25, 26]. At this critical point, R_1 and R_2 facets can coexist across the static edges, which allows the non-equivalent R_1 and R_2 facets to grow at the same rate. Instead of Rectangular Rippled structures, the checker-board structure of four-sided pyramids arises — cf. Fig. 13(b, middle panel), from our zero VA simulations at $a = a_{cr}$. Thus by a Gibbs-like argument (with equilibrium Gibbs' interfaces between different phases corresponding to static edges between non-equivalent facets), one can analytically locate the phase transition point given by Eq. (4.8) — and further, elucidate in great detail the far-from-equilibrium phase transitions encountered in epitaxial growth and erosion.

For nonzero VA, these far-from-equilibrium transitions can also be discussed by searching for the static edge solutions of Eq. (4.8). However, for nonzero VA an additional complexity emerges, because there are then two distinct edge types between the R_1 and R_2 facets as shown in Fig. 19 — viz. (i) *convex* edges, such as the uphill edges emerging from the pit-bottom edges of the rectangular shaped pits of the $R^{(\mathrm{rec})}$ state in Fig. 19(a); and (ii) *concave* edges, such as the downhill edges emerging from the roof-top edges of the rectangular shaped pyramids of the $R^{(\mathrm{rec})}$ state in Fig. 19(b). For *zero* VA, these two types of static R_1-R_2 edges are simply related to each other, because if $h(\mathbf{x})$ is a static solution of Eq. (4.1) then so is $-h(\mathbf{x})$. Thus the static concave downhill edge is directly obtained from the static convex uphill edge, simply by vertical reflection of the interface profile $h(\mathbf{x})$. For zero VA, both types of static edges exist for the *same* critical value of the parameter a given in Eq. (4.8). However, with *nonzero* VA, the vertical reflection $h \to -h$ ceases to be a symmetry of the interface dynamics — i.e. if $h(\mathbf{x})$ solves Eq. (4.1), then $-h(\mathbf{x})$ does not (for the *same* value of a). Consequently, for nonzero VA the necessary value of a for the existence of the static convex uphill edge [cf. Fig. 19(a)] is generally *different* from the necessary value for the existence of the static concave downhill edge [cf. Fig. 19(b)]. Let us call these two special (critical) control parameter values a_{convex} and a_{concave} where $a_{\mathrm{convex}} \neq a_{\mathrm{concave}}$ unless VA is zero, when a_{convex} and a_{concave} both equal the identical critical value given by Eq. (4.8).

https://doi.org/10.4208/eajam.040411.030611a Published online by Cambridge University Press

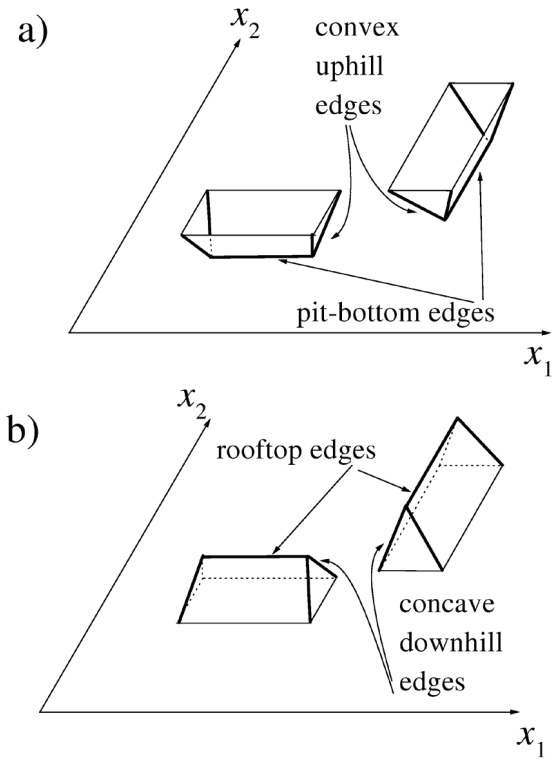

Figure 19: (a) Convex uphill edges between R_1 and R_2 facets, emerging from the long edges along the bottoms of rectangular shaped pits. For $a \neq a_{\rm convex}$ the uphill edges move, so pits grow in length either along the x_1-direction (like in the $R_1^{(\rm rec)}$ state) or along x_2-direction (as in the $R_2^{(\rm rec)}$ state). (b) Concave downhill edges occur between R_1 and R_2 facets, emerging from the long edges along the roof-tops of rectangular shaped pyramids. For $a \neq a_{\rm concave}$, the downhill edges move so the roof-tops grow in length, either along the x_1-direction (like in the $R_1^{(\rm rec)}$ state) or along the x_2-direction (like in the $R_2^{(\rm rec)}$ state). (This figure is reproduced from Ref. [27].)

The existence of two distinct critical points is evidently the major factor responsible for the complex VA-induced interfacial morphologies [27]. The actual values of $a_{\rm convex}$ and $a_{\rm concave}$ were calculated analytically in Ref. [27] by applying the generalized Gibbs argument — i.e. by finding the necessary conditions for the existence of static edge solutions of the interface evolution equation (4.1) with nonzero VA. For a *positive* VA, the likely situation in epitaxial growth and erosion, we have

$$a_{\rm convex} < a_{\rm concave} \ . \tag{4.16}$$

On (001) surfaces for example, positive VA values favor rounder tops of four-sided pyramids and sharper four-sided pyramidal pits, relative to zero VA morphologies with no difference between tops and pits widths — cf. Fig. 1(b). Experiments on (001) surfaces indeed show these typical features (for a positive VA), well illustrated by micrographs of the checkerboard structure of alternating four-sided pyramids and pyramidal pits on

https://doi.org/10.4208/eajam.040411.030611a Published online by Cambridge University Press

Cu(001) surfaces [44]. A similar effect for positive VA is seen in the facet edge widths, with convex edges narrower and concave edges broader (relative to their widths at zero VA) — cf. Fig. 26(i) in § 5.

To elucidate the full meaning and implications of the points $a_{\rm convex}$ and $a_{\rm concave}$ for interface morphology, we carried out extensive numerical simulations using Eq. (4.1). These simulations revealed the existence of four characteristic a parameter values we ordered as $a_3 < a_2 < a_1 < a_0$, related to the VA — cf. Figs. 18, 20, and 21. There is a very rippled rotation transition in a narrow range between a_2 and a_1. Quantitative comparisons between our analytic results and the simulations showed that $a_{\rm convex} \approx a_3$ and $a_{\rm concave} \approx a_2 \approx a_1$. From Eq. (4.16), on decreasing the control parameter a the system first encounters $a_{\rm concave}$, at which the concave downhill edges emerging from the roof-tops of the $R_1^{(\rm rec)}$ state rectangular pyramids become static — cf. Fig. 19(b). On further decreasing a, the system encounters $a_{\rm convex}$, at which the convex uphill edges emerging from the bottoms of the $R_2^{(\rm rec)}$ rectangular pits become static — cf. Fig. 19(a).

Consequently, with decreasing control parameter a there are several qualitatively different interface morphologies due to these features, encountered as follows.
(i) For a sufficiently greater than $a_{\rm concave} > a_{\rm convex}$, both the roof-tops and pit bottoms grow along the x_2 direction, quite like when VA is zero — cf. Fig. 13. Thus the interface is then in the $R_1^{(\rm rec)}$ state, as in the simulations for $a > a_0 > a_{\rm concave}$ shown in Fig. 20(f).
(ii) For $a \approx a_{\rm concave} > a_{\rm convex}$, the concave downhill edges emerging from the roof-tops become nearly static — cf. Fig. 19(b). This feature hinders the growth of roof-tops in the range $a_1 < a < a_0$, but as $a > a_{\rm convex}$ the pits are still prone to grow in length. This is exactly the situation seen in simulations shown in Fig. 20(e) for a in this range, which show the growth of long pits and also that long rectangular roof-tops cease to develop — rather, they break into arrays of small four-sided pyramids as in Fig. 20(e). This is the *altered* form of the $R_1^{(\rm rec)}$ state that we call the $AltR_1^{(\rm rec)}$ state, shown in Fig. 20(e) and discussed in more detail below.
(iii) For $a \approx a_{\rm convex} < a_{\rm concave}$, the convex uphill edges emerging from the pit bottoms become nearly static — cf. Fig. 19(a). This feature hinders the growth of pits, but as $a < a_{\rm concave}$ the roof-tops are prone to grow in length. This is exactly the situation we see in simulations as shown in Fig. 20(b) for the range $a_3 < a < a_2$, showing the growth of long roof-tops and pit bottoms depressed in size that do not grow substantially with time. This is the *altered* form of the $R_2^{(\rm rec)}$ state that we call the $AltR_2^{(\rm rec)}$ state, shown in Fig. 20(b) in the range $a_3 \approx a_{\rm convex} < a < a_2 \approx a_{\rm concave}$ and also discussed in detail below.
(iv) For a below $a_{\rm convex} (< a_{\rm concave})$, both the roof-tops and pit-bottoms grow along the $x_1$direction much as for zero VA, as shown in Fig. 13(b). Thus the interface is in the $R_2^{(\rm rec)}$ state if $a < a_{\rm convex}$, as in the simulations for $a < a_3 \approx a_{\rm convex}$ shown in Fig. 20(a).

In addition to the multitude of interfacial states, there are other consequences to

https://doi.org/10.4208/eajam.040411.030611a Published online by Cambridge University Press

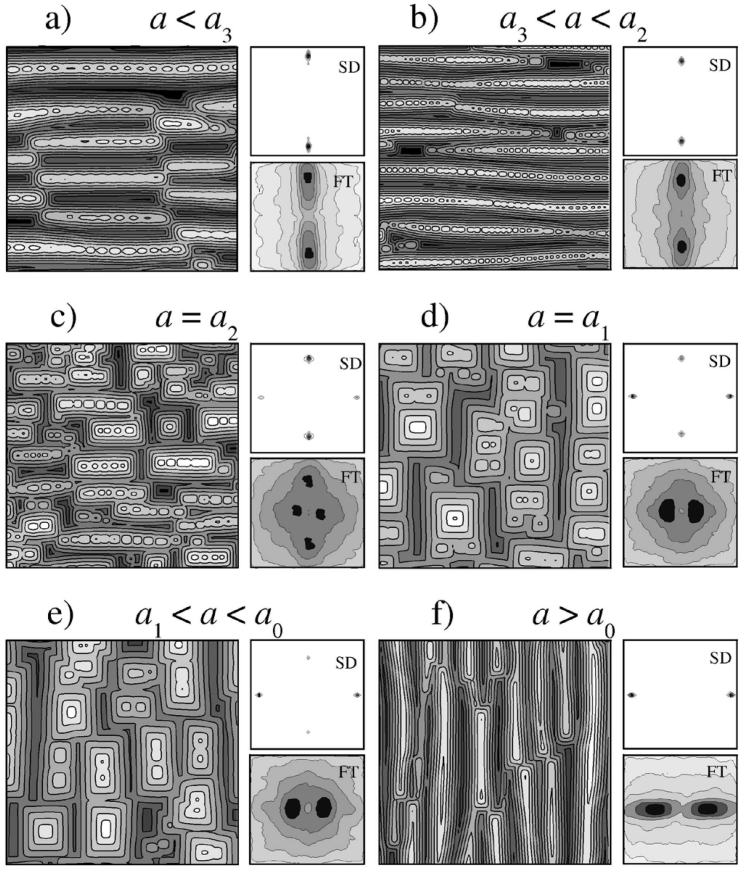

Figure 20: Effects of the VA on the interface morphology (given by surface contour plots) and interface diffraction data (SD and FT), across the transition from $R_2^{(\mathrm{rec})}$ to $R_1^{(\mathrm{rec})}$ state. (a) The $R_2^{(\mathrm{rec})}$ state, with a checkerboard arrangement of rectangular elongated pyramids and pits (inverted roof-tops). (b) Altered form of $R_2^{(\mathrm{rec})}$ state (worm-like ripples), where the pit sizes are depressed and that arrays of small rounded mounds form along roof-tops of elongated pyramids. (c) Interface morphology at the point where surface FT exhibits four peaks of equal magnitude (four-lobe pattern) corresponds to rectangular mounds packed side-by-side. (d) Interface morphology at the point where surface SD exhibits four peaks of equal magnitude. (e) Altered form of the $R_1^{(\mathrm{rec})}$ state (square-pyramid-like state), where roof-top-like pyramids are replaced by arrays of nearly square shaped four-sided pyramids packed between longer in size pits (inverted roof-tops). (f) The $R_1^{(\mathrm{rec})}$ state, with a checkerboard arrangement of rectangular elongated pyramids and pits (inverted roof-tops).

consider. The VA affects the concave uphill edges and concave downhill edges differently, as they become static at the two distinct values of the system control parameter, a_{convex} and a_{concave}. This produces a complex kinetic phase diagram, as suggested by the simulation results shown in Fig. 20. In addition to the Rectangular Rippled states $R_1^{(\mathrm{rec})}$ (Fig. 20(f)) and $R_2^{(\mathrm{rec})}$ [cf. Fig. 20(a)], the phase diagram involves two VA-induced interface states — viz. the Altered $R_1^{(\mathrm{rec})}$ state [Fig. 20(e)] and the Altered

https://doi.org/10.4208/eajam.040411.030611a Published online by Cambridge University Press

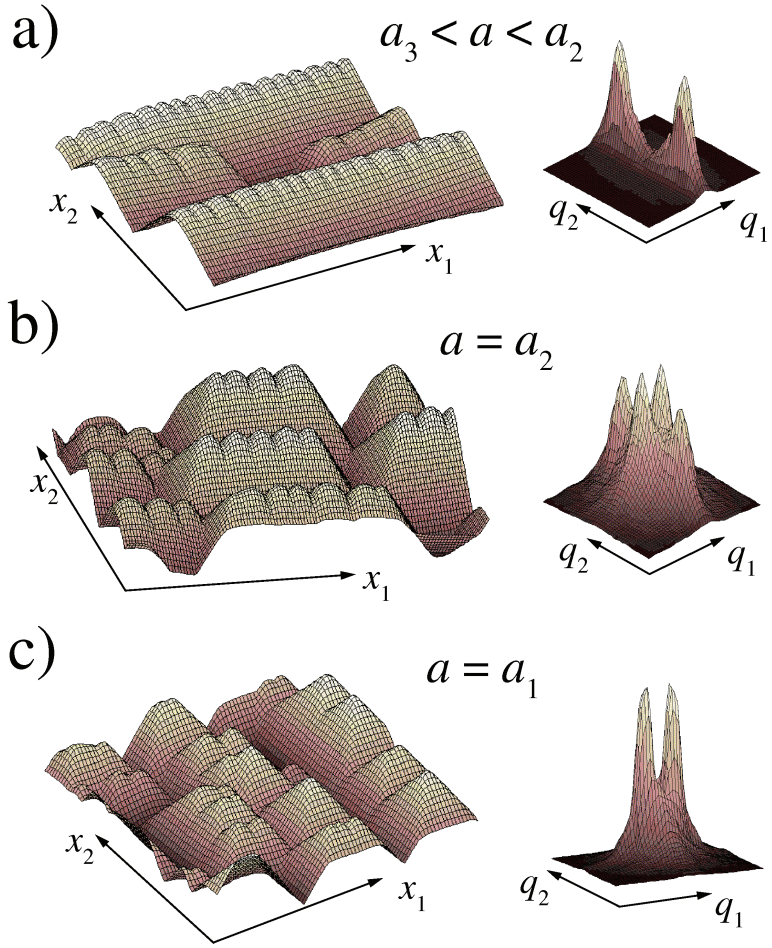

Figure 21: 3D views of the real-space interface morphology and the corresponding FTs (i.e. near in-phase diffraction patterns) for a nonzero VA, at several successive points along the ripple rotation transition between the Rectangular Rippled states. (a) Altered form of the $R_2^{(\mathrm{rec})}$ state where pit sizes are depressed, whereas arrays of small mounds form along roof-tops. Note that this structure yields a FT that is essentially the same as that of the $R_2^{(\mathrm{rec})}$ state, with just two peaks at $(0, \pm q_2)$ — cf. also, Figs. 20(a) and (b). (b) The FT forms with two pairs of peaks, at $(\pm q_1, 0)$ and $(0, \pm q_2)$, having nearly equal magnitudes (four-lobe pattern). This corresponds to the transition at $a = a_2$ as discussed and seen on Ag(110), where the interface structures itself into rectangular pyramids sitting side-by-side [30] — cf. also Fig. 20(c)]. (c) The altered form of the $R_1^{(\mathrm{rec})}$ state, with roof-top edges replaced by arrays of nearly square shaped four-sided pyramids — cf. also Figs. 20(d) and (e). This complex structure has qualitatively the same FT as $R_1^{(\mathrm{rec})}$, with just two peaks at $(\pm q_1, 0)$ — cf. also, Figs. 20(d), (e), and (f). (This figure is reproduced from Ref. [27].)

$R_2^{(\mathrm{rec})}$ state [Fig. 20(b)], and the ripple rotation transition proceeds between these two states.

Let us now compare our theoretical results with the experimental STM data of Ref. [31] for ion beam erosion of Ag(110), and the diffraction data of Ref. [30] for

https://doi.org/10.4208/eajam.040411.030611a Published online by Cambridge University Press

epitaxial growth on Ag(110). In both cases, the system control parameter used was the substrate temperature. These experimental data are related to the wealth of theoretically predicted interfacial phenomena shown in Figs. 20 and 21, produced by VA on (110) crystal surfaces in the ripple rotation transition involving the rectangular rippled states $R_1^{(\mathrm{rec})}$ and $R_2^{(\mathrm{rec})}$. Across this transition, as the temperature-like parameter a varies there are various interesting transitions occurring at *six* characteristic points ordered as $a_+ < a_3 < a_2 < a_1 < a_0 < a_-$.

(i) In the range $a < a_+$, the ordinary rippled state R_2 occurs.

(ii) In the range $a_+ < a < a_3$, the $R_2^{(\mathrm{rec})}$ state occurs — cf. Fig. 20(a).

(iii) In the range $a_3 < a < a_2$, the $AltR_2^{(\mathrm{rec})}$ state occurs, with depressed pit sizes and roof-top edges decorated by arrays of small rounded mounds. Nevertheless, all standard diffraction data of this state are the same as those for the $R_2^{(\mathrm{rec})}$ state — cf. Figs. 20(b) and 20(a). The elongated pyramids of the $AltR_2^{(\mathrm{rec})}$ state have *worm-like shapes*. Such a worm-like ripple morphology is seen in the STM image in Fig. 4(b) of Ref. [2], which parallels Fig. 20(b) and can be viewed as obtained by cutting an infinitely long worm into segments. The "cutting" is provided by the small pits placed between the long segments as shown in Fig. 20(b), in accord with the STM image in Fig. 4(b) of Ref. [2]. In addition, in the same STM image one can see modulation of the widths of worm-like pyramids (pearl-like substructures), corresponding to the arrays of small rounded mounds in Fig. 20(b).

(iv) At $a \approx a_2$, the interface structures appear as rectangular mounds sitting side-by-side, and the in-phase diffraction pattern exhibits two equally strong pairs of peaks at $(\pm q_1, 0)$ and $(0, \pm q_2)$, as shown in Figs. 20(c) and 21(b). This corresponds to the four-lobe nearly in-phase diffraction pattern observed in Ref. [30], at the ripple rotation transition on Ag(110). We recall there is no such FT interface pattern present with zero VA — cf. Fig. 13(b, middle panel), where the four-lobe FT pattern has peak positions different from those seen in both the experiments [30] and simulations in Figs. 20(c) and 21(b) with nonzero VA. Thus our theoretical results with nonzero VA, in combination with experiments [30], provide clear evidence that VA plays a significant qualitative role in epitaxial growth and erosion on crystal surfaces. This alone demonstrates that nonzero VA induces the formation of unique interface morphologies, different from those that occur for zero VA — cf. Figs. 20(c) and 13(b).

(v) The range $a_2 < a < a_1$, characterized by a steep increase of the interface roughness in Fig. 18(b), is an extended ripple rotation transition region. The interface SD (out-of-phase diffraction pattern) in this region is more like that of the $R_2^{(\mathrm{rec})}$ state, whereas the interface FT (the in-phase diffraction pattern) is more like that of the $R_1^{(\mathrm{rec})}$ state.

(vi) At $a \approx a_1$, the interface SD (i.e. out-of-phase diffraction pattern) has two equally strong peaks at $(\pm M_1, 0)$ and $(0, \pm M_2)$, as shown in Fig. 20(d).

(vii) For the range $a_1 < a < a_0$, the $AltR_1^{(\mathrm{rec})}$ state occurs, which importantly exhibits enhanced roughening as shown in Fig. 18(b). Morphologically, the $AltR_1^{(\mathrm{rec})}$ state can be characterized as the $R_1^{(\mathrm{rec})}$ state with roof-top edges replaced by arrays of small

https://doi.org/10.4208/eajam.040411.030611a Published online by Cambridge University Press

nearly square shaped pyramids packed between long pits, as shown in Fig. 20(e). Consequently, all diffraction data of the intensely rough $AltR_1^{(\mathrm{rec})}$ state are almost the same as those of the $R_1^{(\mathrm{rec})}$ state occurring for $a > a_0$ — cf. Fig. 20(f). Such an intensely rough state has been seen in the ripple rotation transition of Ag(110) in epitaxial erosion experiments [31], and in the STM image in Fig. 4(c) of Ref. [31] there are side-by-side nearly square shaped pyramids characteristic of the $AltR_1^{(\mathrm{rec})}$ state — cf. Fig. 20(e).
(viii) For $a_0 < a < a_-$, just next to the STM image of Ref. [31] there are rectangular pyramids of the $R_1^{(\mathrm{rec})}$ state, with Fig. 20(f) corresponding to the STM image in Fig. 4(d) of Ref. [31]. This state is a checkerboard arrangement of rectangular elongated pyramids and pits (inverted roof-tops).
(ix) Finally, in the range $a > a_-$ the simple rippled state R_1 occurs (not shown in Fig. 20 but see Fig. 9), corresponding to the STM image in Fig. 4(e) of Ref. [31] that illustrates the presence of rippled state dislocations theoretically predicted in Refs. [26, 28] — cf. § 4.1 and § 4.3 here. In addition to the agreement between theory and the experimental surface morphology data on Ag(110) in Ref. [30, 31], there is quite remarkable agreement with the experimental surface roughness and feature size data measured across the ripple rotation transition [31], which are highly asymmetric across the transition in accord with the simulation results shown in Fig. 18(b). Our theory explains this asymmetry, in terms of the difference between the roughening character of the worm-like Altered $R_2^{(\mathrm{rec})}$ state with surface roughness $\sim t^{0.25}$ in Fig. 20(b) and the significantly rougher square pyramid-like Altered $R_1^{(\mathrm{rec})}$ state with roughness $\sim t^{0.4}$ shown in Fig. 20(e) from simulations [28].

A comparison of Fig. 13(b) and Fig. 20 also well illustrates significant effects induced by the VA. The morphology of the standard Rectangular Rippled states in the proximity of the ripple rotation transition is qualitatively different. Two new types of interfacial states emerge, the Altered $R_1^{(\mathrm{rec})}$ state and the Altered $R_2^{(\mathrm{rec})}$ state, purely due to the VA. Importantly, the very rippled rotation occurs as a transition between the two Altered Rectangular Rippled states, and due to VA the transition occurs over an extended parameter range interposed between the Altered state ranges. As VA $\to 0$, the ranges of the Altered $R_1^{(\mathrm{rec})}$ and Altered $R_2^{(\mathrm{rec})}$ states — and the ripple rotation transition range — *all shrink to a single critical point*, the a_{cr} in Eq. (4.8). For zero VA, we recall that a_{cr} was identified as the single critical point at which the R_1 and R_2 facets coexist across *static edges* — cf. Eq. (4.8). However, the VA affects the concave uphill edges and concave downhill edges differently, so they become static at the two distinct values of the system control parameter a_{convex} and a_{concave}, which merge into a_{cr} in the zero VA limit. This seminal VA effect gives rise to the complex kinetic phase diagram involving the Altered $R_1^{(\mathrm{rec})}$ state, the Altered $R_2^{(\mathrm{rec})}$ state and the extended ripple rotation transition range. The role of VA is indeed profound: in the zero VA limit, the rich interfacial behaviors emerging due to VA in Figs. 20(b),(c),(d), and (e) all shrink to the single critical point given by Eq. (4.8), corresponding to the interface morphology seen in Fig. 13(b, middle panel).

https://doi.org/10.4208/eajam.040411.030611a Published online by Cambridge University Press

Our focus in the above discussion is on the type B ripple rotation transition that involves the multi-stable region in the epitaxial growth and erosion experiments on Ag(110) [30, 31], where R_1 facets $(\pm M_1, 0)$ and R_2 facets $(0, \pm M_2)$ are both stable. An alternative scenario for this transition, anticipated in Ref. [25] and then observed on Rh(110) and Cu(110) surfaces [33, 35], is the type A behavior that involves the intermediate Rhomboidal Pyramid (RhP) state discussed in § 4.1. The RhP structures are 2D arrays of four-sided pyramids and pyramidal pits with rhomboidal contour lines. The RhP state pyramids consist of facets with a quartet of four *equivalent* (symmetry related) slope vectors $(\pm M_1, \pm M_2)$ — cf. Fig. 8. In accord with experiments [33, 35], the RhP state exhibits an enhanced roughening with $< h^2 >^{1/2} \sim t^{0.4}$ for zero VA [26] — cf. § 4.1. In addition, the SD and FT data for the RhP state obtained for zero VA [26] are qualitatively the same as the data obtained in the experiments on Rh(110) and Cu(110) [33, 35], so the VA does not substantially alter the RhP state. Further, the RhP four-sided pyramids arise from the quartet of four equivalent facets. By symmetry, such facets can coexist across static edges *whatever* the values of the system control parameter or the VA may be. Varying the VA value only produces quantitative differences between the widths of the convex and concave edges on the four-sided pyramids and pits, as seen on (001) surfaces — cf. [29] and § 5 . In contrast to the RhP pyramids, the Rectangular Rippled states have pyramids consisting of the two types of facets R_1 at $(\pm M_1, 0)$ and R_2 at $(0, \pm M_2)$, which are oriented along the two *non-equivalent* principal axes of (110) — cf. the SDs in our figures. Such *non-equivalent* facets are not related to each other, and can therefore coexist across static edges only at *special* values of the system control parameter affected by the VA. This significantly influences the structural dynamics and kinetic phase transitions of the interface for the type B systems, with the ripple rotation transition going through the multi-stable system parameter region where the R_1 and R_2 facets are both stable.

4.3. Large scale topological defects mediating surface growth

Unlike the high symmetry (001) and (111) surfaces on which growing pyramidal structures form, the dominant structures on low symmetry rectangular (110) surfaces are the so-called rippled states [30–35]. They are one-dimensionally periodic surface structures, seen on (110) crystal surfaces of various materials such as Ag, Cu, and Rh [30, 31, 33, 35]. The rippled state wave-vector points along one of the two principal (high symmetry) directions of the (110) surface, and the rippled state surface profile is simply a zigzag line — i.e. the surface consists of long facets with slope vectors that alternate from parallel to anti-parallel to one of the two principal directions of the (110) crystal surface (cf. Fig. 22).

The two principal directions of (110) are not equivalent (symmetry related). Thus depending on the choice of the preferred direction, there are two major kinds of rippled states, R_1 and R_2 [25, 26]. By changing the substrate temperature, the deposition

https://doi.org/10.4208/eajam.040411.030611a Published online by Cambridge University Press

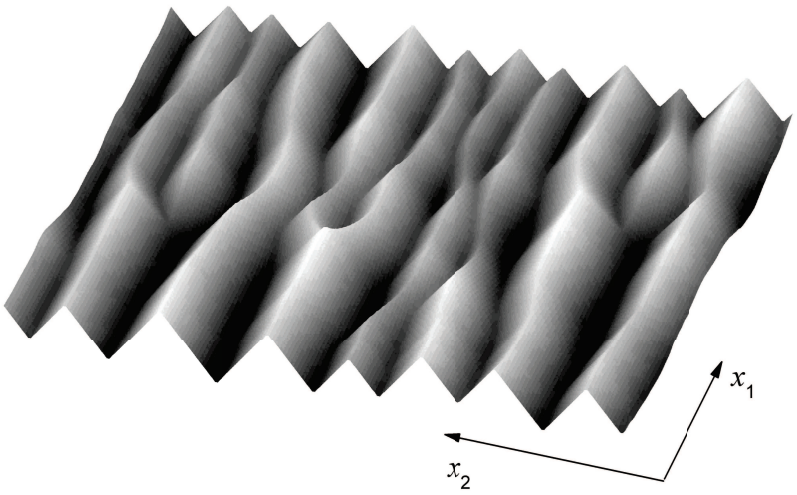

Figure 22: 3D plot of the (110) surface in the rippled state R_2 from simulations. Note the facets that have a finite extent along the x_1 direction, where they are terminated by dislocation-like topological defects. Two knife-like dislocations are seen on the left and the right side of surface section. whereas in the middle a fork-like dislocation is present. The presence of the dislocations breaks the perfect periodic order of the rippled state R_2 along the x_2 direction.

(or erosion) flux intensity and the molecular beam energy, de Mongeot and coworkers were able to drive the so-called ripple rotation (by 90°) transition between the two kinds of rippled states [30, 31, 33, 35]. These experiments and theory [25–27] both suggest this transition is complex, involving the formation of interesting intermediate states between the two rippled states. One is the Rhomboidal Pyramid (RhP) state, theoretically predicted in Ref. [25] and subsequently observed in epitaxial erosion experiments on Rh(110) and Cu(110) surfaces [33]. Alternatively, the ripple rotation transition may proceed through a multi-stable parameter range, where both types of rippled state facets (R_1 and R_2) are locally stable [25–27]. This multi-stable range is realized in experiments on Ag(110) surfaces, in both epitaxial growth [30] and erosion studies [31]. As theoretically revealed in Refs. [25, 27], due to multi-stability the simple Rippled states R_1 and R_2 are replaced by more complex Rectangular Rippled states $R_1^{(\mathrm{rec})}$ and $R_2^{(\mathrm{rec})}$, which are (disordered) checker-board structures of alternating rectangular pyramids and pits. For example, unlike the simple R_1 state, a rectangular pyramid of the $R_1^{(\mathrm{rec})}$ state incorporates not only the long R_1 facets but also significantly smaller metastable R_2 facets [25–27]. Rippled Rectangular pyramid structures are clearly seen in the STM images from erosion experiments on Ag(110) — cf. Fig. 4(d) of Ref. [31].

In reality, the structures of the simple Rippled and Rectangular Rippled states do not have a long range positional (periodic) order, as seen in the simulations shown in Figs. 12 and 22. Experimentally, the lack of long range positional order corresponds to a finite width of the correlation peaks in the nearly in-phase surface diffraction data

https://doi.org/10.4208/eajam.040411.030611a Published online by Cambridge University Press

of the rippled states [30]. The perfect periodic order is destroyed by dislocation-like topological defects that break the coherence of these structures — cf. Refs. [25,26] and Figs. 12 and 22 here. Due to dislocations, ripples only have a finite coherence length ξ, corresponding to the typical separation between the dislocations along a ripple [3,16]. Importantly, the simulations show that the Rippled state period λ and the ripple amplitude w ($\sim$ surface roughness) grow via a coarsening process involving the motion and annihilations of these dislocations [25, 26]. Unlike the dislocations in standard near-equilibrium systems [43], the dislocations of the growing rippled states are genuinely traveling objects (never at rest). Over their lifetimes (i.e. before they annihilate with each other), these dislocations constantly move under the tension of the facet edges terminating at the dislocation core [26] — cf. § 4.1.

We have elucidated the structure and dynamics of these far-from-equilibrium topological defects [28]. The derived fundamental dislocation dynamics laws that relate the dislocation velocity to the Rippled state period (i.e. the wavelength λ) provide the analytical deduction of experimentally interesting surface coarsening laws that govern its temporal evolution, the ripple amplitude ($\sim$ surface roughness) w and the ripple coherence length ξ. For the simple Rippled states, we thus obtain the coarsening laws $\lambda \sim w \sim t^{2/7}$ and $\xi \sim t^{4/7}$ in excellent agreement with the simulations [25, 26]. However, in some circumstances we find that these states may exhibit a faster coarsening (i.e. roughening) with $\lambda \sim w \sim t^{1/3}$ and $\xi \sim t^{1/2}$, as also observed in simulations [26]. In Ref. [28], we have also discussed the dislocations in the Rectangular Rippled interfacial states for which the coarsening laws $\lambda \sim w \sim t^{1/4}$ and $\xi \sim t^{1/2}$ previously inferred from the simulations [25, 26] are found. The surface coarsening laws at the transition from the Rippled to the Rhomboidal Pyramid state are discussed, and also the crossover effects that occur in the proximity of this transition on (110) crystal surfaces. Our analytic theory of dislocation dynamics is based on the general phenomenological approach to surface dynamics in multilayer epitaxial growth outlined in § 2. Let us now review our results on dislocation dynamics, and implications for interface coarsening.

The structure of a single dislocation close to its core is shown in Fig. 23, for the R_2 rippled state with half period λ. The dislocations of a rippled state travel along the ripples — i.e. their drift velocities are parallel to the direction of the edges as shown in Fig. 12. A surface section around a dislocation is shown in Fig. 23(a); and Fig. 23(b) depicts the dislocation in terms of the edges between facet-like surface sections seen in Fig. 23(a). The dislocation in Fig. 23(b) moves to the right, as observed in simulations [3, 16], and this motion is essential for the overall surface dynamics as the primary mechanism of the rippled state surface coarsening. Thus as the dislocation in Fig. 23 moves to the right, the two facets of width λ (above and below the middle facet) merge to form the larger facet of width 2λ. These two facets, labeled in Fig. 23 as the "upper" (U) and "lower" (L) facets relative to the "middle" (M) facet in Fig. 23, play an essential role in the dislocation dynamics — in particular, in deriving the kinetic law for $v_{\rm d}(\lambda)$ relating the dislocation velocity $v_{\rm d}$ to the phase half-period λ, essential for

https://doi.org/10.4208/eajam.040411.030611a Published online by Cambridge University Press

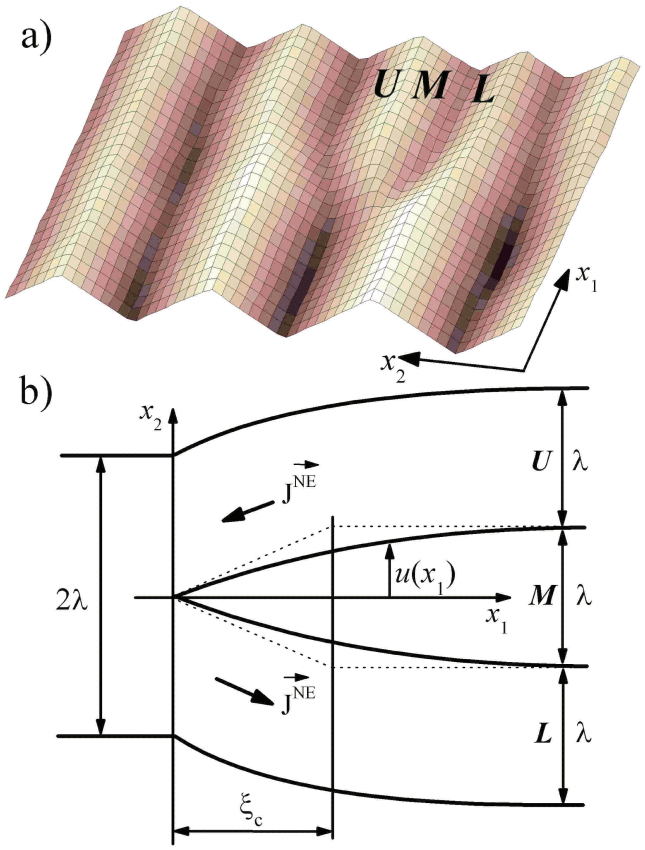

Figure 23: (a) 3D view of a surface section containing a dislocation in the simple Rippled state R_2, from simulations [26]. (b) The dislocation depicted in terms of the edges between facet-like surface sections in Fig. (a). The dislocation consists of three R_2 facets — viz. a flat middle facet (M) having a knife-like shape, and upper (U) and lower (L) facets that are both slightly curved (mostly along the x_1-direction).

obtaining the surface coarsening laws. As discussed below, the dislocation core eventually becomes sharp, with λ (core length scale along x_2) much smaller than the core lateral size ξ_c (core length scale along x_1) as seen in Fig. 23(b). In this figure, $\mathbf{J}^{\rm NE} = 0$ on the middle (M) flat facet, whereas the upper and lower facets both move due to a nonzero downhill current, which displaces the material from the upper facet where $\mathbf{J}^{\rm NE}$ flows to the left to the lower facet where $\mathbf{J}^{\rm NE}$ flows to the right. This removal of material from the upper facet and its subsequent absorption on the lower facet is the mechanism that causes the dislocation in Fig. 23(b) to move to the right.

Our analytic theory of the dislocation dynamics [28] is based on these ideas. One of the central results of this theory is the scaling law

$$v_{\rm d} \sim \frac{\xi_c}{\lambda^3} \,, \tag{4.17}$$

which relates the dislocation velocity $v_{\rm d}$ to the phase half-period λ and the dislocation

https://doi.org/10.4208/eajam.040411.030611a Published online by Cambridge University Press

core lateral size ξ_c — cf. Fig. 23(b). To establish the dislocation dynamics law expressing $v_{\rm d}$ as a function λ, one also needs to relate ξ_c in (4.17) to λ. For example, for the dislocations of the R_2 rippled state [28] we have

$$\xi_c \sim \lambda^{3/2} \ , \tag{4.18a}$$

such that

$$v_{\rm d}(\lambda) \sim \frac{(a_- - a)^{1/2}}{\lambda^{3/2}} \sim \frac{1}{\lambda^{3/2}} \tag{4.18b}$$

for $\lambda \gg \lambda_{\rm cross}$. Here

$$\lambda_{\rm cross} \sim \frac{1}{(a_- - a)^2} \tag{4.19}$$

is the characteristic length scale, which depends on the distance $a_- - a$ away from the R_2-to-RhP state transition at the line $a_- = a$ in the phase diagram — cf. Figs. 8 and 9. At the transition, $\lambda_{\rm cross}$ in Eq (4.19) diverges, so another scaling regime becomes prominent at or near the transition. This regime is characterized by

$$\xi_c \sim \lambda^{5/4} \ , \tag{4.20a}$$

hence from (4.17) we have

$$v_{\rm d}(\lambda) \sim \frac{1}{\lambda^{7/4}} \tag{4.20b}$$

for $\lambda \ll \lambda_{\rm cross}$. For $\lambda > \lambda_{\rm cross}$, the ultimate scaling behavior seen near the transition critical point is given by Eq. (4.18). As this transition point is approached $\lambda_{\rm cross}$ diverges, leaving the purely critical scaling behavior in Eq. (4.20). Below we discuss the effects of this significant crossover on the overall surface coarsening dynamics of the rippled state.

From the simulations [25,26] (cf. § 4.1 here), the coarsening growth of the rippled state period λ is mediated by traveling dislocations with velocity $v_{\rm d}(\lambda)$, This is similar to that discussed in Ref. [18] denoted by MG, for pyramidal states on (001) surfaces — cf. § 3.2. Indeed, the (001) surfaces coarsen from the gliding motion and annihilation of two nearly independent dislocations ensembles, moving along the two mutually perpendicular principal axes of the (001) — cf. § 3.2 and Fig. 5. Thus the dislocations of one ensemble move in the direction of one principal axis, while the dislocations of the other ensemble move in the direction of the other principal axis. In the MG study of (001) surfaces, the dislocations from different ensembles occasionally collide and form bound pairs. However, these dislocation-bound states are short-lived and eventually decay — cf. Fig. 5. The two dislocation ensembles are nearly decoupled from each other, and they independently and simultaneously contribute to the (001) surface coarsening. Geometrically, *each* of the two dislocation ensembles on (001) surfaces shown is equivalent to the Rippled state dislocation ensemble on (110) surfaces in Fig. 12. Consequently, two basic relations of geometric origin for the growth kinetics of

https://doi.org/10.4208/eajam.040411.030611a Published online by Cambridge University Press

the surface state period λ can be adopted from the MG here — cf. also § 3.2 and Fig. 6. These are (i) the relation in Eq. (3.13)

$$\frac{1}{\lambda}\frac{d\lambda}{dt} = \frac{2v_{\rm d}(\lambda)}{\xi(\lambda)} \ , \tag{4.21}$$

with ξ the separation between dislocations along a ripple (cf. [18, 26], § 3.2, § 4.1 and also Fig. 12); and (ii) the relation

$$\xi \sim \lambda^{q-1} \ , \tag{4.22}$$

with q the number of channels for dislocation annihilations — i.e. the number of distinct ways for an annihilation to proceed by continuously changing the edge network (cf. [18], and Eq. (3.20) and Fig. 6 here). As discussed in Ref. [18], the dislocations of four-sided pyramidal states on (001) surfaces have $q = 3$ channels for their annihilations — cf. § 3.2 and Fig. 6. Similarly, any dislocation D on (110) surfaces in Fig. 12 may annihilate (with an anti-dislocation) the core that is on the same facet as the core of D — cf. the dislocation pairs terminating closed loops of facet edges in Fig. 12, in the annihilation channel 1. In addition, a dislocation may also annihilate with anti-dislocations that have cores on any one of the two nearest neighboring facets — e.g. the dislocation pair close to the right in Fig. 12(b), in the annihilation channels 2 and 3 similar to those in Fig. 6. Thus as before there are $q = 3$ channels for dislocation annihilations, allowed by the continuously changing edge networks of the rippled states on (110) surfaces.

There is a major qualitative difference between the MG dislocations of the four-sided pyramidal states on (001) surfaces and those of the rippled states discussed above — viz. the relevant velocity law $v_{\rm d}(\lambda)$. This difference affects the detailed form of the coarsening law giving the growth of $\lambda(t)$ with time t, which from Eqs. (4.21) and (4.22) can be extracted from

$$t = \int_0^{\lambda(t)} \frac{d\lambda}{\lambda}\frac{\xi(\lambda)}{v_{\rm d}(\lambda)} \sim \int_0^{\lambda(t)} \frac{d\lambda}{\lambda}\frac{\lambda^{q-1}}{v_{\rm d}(\lambda)} \ . \tag{4.23}$$

Thus the combination of Eq. (4.23) with the respective dislocation velocity law for $v_{\rm d}(\lambda)$ produces the related coarsening law governing the dynamics of the rippled states on (110) surfaces. For the power velocity law of the form

$$v_{\rm d}(\lambda) \sim \frac{1}{\lambda^{n_v}} \ , \tag{4.24}$$

Eq. (4.23) implies the coarsening law

$$\lambda(t) \sim t^{n_\lambda} \qquad \text{and} \qquad \xi(t) \sim t^{n_\xi} \ , \tag{4.25}$$

with

$$n_\lambda = \frac{1}{q - 1 + n_v} \tag{4.26}$$

https://doi.org/10.4208/eajam.040411.030611a Published online by Cambridge University Press

and

$$n_\xi = (q-1)n_\lambda = \frac{q-1}{q-1+n_v} \,. \tag{4.27}$$

However, in the presence of the crossover behavior described in Eqs. (4.18)–(4.20), $v_{\rm d}(\lambda)$ is not a simple power law as in Eq. (4.24). Nevertheless, since $v_{\rm d}(\lambda)$ has power law asymptotic forms on both sides of the crossover, the crossover behavior of $v_{\rm d}(\lambda)$ versus λ directly implies the corresponding crossover behavior of $\lambda(t)$ (and of $\xi(t) \sim [\lambda(t)]^{q-1}$) versus time t. This crossover occurs at a characteristic time scale $t_{\rm cross}$, at which $\lambda(t_{\rm cross}) = \lambda_{\rm cross}$ with $\lambda_{\rm cross}$ as in Eq. (4.19). There are thus two scaling behaviors, one for $t \ll t_{\rm cross}$ corresponding to $\lambda(t) \ll \lambda_{\rm cross}$ and the other for $t \gg t_{\rm cross}$ when $\lambda(t) \gg \lambda_{\rm cross}$. The crossover time scale $t_{\rm cross}$ can be obtained by combining Eq. (4.23) with Eqs. (4.19) and (4.20b), yielding the time scale

$$t_{\rm cross} \sim \frac{1}{(a_- - a)^{2q+3/2}} = \frac{1}{(a_- - a)^{15/2}} \tag{4.28}$$

that diverges at the ripple-to-RhP state transition point because $a_- - a$ vanishes at this transition. For $t \ll t_{\rm cross}$, one has $\lambda \ll \lambda_{\rm cross}$ and $v_{\rm d}(\lambda)$ as in Eq. (4.20b), corresponding to Eq. (4.24) with the velocity exponent $n_v = 7/4$. With this value of n_v, from Eqs. (4.26) and (4.27) with $q = 3$ we find that $w(t) \sim \lambda(t) \sim t^{n_\lambda}$ and $\xi \sim t^{n_\xi}$, where

$$n_\lambda = \frac{4}{15} \cong 0.2666 \qquad \text{and} \qquad n_\xi = \frac{8}{15} \,. \tag{4.29}$$

At the ripple-to-RhP transition ($a_- - a = 0$), the crossover time given by Eq. (4.28) is infinite, and coarsening with the exponents in Eq. (4.29) persists for arbitrarily long times. Near the transition ($a_- - a > 0$) in the rippled phase, $t_{\rm cross}$ is finite; and for $t \gg t_{\rm cross}$ one has $\lambda(t) \gg \lambda_{\rm cross}$ with $v_{\rm d}(\lambda)$ as in Eq. (4.18b), corresponding to Eq. (4.24) with the velocity exponent $n_v = 3/2$. With this value of n_v, from Eqs. (4.26) and (4.27) with $q = 3$ we find $w \sim \lambda \sim t^{n_\lambda}$ and $\xi \sim t^{n_\xi}$, where

$$n_\lambda = \frac{2}{7} \cong 0.2857 \qquad \text{and} \qquad n_\xi = \frac{4}{7} \,. \tag{4.30}$$

Indeed, from Eqs. (4.18b) and (4.23), for $t \gg t_{\rm cross}$ we find

$$w(t) \sim \lambda(t) \sim (a_- - a)^{1/7}\, t^{2/7} \,, \tag{4.31}$$

indicating that the amplitude of this coarsening law vanishes at the R_2-to-RhP transition. At the transition point, the coarsening given by Eq. (4.31) is pushed away to infinite time, and replaced by the slower coarsening law $w(t) \sim \lambda(t) \sim t^{4/15}$ from Eq. (4.29). Away from the transition point, this critical coarsening behavior persists up to time $t_{\rm cross}$, when it crosses over to the coarsening law in Eq. (4.31) with the bigger coarsening exponent $n_\lambda = 2/7 \cong 0.2857$. This exponent is in an excellent agreement with the value obtained from the rippled state simulations [25, 26], away from the transition point. The simulations also indicate that the amplitude of the coarsening

https://doi.org/10.4208/eajam.040411.030611a Published online by Cambridge University Press

law decreases as the R_2-to-RhP transition is approached ($a_- - a \to 0$) as shown in Fig. 11(a), in accord with Eq. (4.31).

To summarize, the analytic results explain the coarsening of the Rippled state with

$$\lambda \sim t^{2/7} \qquad \text{and} \qquad \xi \sim t^{4/7} \tag{4.32}$$

seen in the simulations [25, 26], but in some circumstances there is a different coarsening where

$$\lambda \sim t^{1/3} \qquad \text{and} \qquad \xi \sim t^{1/2} \tag{4.33}$$

in the Rippled state simulations [26], as noted in § 4.1. In the phase diagram, such a coarsening occurs for $u_{21} \neq u_{12}$ in a sub-domain of the Rippled state range, just below the intensely rough sub-domain of the RhP state in Figs. 8 and 9 (close to the transition line to the $R^{(\mathrm{buc})}$ state). The morphology of the dislocations in this sub-domain from the simulations is shown in Fig. 12(b). For these knife dislocations there are typically long cores, with core size ξ_c comparable to the separation between dislocations given by

$$\xi \sim \xi_c \, . \tag{4.34}$$

Consequently, on invoking Eq. (4.18a) we find

$$\xi \sim \lambda^{3/2} \, . \tag{4.35}$$

In the regime exhibiting these maximally elongated dislocation cores (with $\xi_c \sim \xi$), Eq. (4.35) actually replaces Eq. (4.22). Note however that Eq. (4.35) has the form of Eq. (4.22), on formally setting $q = 5/2$. With this value of q and $n_v = 3/2$ [cf. Eq. (4.18a)], Eq. (4.26) and Eq. (4.27) yield

$$n_\lambda = \frac{1}{3}, \qquad \text{and} \qquad n_\xi = \frac{1}{2} \, . \tag{4.36}$$

These results explain the scaling behavior in Eq. (4.33), suggested by the simulations in the sub-domain of the Rippled state range.

Next, let us consider the coarsening behavior of Rectangular Rippled states seen in Fig. 13. For these states, simulations [25, 26] suggest that

$$\lambda \sim t^{1/4}, \qquad \text{and} \qquad \xi \sim t^{1/2} \, . \tag{4.37}$$

The scaling behavior in Eq. (4.37) can be also understood within the present analytic framework. Note that the dislocations of the Rectangular Rippled Stated are structurally different from the dislocations of ordinary rippled states, so the scaling behavior in Eq. (4.37) is different from that for simple rippled states in Eqs. (4.32) and (4.33). Indeed, consider a typical dislocation of the Rectangular Rippled state, as depicted in Fig. 24 for the case of the $R_2^{(\mathrm{rec})}$ state. The core of this dislocation is an R_1 facet with a

https://doi.org/10.4208/eajam.040411.030611a Published online by Cambridge University Press

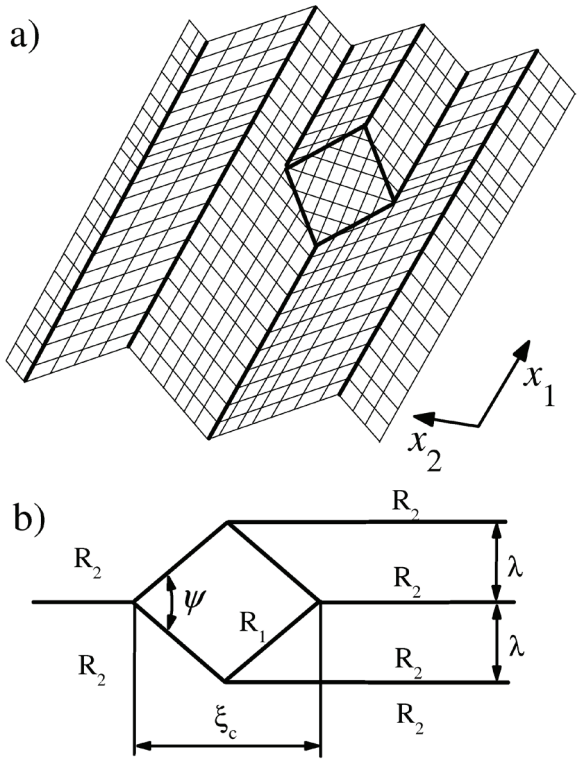

Figure 24: (a) 3D view of a surface section around a dislocation in a Rectangular Rippled state $R_2^{(\mathrm{rec})}$. (b) The dislocation depicted in terms of the edges between facet-like surface sections seen in Fig. (a), incorporating a smaller rhomboidally shaped R_1 facet at its core in addition to the long R_2 facets. (This figure is reproduced from Ref. [28].)

rhombic shape — cf. Fig. 24(b). The rhomboidal angle ψ in Fig. 24 is fixed by model parameters — i.e. it does not depend on the dislocation size. Due to this geometric constraint, the lateral core size

$$\xi_c \sim \lambda \, . \tag{4.38}$$

From Eqs. (4.38) and (4.17), the velocity law for the dislocations in the Rectangular Rippled states has the form

$$v_{\mathrm{d}} \sim \frac{1}{\lambda^2} \, , \tag{4.39}$$

which corresponds to Eq. (4.24) with velocity exponent $n_v = 2$. Thus from Eqs. (4.26) and (4.27), and again with $q = 3$ channels, we find

$$n_\lambda = \frac{1}{4}, \qquad n_\xi = \frac{1}{2} \, . \tag{4.40}$$

These results analytically explain the scaling behavior of the Rectangular Rippled states in Eq. (4.37), inferred earlier from the simulations [25, 26].

https://doi.org/10.4208/eajam.040411.030611a Published online by Cambridge University Press

It is significant to note that coarsening of the four-sided pyramid states on (001) surfaces (cf. § 3.2 here and Eq. (3.25) in particular), and also the RhP state on (110) surfaces, is *also* governed by the scaling law (4.37). This corresponds to Eq. (4.38) being satisfied for the dislocations in these states — i.e. the lateral dislocation core size ξ_c is proportional to λ.

Consequently, from (4.17) the velocity law takes the same form $v_{\rm d} \sim 1/\lambda^2$ as in Eq. (4.39), so the coarsening exponents in Eq. (4.40) also apply to the four-sided pyramid states on (001) surfaces [cf. Eq. (3.21) in § 3.2] and to the RhP state on (110) surfaces. However, higher values of the coarsening exponents ("enhanced coarsening") are seen in the simulations [26], in the RhP range close to the $R^{(\rm buc)}$ state [cf. § 3.1 and Fig. 11]. Indeed, this intensely rough RhP domain is adjacent to the intensely rough rippled state, with the coarsening as in Eq. (4.33).

We end this section with a few further remarks. The discussion presented here has addressed the rippled and other states on (110) surfaces, in the slope selection dominated regime reached at long times. In this regime, the spatial period $\lambda \sim t^{n_\lambda}$ and the interface roughness (width) $w \sim t^\beta$ must scale with the same coarsening exponent $n_\lambda = \beta$ as slope $\sim w/\lambda =$ const., due to the slope selection. In contrast to this long time regime where $n_\lambda = \beta$, in ion erosion studies on Cu (110) [33, 35] it appears that the selected facets of the Rippled state have not yet fully reached the preferred slope magnitude — their slope $\sim w/\lambda$ still grows within the experimentally accessible time scale. Such early time regimes are theoretically known to exhibit the coarsening exponent n smaller than β with typically small values [22], as was indeed observed in these experiments on Cu (110) crystal surfaces. We also note that the above analytic discussions of the rippled state ignore the vertical asymmetry (VA) discussed in § 4.2, which produces a contribution to the surface curvature current that is even under vertical reflection $h \to -h$. The VA effects were examined in detail in recent simulations [27] reviewed in § 4.2, which show that the VA does not alter the coarsening laws of simple Rippled, Rhomboidal Pyramid and Rectangular Rippled states. Thus the VA is irrelevant for these states — i.e. at long times, the coarsening of these states obeys the zero VA coarsening laws discussed. Nonetheless, in Ref. [27] the VA was shown to be capable to induce novel surface states which are altered versions of the Rectangular Rippled states — cf. § 4.2. One of them, the so-called Altered $R_1^{(\rm rec)}$ state, was found from simulations [27]) to exhibit an enhanced coarsening with $\lambda \sim w \sim t^{0.4}$. This is significantly different from that for ordinary Rectangular Rippled states in Eq. (4.40), but unsurprising given the significant structural differences between the $R_1^{(\rm rec)}$ and the Altered $R_1^{(\rm rec)}$ states [27]. Detailed analytic understanding of the structure and coarsening laws of the VA induced Altered $R_1^{(\rm rec)}$ state remains an issue for future theoretical work. Another experimentally significant theoretical challenge is to analytically deduce the enhanced coarsening where $\lambda \sim w \sim t^{0.4}$, seen in the simulations of the Buckled Rippled and intensely rough RhP state even for zero VA — cf. § 4.1.

https://doi.org/10.4208/eajam.040411.030611a Published online by Cambridge University Press

5. Far-From-Equilibrium Transitions in the Epitaxial Growth and Erosion on (001) Surfaces

On square symmetry surfaces (001) surfaces, the ESV instability [4] frequently induces the formation of nearly periodic (defected) checkerboard arrangements of alternating four-sided pyramids and pits (inverted pyramids), with sizes growing in time as $t^{1/4}$ as exemplified by Cu(001) epitaxial growth [44]. As discussed in § 3.2, this coarsening law may be understood from the dynamics of topological defects (dislocations) of the regular checkerboard structure [18,19]. However, other structures have recently been suggested by experiments on (001) surfaces [36–40]. Further, a far-from equilibrium phase transition between two kinds of four-sided pyramidal states has recently been observed in the epitaxial growth on Ag(001) by de Mongeot et al. [36]. This transition occurs as a 45° rotation of pyramid facets at a low critical temperature (≈ 100 degrees K), and may be attributed to deactivation of corner crossing processes [46]. At significantly higher critical temperature, a similar transition has been seen in erosion on Cu(001), but this has been disputed [37]. Until our study [29], a deep qualitative understanding of these interesting experimental results was missing and some long-standing basic questions remained unresolved, even for the epitaxial growth and erosion on common (001) surfaces. Thus how does vertical (pyramid-pit) asymmetry affect interface structure and its coarsening dynamics? And what are the possible interfacial morphologies and structures involved in the 45° facet rotation transitions on (001) surfaces?

5.1. The multitude of interface states on (001) surfaces

The above recent and long-standing questions have been addressed [29]. The epitaxial growth and erosion on (001) crystal surfaces were elucidated by considering the general phenomenological approach outlined in § 2, expressing the dynamics of the interface profile $h(x_1, x_2, t)$ through the conservation law Eq. (2.1) of the surface current $\mathbf{J} = (J_1, J_2)$ — i.e.

$$\frac{\partial h}{\partial t} = -\boldsymbol{\nabla}\cdot\mathbf{J} \quad \text{where} \quad \mathbf{J} = \mathbf{J}^{(NE)}(\mathbf{M}) + \mathbf{J}^{(\mathrm{curv})} \ , \tag{5.1}$$

on again omitting the white noise term $\eta(\mathbf{x}, t)$. As in § 2, the surface non-equilibrium current $\mathbf{J}^{(NE)}$ is a function of the local interface slope vector $\mathbf{M} = (M_1, M_2) = \boldsymbol{\nabla} h$, whereas the $\mathbf{J}^{(\mathrm{curv})}$ includes the "curvature currents" that vanish on flat interfaces (facets) — viz. the surface diffusion-like current $\sim \nabla(\nabla)^2 h$ and the vertical asymmetry Villain current $\sim \nabla(\nabla h)^2$ breakiing the vertical reflection symmetry $h \to -h$. The square symmetry of the (001) surface imposes some ubiquitous properties on $\mathbf{J}^{(NE)}(\mathbf{M}) = (J_1^{(NE)}(\mathbf{M}), J_2^{(NE)}(\mathbf{M}))$, which again must transform in the same way as the slope vector $\mathbf{M}$ under symmetry transformations of the (001) surface. Thus

https://doi.org/10.4208/eajam.040411.030611a Published online by Cambridge University Press

under the basic square reflections we have

$$(M_1, M_2) \to (-M_1, M_2),$$
$$(J_1^{(NE)}, J_2^{(NE)}) \to (-J_1^{(NE)}, J_2^{(NE)})$$

and

$$(M_1, M_2) \to (M_1, -M_2)\ ,$$
$$(J_1^{(NE)}, J_2^{(NE)}) \to (J_1^{(NE)}, -J_2^{(NE)})\ .$$

In addition, the square diagonal reflection symmetry $(M_1, M_2) \to (M_2, M_1)$ implies $(J_1^{(NE)}, J_2^{(NE)}) \to (J_2^{(NE)}, J_1^{(NE)})$, which is the condition $J_1^{\rm NE}(M_1, M_2) = J_2^{\rm NE}(M_2, M_1)$ met in § 2. As before, these symmetry restrictions on the form of $\mathbf{J}^{(NE)}$ can be used to classify the solutions where $\mathbf{J}^{(NE)}(\mathbf{M}) = 0$ — i.e. the zeros related to the preferred slopes $\mathbf{M}$ of the facets that develop across the growing interface and self-organize into pyramidal structures. From the square symmetry of (001), there are three possible kinds of preferred slope vectors $\mathbf{M} = (|\mathbf{M}|\cos(\theta), |\mathbf{M}|\sin(\theta))$ as follows.
(i) Singlet at $|\mathbf{M}| = 0$.
(ii) Quartet of equivalent (symmetry related) slope vectors. There are two *nonequivalent* types of quartets: a type I quartet, along square diagonals $\theta = 45^\circ + 90^\circ(n-1)$, $n = 1, 2, 3, 4$; and a type II quartet, along square sides $\theta = 90^\circ(n-1)$, $n = 1, 2, 3, 4$, already encountered in § 2. Importantly for an understanding of the 45° rotation transition on (001) surfaces, the type I and type II quartets are *not* equivalent because the 45° rotation is not a symmetry of the (001) surface.
(iii) Octet of equivalent slope vectors pointing along eight polar angles $\theta = 90^\circ(n-1) \pm \phi$, where ϕ is an angle in the range $-45^\circ < \phi < +45^\circ$ and $n = 1, 2, 3, 4$. Although naturally permitted by the square symmetry of the (001) surface, the possible existence of an octet zero and its physical relevance had not been anticipated prior to our study [29].

Due to the ESV instability, the singlet at $\mathbf{M} = 0$ is unstable, and preferred facets may therefore correspond to quartets or to an octet. Thus the stable type I quartet may give rise to the checkerboard Phase I (PI) of four-sided pyramid structure in Fig. 25. Likewise, the stable type II quartet may give rise to the checkerboard Phase II (PII) of four-sided pyramid structure in Fig. 25. The states PI and PII *both* enter Fig. 25, which depicts the unified far-from-equilibrium phase diagram for the epitaxial growth and erosion phenomena on (001) surfaces [29]. Type I and type II pyramid facets are geometrically related by the 45° rotation, and the phase diagram incorporates the experimentally observed 45° facet rotation transition on Ag(001) [36]. Moreover, we find that the octet zeros give rise to a novel interface state, shown in Fig. 25(a) from simulations. This state intervenes between PI and PII states and is characterized by the interface slope distribution (SD) function in Fig. 25(a), with eight peaks forming an octagon in the $\mathbf{M}$-plane at the eight polar vectors $\theta = 90^\circ(n-1) \pm \phi$ ($n = 1, 2, 3, 4$), so we call it the *octagonal pyramid* ($OctP$) state. From simulations, we find this state

https://doi.org/10.4208/eajam.040411.030611a Published online by Cambridge University Press

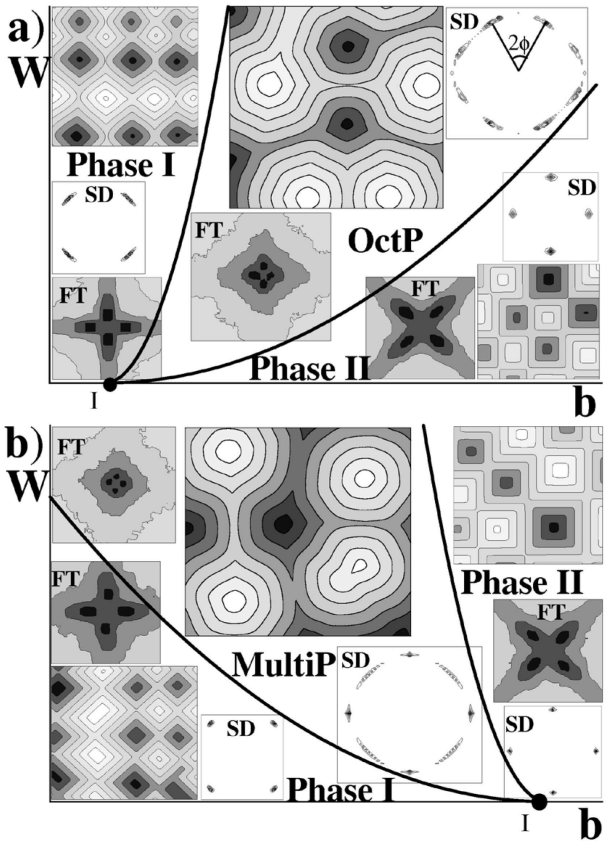

Figure 25: Kinetic phase diagram of the interface model with $\mathbf{J}^{(NE)}(\mathbf{M})$ in Eq. (5.2), depicting the $(b, W = wu^2/r)$ plane for fixed c and d. The point I is at $b = 1$, $W = 0$. (a) The case $(d-1)(c-d-1) < 0$, with $OctP$ state realized. (b) The case $(d-1)(c-d-1) > 0$ with $MultiP$ state realized, showung interface height contour plots, height FTs (yielding in-phase diffraction patterns) and SD functions (yielding out-of-phase diffraction patterns) from simulations [29]. The $OctP$ angle ϕ in (a) changes from 0 at the transition to $P\,II$ to 45° at the transition to $P\,I$ (VA$= 0$).

corresponds to a structure with pyramids having up to eight facets — cf. Fig. 26(a). The interface slope distribution (SD) of the $OctP$, with eight peaks positioned as in Fig. 25(a), is the same as the SD of the intermediate state seen in the 45° rotation transition on Cu(001) — cf. the eight lobe out-of-phase diffraction patterns observed by Broekmann *et al*. [37]. It has been suggested that the 45° rotation transition on Cu(001) (erosion) may be due to post-deposition annealing [37]. However, in the study of Ag(001) growth by de Mongeot *et al*. [36] such post-growth annealing effects were carefully eliminated at low temperatures (< 100 degrees K) where the 45° facet rotation transition was found, so it can be considered a far-from-equilibrium growth transition.

The epitaxial growth and erosion phenomenology on common (001) surfaces can

https://doi.org/10.4208/eajam.040411.030611a Published online by Cambridge University Press

be explained by considering the interface equation of motion Eq. (5.1) with a generic form of the non-equilibrium current $\mathbf{J}^{(NE)}(\mathbf{M})$ permitted by the symmetries of the (001) surface. As discussed in § 2, $\mathbf{J}^{(NE)}(\mathbf{M})$ can be expressed as an expansion in powers of $\mathbf{M}$ respecting the symmetry restrictions such that

$$J_1^{(NE)} = M_1 \left[r - u(M_1^2 + bM_2^2) - w(M_1^4 + cM_1^2M_2^2 + dM_2^4) + \cdots \right] ,$$
$$J_2^{(NE)} = M_2 \left[r - u(M_2^2 + bM_1^2) - w(M_2^4 + cM_2^2M_1^2 + dM_1^4) + \cdots \right] . \qquad (5.2)$$

Equation (5.2) is the natural generalization of Eq. (2.7), obtained by incorporating the (symmetry permitted) fifth order terms — i.e. the w-terms in Eq. (5.2) introduced in Ref. [29]. These w-terms are essential for a qualitative understanding of the 45° rotation transition on realistic (001) surfaces. Indeed, for $w = 0$ we recover the (001) surfaces model Eq. (2.7), where the 45° rotation transition between the Phase I and Phase II occurs at the *single* point I at $(b = 1, W = 0)$ in Fig. 25, with the phase diagram in terms of the two parameters $(b, W = wu^2/r)$ — and we recall that for a system at the $(b = 1, W = 0)$ point, $\mathbf{J}^{(NE)}(\mathbf{M})$ vanishes on the circle $|M|^2 = r/u$ in the M-space, which is unphysical and *in general* excluded on real (001) surfaces. The w-terms in Eq. (5.2) are essential to break this artificial symmetry — i.e. they *must* be included to realistically discuss the 45° rotation transition, and produce the novel ubiquitous intermediate states $OctP$ and $MultiP$ as discussed below (cf. also the kinetic phase diagram in Fig. 25 for $w \neq 0$). Thus for typical situations with small selected $|\mathbf{M}|$, the minimal basic growth model for (001) is actually obtained by truncating out the higher order terms indicated by the dots in Eq. (5.2). In this limit, we model the curvature current $\mathbf{J}^{(\mathrm{curv})}$ in Eq. (5.1) as described in § 2 — cf. Eq. (2.5) and Eq. (2.4) incorporating the effects of the vertical asymmetry (VA). The kinetic phase diagram in Fig. 25 is analytically deduced by stability analysis of the facets corresponding to the zeros of $\mathbf{J}^{(NE)}(\mathbf{M})$ in Eq. (5.2) and further corroborated by relevant numerical simulations, to yield the 45° rotation transition between PI and PII states shown in Fig. 25. There we also see the intermediate $OctP$ state, which occurs in a region in Fig. 25(a) where neither type I nor type II facets are stable. Although many-sided, the $OctP$ state pyramids have the same coordination (spatial arrangement) and thus qualitatively yield the same Fourier transforms (i.e. nearly in-phase-diffraction pattern) as the four-sided pyramids of a nearby checkerboard state — cf. Fig. 25(a). Within the model Eq. (5.2), the 45° rotation transition involving the $OctP$ intermediate state occurs if $(d-1)(c-d-1) < 0$.

On the other hand, for

$$(d-1)(c-d-1) > 0 \qquad (5.3)$$

Eq. (5.2) yields a qualitatively different intermediate state that we call $MultiP$ as shown in Fig. 25(b), when the 45° rotation transition goes through a multi-stable region where type I and type II quartet facets are both stable. In this region, SD (i.e. the out-of-phase-diffraction pattern) also has eight peaks — cf. Fig. 25(b). However, in contrast to the SD of $OctP$ in Fig. 25(a), the eight SD peaks of the $MultiP$ in Fig. 25(b) are not equivalent — note that the SD of $MultiP$ structures is a superposition of the

https://doi.org/10.4208/eajam.040411.030611a Published online by Cambridge University Press

SD peak patterns from the nearby PI and PII states, with strong sharp peaks along type II facet directions and broad weaker peaks along type I facet directions. This corresponds to multi-sided pyramids (with *up to* eight sides) with prominent type II facets (like in the PII state) — cf. Figs. 25(b), 26(b), and 26(e). However, this state has the same spatial pyramidal arrangement as the PI state — cf. the interface plots and their FTs in Figs. 25(b) and 26(b,e,f). Thus the $MultiP$ is a *hybrid* state, neither a PI nor a PII state. For VA $= 0$, the $MultiP$ state has the pyramid spatial arrangement of PI *already* at early times. but for VA $\neq 0$ its pyramids initially form with the spatial arrangement of PII — cf. Fig. 26(e, left panel). Eventually however, the pyramid lattice rearranges, and the spatial arrangement becomes the same as that of the PI state — cf. Fig. 26(e, right panel). This striking spatial rearrangement of the $MultiP$ state is also documented by the time sequence of FTs in Fig. 26(f). Close to the center of the $MultiP$ domain in Fig. 25(b), the VA-dominated early time morphologies persist over time scales longer than the simulation times in Ref. [29], suggesting that VA on (001) surfaces may produce the eventual (long time) interface morphologies not present for zero VA. All these interesting VA effects on the structure of an interface have been found in the regime where the $MultiP$ state is realized, and in simulations no such dramatic structural VA effects on the other $OctP$ state for (001) surfaces were found.

5.2. Enhanced roughening of (001) surfaces

The pyramid sizes in the $MultiP$ and $OctP$ states grow as $t^{1/3}$, *both with and without* VA — cf. Fig. 26(d). Both intermediate states coarsen via local pyramid (or pit) coalescence. These numerical results demonstrate the robustness of the $t^{1/3}$ law for growth via local pyramid coalescence. Indeed, for $W = 0$ and $b = 1$, pyramids form at the isotropic transition point I in Fig. 25 with randomly oriented facets, and grow as $t^{1/3}$ via local pyramid coalescence (cf. Ref. [18], and § 3.1 here). For realistic (001) surfaces $w \sim W \neq 0$, when the transition always goes through the intermediate states in Fig. 25, with pyramid facets oriented by (001) square anisotropy. However, as documented in Fig. 26(d), they still grow as $t^{1/3}$ via local coalescence as in the simulations [29].

Away from the intermediate states in Fig. 25, the sizes of four-sided pyramids in the checkerboard states PI and PII grow as $t^{1/4}$, *both with and without* VA — cf. Fig. 26(g). This growth is mediated by motion of the topological defects (dislocations) of the mesh of pyramid facet edges [18], as discussed in § 3.2 here — cf. Figs. 26(h) and (i). Note that VA introduces two kinds of pyramid facet edges, sharp and blunt. However, this VA-induced decoration of the edges mesh does not affect the topology of the mesh of facet edges, with dislocations present as documented in Figs. 26(h) and (i). In accord with the experiments [44], these results explain the striking insensitivity of the (zero VA) checkerboard $t^{1/4}$ growth law [18] to the presence of VA. We stress again that this $t^{1/4}$ coarsening behavior of the checkerboard occurs away from the 45° facet rotation transition — i.e. the transition to the intermediate state. However, *near* the intermediate states the coarsening mechanism of checkerboard pyramids changes into

https://doi.org/10.4208/eajam.040411.030611a Published online by Cambridge University Press

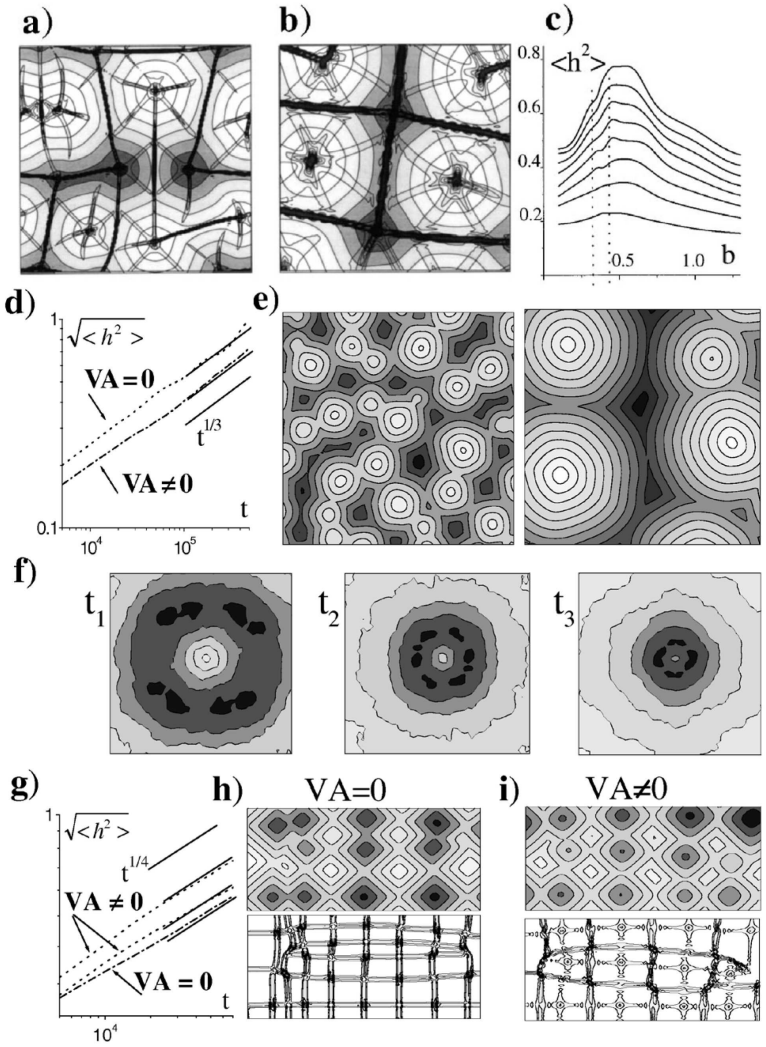

Figure 26: (a) $OctP$ state: a superposition of its interface height contour plots and facet edges plots (contour plots of the interface curvature magnitude). Note sharp (dark) edges at pyramid bases, and blunt (faint) edges emerging from pyramid tops. (b) $MultiP$ state pyramids, formed out of both type I and type II facets: Note that the spatial arrangement of $MultiP$ pyramids is as in phase I [see also Figs. 25(b) and the panel (e) here]. (c) Square of interface width, $< h^2 >$ versus b for a fixed W for several times, increasing from bottom to top: Note the enhanced roughening in the proximity of the intermediate state (here, $MultiP$) between the dashed lines. In panels (a) (b) and (c), VA$= 0$. In (d), (e), and (f): VA effects on the $MultiP$ intermediate state. (d) Interface width $< h^2 >^{1/2} \sim t^{1/3}$, both with and without VA. (e) Due to VA$\neq 0$, at early times (left panel) the pyramids form with the spatial arrangement of phase II. However, at later times (the right panel), the spatial pyramid arrangement turns into that of phase I. This spatial rearrangement is illustrated also by the time sequence of FTs in (f), at $t_1 < t_2 < t_3$. In (g), (h), and (i): VA effects on checkerboard structure (away from intermediate states regions). (g) Interface width for three different strengths of VA (increasing from zero, from bottom to top): $< h^2 >^{1/2} \sim t^{1/4}$ both with and without VA. Surface without [in (h)] and with VA [in (c)]. In (i), note blunt (faint) facet edges emerging from pyramid tops, and sharp (dark) edges emerging from the pits.

https://doi.org/10.4208/eajam.040411.030611a Published online by Cambridge University Press

coalescence, yielding *enhanced roughening* manifest through the $t^{1/3}$ growth at long times, and *also* faster growth at short times — cf. Fig. 26(c). From the simulations, we find that this $t^{1/3}$ coarsening occurs both with and without VA — cf. Fig. 26(d).

Given our theoretical results, let us now discuss various recent experiments on Ag(001) growth. Enhanced roughening has been seen by Stoldt *et al*. [38] near the temperature of 100 degrees K, precisely where de Mongeot *et al*. [36] report the 45° facet rotation transition. Thus within a unified framework, our theory has related previously disconnected experimental findings on Ag(001) growth. We predict that either the $MultiP$ or the $OctP$ state ubiquitously develops on Ag(001) and intervenes in the 45° rotation transition. Microscopically, this transition may be driven by Type I facet destabilization (with decreasing temperature say), due to Schwoebel barriers on kinks on the terrace steps of the Type I facets. These kinks are easily rounded by adatoms only at high enough temperature, so the Phase I is stable there. With decreasing temperature, the Type I facets may destabilize (or become less stable) due to the Schwoebel barriers, and the Phase I may transform into the $MultiP$ state that has the SD closer to that of the Phase II — cf. Fig. 25(b). This scenario for the facet rotation transition does indeed correspond to out-of-phase diffraction data — i.e. the slope distributions changes seen on Ag(100) by de Mongeot and co-workers [36]. In contrast to our model, the previous microscopic simulations of Ag(001) in Refs. [38–40] (by construction) do not allow for the 45° facet rotation transition suggested by the experiments in Ref. [36]. However, it is interesting to note that the $MultiP$ pyramids in Figs. 25(b) and 26(b, e right panel) closely resemble (even for zero VA) the side-by-side arranged pyramidal mounds observed in the microscopic simulations [40].

In summary, the model of Ref. [29] reviewed in this section exhibits a generic multitude of interfacial states and transitions in epitaxial growth and erosion on (001) crystal surfaces. The model shows that the 45° facet rotation phenomenon observed on realistic (001) surfaces involves the formation of intermediate states (either $MultiP$ or $OctP$), which exhibit an enhanced interface roughening. The results for out-of-phase (SD) and in-phase (FT) diffraction patterns in Fig. 25 can be used to reveal the intermediate states in future experiments and numerical studies. Finally, the results of [29] reviewed here first elucidate the actual effects of the elusive vertical growth asymmetry on various interfacial states on (001) crystal surfaces. On the theoretical side, we note that from Eq. (5.2)

$$\frac{\partial J_1^{\rm NE}}{\partial M_2} - \frac{\partial J_2^{\rm NE}}{\partial M_1} = 2(c-2d)[M_1^3 M_2 - M_2 M_1^3] \; , \tag{5.4}$$

hence from the discussion in § 2 [cf. Eq. (2.16)], the model (5.2) can be generated from an effective free energy only if $c = 2d$. With this parameter choice, the inequality in Eq. (5.3) is easily seen to be satisfied, so within an effective free energy model the $MultiP$ state would be realized and the $OctP$ state actually forbidden. However, there is no reason (e.g. symmetry) to impose the condition that $c = 2d$, so in principle both

https://doi.org/10.4208/eajam.040411.030611a Published online by Cambridge University Press

$MultiP$ and $OctP$ states can be realized on the (001) surfaces of *different* materials.

6. Summary

Multilayer epitaxial growth and erosion by molecular beams exhibit the formation of large scale surface structures, such as the pyramidal and rippled interfacial states addressed in this review. Despite extensive experimental work, a deep understanding of the laws governing the growth of these structures (interface coarsening) was missing before the theoretical developments in the studies reviewed in this article [18, 25–29]. This theory provides analytic explanations of the experimentally observed coarsening laws, as detailed in § 3 and § 4.3. More importantly, it elucidates the detailed structure of interfacial morphologies seen in the epitaxial growth and erosion, as reviewed in § 4 and § 5. Our theoretical approach involves both numerical simulation and the analysis of continuum interface dynamics models for crystal surfaces of various symmetries. For the major (001), (110), and (111) crystal surfaces, a wealth of theoretically and experimentally significant results has been obtained from simple minimal models, based on mass conservation of the deposited thin film and on respecting the symmetries of the growing crystal surface. Conceptually, the theory establishes the relationship between interface coarsening in epitaxial growth (growth of the facets of pyramids and ripples) and more familiar phase ordering processes, such as the growth of ordered domains in magnetic systems (spinodal decomposition). However, our theory of epitaxial growth goes beyond the limits imposed in standard phase ordering theories that usually assume an effective free energy governs the system dynamics. Thus as detailed in § 2, § 4.2 and § 5, it incorporates the effects of the ubiquitous vertical growth asymmetry not tractable within an effective free energy approach. Also significant are the effects related to the form of the non-equilibrium current, where novel interfacial states emerge due to the absence of an effective free energy (even in the zero vertical asymmetry limit) — cf. § 4.1 and § 5.

Particularly important results from our approach relate to recent experimentally observed far-from-equilibrium phase transitions on (110) and (001) crystal surfaces. The theory in Refs. [25–28] reviewed in § 4 and § 5 provides non-equilibrium phase diagrams for these transitions, and also predicts and elucidates novel interfacial states involved in these transitions, with some but not all previously observed. For example, the Rhomboidal Pyramid State (§ 4.1) was theoretically predicted [25] and subsequently seen in the experiments on (110) surfaces [33, 35]. As noted by experimentalists [35], observations also indicate the possible presence of the Buckled Rippled interface state (§ 4.1), which is unusual in that it caries persistent (nonzero) surface currents that form vortex patterns reminiscent of self-organized convective flow patterns in hydrodynamics. This state owes its existence to the absence of the effective free energy in the governing interface dynamics. On the conceptual side, the existence of the Buckled Rippled interface state demonstrates it is not generally true that the surface current must vanish on the selected interfacial structures, as was previously commonly believed (although

https://doi.org/10.4208/eajam.040411.030611a Published online by Cambridge University Press

the surface current does indeed vanish in many interfacial states). Our theory has also elucidated the structure of complex interfacial states, such as the Rectangular Rippled states on (110) surfaces (§ 4.1 and § 4.2). In these states, it predicts the development of long roof-like multifaceted objects (huts) that have since been seen on Ag(110) surface [31, 34]. A major theoretical and conceptual finding on these structures is that they are highly affected by the vertical growth asymmetry (§ 4.2). Indeed, the experimental phenomenology of Rectangular Rippled states [30] can be understood in detail only by invoking the effects of the vertical growth asymmetry. As discussed in § 4.2, our theoretical results [27] in combination with experiments [30] on (110) surfaces provide strong evidence that nonzero vertical growth asymmetry induces the formation of unique surface structures. Our approach also elucidates far-from-equilibrium phase transitions on (001) surfaces (§ 5). It reveals that the experimentally observed 45° facet rotation phenomenon on (001) surfaces involves novel intermediate states ($MultiP$ or $OctP$), which exhibit the observed enhanced interface roughening [36]. Finally, the results of [29] reviewed in § 5 first elucidated the actual effects of vertical growth asymmetry on various interfacial states on (001) crystal surfaces.

In summary, using *single* models (one for each crystal surface symmetry type) the continuum modeling discussed in this article provides a unified understanding of the known experimental phenomenology in the epitaxial growth and erosion of crystal surfaces. Our novel theoretical and conceptual framework elucidates the interfacial dynamics, and predicts structures and transitions between the structures that have been observed.

Acknowledgments

This research has been supported by grants from the Milan Laboratories and the NSF-WV-EPSCoR program, and DAAD Grant No. A/02/15054. L.G. thanks the Max Planck Institute for the Physics of Complex Systems (Dresden) for hospitality. We also thank F. B. de Mongeot for discussions.

References

[1] See for example, J.Y. Tsao, Materials fundamentals of molecular beam epitaxy (World-Scientific, Singapore, 1993).
[2] G. Ehrlich and F.G. Hudda, J. Chem. Phys. 44 (1966), 1039.
[3] R.L. Schwoebel and E.J. Shipsey, J Appl. Phys. 37 (1966), 3982; R.L. Schwoebel, J. Appl. Phys. 40 (1969), 614.
[4] J. Villain, J. Phys. I (France) 1 (1991), 19.
[5] H.-J. Ernst, F. Fabre, R. Folkerts and J. Lapujoulade, Phys. Rev. Lett. 72 (1994), 112.
[6] M..D. Johnson, C. Orme, A.W. Hunt, D. Graff, J. Sudijono, L.M. Sander and B.G. Orr, Phys. Rev. Lett. 72 (1994), 116.
[7] J.W. Evans, D.E. Sanders, P. A. Thiel and A.E. DePristo, Phys. Rev. B 41 (1990) 5410; J.W. Evans, Phys. Rev. B 43 (1993) , 3897.

[8] D.D. Vvedensky, A. Zangwill, C.N. Luse and M.R. Wilby, Phys. Rev. E 48 (1993), 852.
[9] M. Siegert, in: Scale Invariance, Interfaces, and Non-Equilibrium Dynamics, eds. A.J. McKane, M. Droz, J. Vannimenus and D. Wolf, NATO ASI Series B, Vol. 344 (Plenum, New York, 1995) pp. 165-202.
[10] M.C. Bartelt and J.W. Evans, Phys. Rev. Lett. 75 (1995), 4250.
[11] G.W. Smith, A.J. Pidduck, C.R. Whitehouse, J.L.Glasper and J. Spowart, J. Cryst. Growth 127 (1993), 996; C. Orme, M.D. Johnson, K.-T. Leung, B.G. Orr, P. Smilauer and D. Vvedensky, J. Cryst. Growth 150 (1995), 128.
[12] J.E. Van Nostrand, S.J. Chey, M.-A. Hasan, D.G. Cahill and J.E. Greene, Phys. Rev. Lett. 74 (1995), 1127.
[13] K. Thurmer, R. Koch, M. Weber and K.H. Rieder, Phys. Rev. Lett. 75 (1995), 1767.
[14] J.A. Stroscio, D.T. Pierce, M. Stiles, A. Zangwill and L.M. Sander, Phys. Rev. Lett. 75 (1995), 4246.
[15] F. Tsui, J. Wellman, C. Uher and R. Clarke, Phys. Rev. Lett. 76 (1996), 3164; T. Michely, M. Kalff, G. Comsa, M. Strobel, and K.-H. Heinig, Phys. Rev. Lett. 86 (2001), 2589.
[16] M. Siegert and M. Plischke, Phys. Rev. Lett. 73 (1994), 1517.
[17] J. Amar and F. Family, Phys. Rev. B 54 (1996), 14742.
[18] D. Moldovan and L. Golubovic, Phys. Rev. E 61, 6190 (2000).
[19] M. Siegert, Phys. Rev. Lett. 81 (1998), 5481.
[20] A. J. Bray, Adv. Phys. 34 (1994), 357.
[21] L. Golubovic and R.P.U. Karunasiri, Phys. Rev. Lett. 66 (1991), 3156.
[22] L. Golubovic, Phys. Rev. Lett. 78 (1997), 90.
[23] L. Golubovic, D. Moldovan and A. Peredera, Phys. Rev. Lett. 81 (1998), 3387 ; L. Golubovic, D. Moldovan and A. Peredera, Phys. Rev. E 61 (2000), 1703.
[24] D. Moldovan and L. Golubovic, Phys. Rev. Lett. 82 (1999) 2884 ; D. Moldovan and L. Golubovic, Phys. Rev. E 60 (1999), 4377.
[25] L. Golubovic, A. Levandovsky, and D. Moldovan, Phys. Rev. Lett. 89 (2002), 266104.
[26] A. Levandovsky, L. Golubovic, and D. Moldovan, Phys. Rev. E74 (2006), 061601.
[27] A. Levandovsky and L. Golubovic, Phys. Rev. E 76 (2007), 041605.
[28] L. Golubovic and A. Levandovsky, Phys. Rev. E 77 (2008), 051606.
[29] A. Levandovsky and L. Golubovic, Phys. Rev. B 69 R (2004), 241402.
[30] F. B. de Mongeot, G. Costantini, C. Boragno, and U. Valbusa, Phys. Rev. Lett. 84 (2000), 2446. This study was the first one to report the ripple rotation transition on a (110) crystal surface, for the case of the Ag(110) surface (epitaxial growth), and to reveal an intermediate state intervening in the transition.
[31] G. Costantini, S. Rusponi, F. B. de Mongeot, C. Boragno, and U. Valbusa, J. Phys.: Cond. Matter 13 (2001), 5875.
[32] M. Albrecht, H. Fritzsche and U. Gradmann, Surf. Sci. 294 (1993), 1.
[33] A. Molle, F. B. de Mongeot, A. Molinari, F. Xiaerding, C. Boragno, and U. Valbusa, Phys. Rev. Lett. 93 (2004), 256103. This study revealed the Rhomboidal Pyramid state to be present in the erosion on Cu(110) and Rh(100) surfaces.
[34] F. B. de Mongeot, W. Zhu, A. Molle, R. Buzio, C. Boragno, U. Valbusa, E. G. Wang, and Z. Zhang, Phys. Rev. Lett. 91 (2003), 016102.
[35] A. Molle, F. B. de Mongeot, A. Molinari, C. Boragno, and U. Valbusa, Phys. Rev. B 73 (2006), 155418.
[36] F. B. de Mongeot, G. Costantini, C. Boragno, and U. Valbusa, Europhys. Lett. 58 (2002), 537.
[37] P. Broekmann, A. Mewe, H. Wormeester, and B. Poelsema, Phys. Rev. Lett. 89(2002),

146102.
[38] C. R. Stoldt, K. J. Caspersen, M. C. Bartelt, C. J. Jenks, J. W. Evans, and P. A. Thiel, Phys. Rev. Lett. 85 (2000), 800.
[39] K. J. Caspersen, C. R. Stoldt, A. R. Layson, M. C. Bartelt, P. A. Thiel, and J. W. Evans, Phys. Rev. B 63 (2001), 085401.
[40] K. J. Caspersen, A. R. Layson, C. R. Stoldt, V. Fournee, P. A. Thiel, and J. W. Evans, Phys. Rev. B 65 (2002), 193407.
[41] For review, see J. Krug, Adv. in Phys. 46 (1997), 139, and Physica A 313 (2002), 47. See also, J.W. Evans, P.A. Thiel, and M.C. Bartelt, Surf. Sci. Reports 61 iss. 1-2 (2006), 1.
[42] See, e.g., H. Haken, Synegetics (Springer-Verlag, 1978).
[43] J. Toner and D. R. Nelson, Phys. Rev. B 23 (1981), 316.
[44] J.-K. Zuo and J. F. Wendelken, Phys. Rev. Lett 78, 2791 (1997).
[45] M. Li and J. W. Evans, Phys. Rev. Lett. 95 (2005), 256101; ibid. 96 (2006), 079902 E, and Phys. Rev. B 73 (2006), 125434.
[46] J. Amar, Phys. Rev. B 60 (1999), R 11 317.

https://doi.org/10.4208/eajam.040411.030611a Published online by Cambridge University Press